Nanoparticles from 3d-metals: Influence of different substrates at different temperatures

Inaugural-Dissertation

zur Erlangung des Doktorgrades
der Mathematisch-Naturwissenschaftlichen Fakultät
der Heinrich-Heine-Universität Düsseldorf

vorgelegt von

Hendrik Bettermann
aus Düsseldorf

Düsseldorf, Januar 2018

aus dem Institut für Angewandte Physik
der Heinrich-Heine-Universität Düsseldorf

Gedruckt mit der Genehmigung der
Mathematisch-Naturwissenschaftlichen Fakultät der
Heinrich-Heine-Universität Düsseldorf

Referent: Prof. Dr. Mathias Getzlaff

Korreferent: Prof. Dr. Klaus Schierbaum

Tag der mündlichen Prüfung: 23.03.2018

"Without feelings insignificant decisions become excruciating attempts to compare endless arrays of inconsequential things."

A. Leckie
Ancillary Justice

Zusammenfassung

Diese Dissertation ist die schriftliche Zusammenfassung meiner Arbeit am Institut für Angewandte Physik. Diese Arbeit lässt sich in zwei, miteinander verknüpfte Teile trennen. Das übergreifende Thema ist dabei die Deposition von Nanopartikeln auf einer kristallinen Wolframoberfläche. Die Experimente wurden im Ultrahochvakuum durchgeführt, um jedwede Kontamination der Proben zu reduzieren.

Zum einen wurden 3d-Metall-Nanopartikel erzeugt und ihr Schmelzverhalten untersucht. Dabei wurde die Arbeiten meiner Vorgänger, Furkan Bulut und Wolfgang Rosellen, an Eisen, Eisen-Kobalt und Kobalt auf Nickel-Eisen-Legierungen ausgedehnt. Hier wurde die bestehende Nanopartikelquelle ACIS verwendet.

Der andere Teil dieser Arbeit beschäftigt sich mit dem Aufbau und Inbetriebnahme der Magnetronsputterquelle. Diese Nanopartikelquelle selbst und ein zugehöriger Massenfilter waren vor Beginn der Arbeit beschafft worden. Hierfür habe ich eine Ultrahochvakuumkammer entworfen und aufgebaut. Diese Kammer wurde im Laufe der Promotionsarbeit schrittweise verbessert und an wechselnde Anforderungsprofile angepasst.

Hierbei zeigten die Nanopartikel beim Erwärmen ein sukzessives Schmelzverhalten (*unrolling carpet*). Dies steht im klaren Gegensatz zu den Ergebnissen meiner Vorgänger, die eine Umformung der gesamten Partikel beobachtet hatten. In der Folge wurden weitere Experimente durchgeführt, um eine mögliche Kontamination der Oberfläche als Ursache für die Diskrepanz auszuschließen. Hier lag der Schwerpunkt auf den Oberflächenverunreinigungen, die bei der Arbeit mit Wolframkristallen am ehesten auftreten könnten. Dies umfasst Kohlenstoff, welcher sich beim Erwärmen von Wolfram an der Oberfläche ansammelt, und Sauerstoff, welcher zum Entfernen des Kohlenstoffs in die Kammer eingeleitet wird oder in Form von Lecks in die Vakuumkammer gelangt sein könnte. Beim Anbieten von Kohlenstoff und Sauerstoff wurden weitere Oberflächenstrukturen erzeugt. Die Nanopartikel zeigten in der Folge ein geändertes Verhalten, welches aber nicht mit den Beobachtungen meiner Vorgänger übereinstimmt.

Die Herausforderung bestand nicht zuletzt darin, den begrenzten Platz im Labor, die begrenzten Mittel und die generellen Anforderungen des Ultrahochvakuums in Einklang zu bringen. Generell hat sich gezeigt, dass die Magnetronsputterquelle in der Lage ist, Nanopartikel aus einer Vielzahl an Materialien zu erzeugen und dabei eine große Bandbreite an verschiedenen Partikelgrößen bereitzustellen.

Die Nanopartikel beider Quellen wurden auf Wolfram-Substrate deponiert und dort mit Rastertunnelmikroskopie untersucht. Andere Substrate sind dabei auch möglich, wie in den Masterarbeiten von Kariman Elshimi (auf einer rekonstruierten Stickstoff-Kupfer-Oberfläche) und Wolfram Gilbert (auf Graphen) gezeigt wurde.

Summary

This dissertation is the written summary of my work at the Institute of Applied Physics. This work consisted of two separate, but nevertheless related, parts. The overarching topic therein is the deposition of nanoparticles on a tungsten crystal surface. All experiments were carried out in an ultra-high vacuum (UHV) environment. This was necessary to minimize the contamination of the samples.

One part was the production and deposition of 3d-metal nanoparticles. My predecessors, Furkan Bulut and Wolfgang Rosellen, began with iron, iron-cobalt, and cobalt particles and I have been extending this work towards nickel-iron alloys. The available nanoparticle source ACIS was used.

The other part of my work was the construction and implementation of the magnetron sputtering source. This nanoparticle source itself and its mass-filter had been purchased prior to this thesis. I've designed and installed a suitable ultra-high vacuum chamber. This chamber was optimized over time and adapted to changing requirements.

The nanoparticles exhibited a gradual melting behavior upon heating. This is known as *unrolling carpet* and it is in strong contrast to the reshaping of whole particles as observed by my predecessors. Further experiments were carried out to determine a possible cause of this discrepancy. One explanation could be a contamination of the crystal surface. The focus was on contaminations which are typically associated with tungsten crystals. This includes carbon and oxygen. Carbon agglomerates at the surface when tungsten is being annealed. Oxygen is being used to remove the carbon and could also reach the surface through leaks in the vacuum chamber. The introduction of carbon and oxygen gave rise to further surface structures. This had a significant effect on the behavior of the nanoparticles. This behavior was, however, different from the results of my predecessors.

The limited lab space, limited supplies and the general requirements of UHV-operations provided a challenging work. It has been shown that the magnetron sputtering source is capable of producing a wide range of particle sizes from a number of different materials.

Nanoparticles from both sources were deposited on tungsten substrates and examined by scanning tunneling microscopy. Other substrate are possible as well, as it was shown in the master theses by Kariman Elshimi (on a reconstructed nitrogen-copper surface) and Wolfram Gilbert (on graphene).

Contents

1 Introduction

Nanoparticles are small objects whose size in each direction is in the range of nanometers.

Nanoparticles can be approached in two different ways. One deals with bulk material and the other deals with single atoms. The former is characterized by a *macroscopic* length-scale and its properties can be easily accessed. The latter is characterized by the eponymous *atomic* length-scale and its properties are described by quantum-mechanics.

The size of nanoparticles and clusters is between these two ranges. Clusters are ranging from 2 atoms up to approximately 1000 atoms. Nanoparticles are larger and have a diameter that is ranging from a few nanometers up to several hundred nanometers.

The distinction between nanoparticles and clusters is drawn based on their size-dependent properties. *Each-atom-counts* is characteristic of clusters, which means that the addition of one atom can change a cluster's properties discontinuously. A well-known example is the *bucky ball* made of exactly 60 carbon atoms. Similar structures with 59 or 61 atoms cannot exist [1, sec. 15.4].

The properties of nanoparticles are changing continuously with size and these properties are approaching bulk-like values for large sizes.

The size is determining a nanoparticle's attributes in several ways. One way is the formation of a shell-like structure, similar to the electron shell of atoms or to atomic nucleus. This is a characteristic of (small) clusters.

Another way is the plasmon resonance, i.e. illumination by light leads to a coherent oscillations of the nanoparticle's conduction electrons. The associated resonance frequency can be in the visible spectrum. This is well-known for gold nanoparticles which have been in use since roman times to give glass a red color [2]. This effect is also present in modern displays where e.g. CdSe particles between 1.5 and $5\,\mathrm{nm}$ can provide higher contrast and brightness compared to more traditional displays. These *quantum dots* can emit light or fluoresce as a result of illumination [3].

Other properties are a result of the larger surface-to-volume ratio of small particles. This is particularly useful to increase the chemical reactivity for e.g. catalysis.

This thesis is focused on the production and study of nanoparticles made of iron, cobalt, nickel, and their alloys. The nanoparticles were produced with two different sources: An arc cluster ion source (ACIS) and a magnetron sputtering source. The nanoparticles were deposited on different surfaces for further treatment (i.e. heating) and examined by scanning tunneling microscopy (STM). Deposition, treatment, and examination were all taking place under ultra-high vacuum condition. Ultra-high vacuum is necessary to minimize the contamination of samples.

The scientific work during my doctorate can be split in two major parts: One part was the construction of a new nanoparticle source. This magnetron sputtering source, which had been previously acquired but was not yet functional, had to be equipped with its own vacuum chamber and all systems necessary for sample preparation. The other part was less engineering-based and more focused on the physics of nanoparticles. The emphasis was on the influence of the nanoparticles' composition on their properties and the role of the substrate.

The outline is as follows: Chapter 2 is an introduction to the scientific background of this thesis. The focus is on the physical systems and effects that I have encountered during my research. I will introduce the magnetic and structural properties of nanoparticles and the properties of related bulk materials, i.e. magnetic 3d-metal alloys, will be discussed afterwards.

The substrates, i.e. the nanoparticles' supports, are obviously important. Therefore tungsten and its carbon and oxygen induced reconstructions are covered. This includes the discussion of atoms on surfaces. Subsequently I will broaden the discussion on agglomerations of atoms (i.e. nanoparticles) on surfaces.

The discussion of the broader topics emphasises on textbook cases while the specifics, that are related to this doctorate, are discussed in relation with recent results of different groups. The scientific background concludes by introducing the prior results of this research group, i.e. the results of Fe, FeCo, and Co nanoparticles on tungsten and a case of a highly contaminated tungsten surface.

Chapter 3 is an introduction to this work's experimental background. The ultra-high vacuum system will be discussed, followed by an introduction of the two main measurement systems, STM and low-energy electron diffraction (LEED). The preparation of the different substrates (for the deposition of nanoparticles) are covered subsequently. A brief overview of the arc cluster ion source is followed by a more detailed discussion of the magnetron sputtering source. The chapter concludes with a section about materials and methods, where the experimental procedures are introduced. An integral part of these procedures are the STM measurements, since the STM was the most import measurement tool for this thesis and proper data evaluation is crucial to obtain credible results.

The measurements will be discussed in chapter 4. Nanoparticle preparation and sample treatment will be specified for each measurement. This also includes the discussion of the results and of possible explanations. The differences and similarities of my results and the reports of my predecessors will be discussed. The differences between the two nanoparticle sources and their influence on the measurement are part of this.

A conclusion is given in chapter 5. The chapter will provide an outlook about remaining questions.

2 Scientific background

The topic of my thesis is supported nanoparticles and this chapter strives to highlight their fundamental aspects. The preparation of such a system is straight forward: bulk material gets evaporated and the resulting vapor is cooled to the point where nanoparticles are condensing. This process is similar to the formation of hail in the earth's atmosphere. These nanoparticles are still suspended in the vapor phase. The deposition on a surface, i.e. a *support*, simplifies the further treatment and examination.

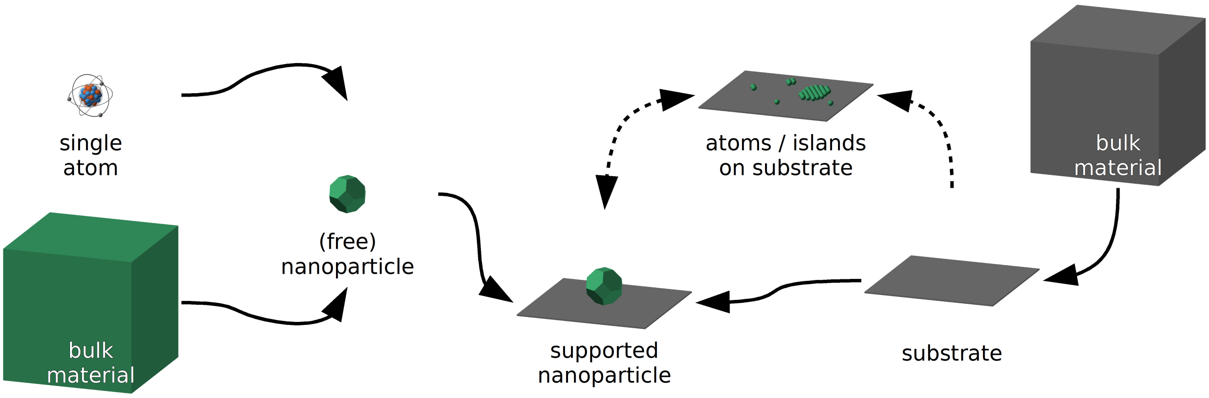

Figure 2.1: The fundamental aspects of supported nanoparticles can be explained by considering its constituents: Nanoparticles are at the threshold between bulk material and single atoms. The nanoparticles' support is the surface of bulk material. Atoms and islands on surfaces also share properties with the much larger nanoparticles on surfaces.

Figure 2.1 sketches the fundamental aspects of a supported nanoparticle. One approach to understand nanoparticles is the properties of single atoms as well as bulk material. Section 2.1 will discuss the properties of (free) nanoparticles with an emphasis on magnetic and structural properties. This includes textbook cases as well as recent research results concerning specific systems.

The bulk materials that were used for nanoparticle production will be introduced afterwards in section 2.2. The focus is on alloys of 3d-metals.

The next aspect of supported nanoparticles is their support, which means that a nanoparticle is embedded in a matrix or located on a substrate. This thesis focuses on the latter case. Section 2.3 will hence introduce the properties of tungsten and its oxide and carbide reconstructions.

The rather complex interaction between the nanoparticles and their support is the final aspect. A simplified approach is the behavior of small-scale systems on substrates, i.e. single atoms and thin films. This will be covered in section 2.4 and it will pave the way to section 2.5 about nanoparticles on surfaces. This includes the general properties, the influence of the deposition process and the post-deposition treatment.

The technical aspects of the nanoparticle production as well as the theoretical background of the scientific instruments (e.g. STM, LEED) are covered in chapter 3.

2.1 Nanoparticles and clusters

The following section will give an introduction to nanoparticles and clusters. Fundamental physical properties on the one hand and results from experimental and theoretical research on the other hand will be introduced. The focus is on magnetic as well as structural properties and nanoparticles from NiFe alloy.

2.1.1 Magnetism of nanoparticles and clusters

The magnetism of bulk alloys will be introduced in section 2.2.3. It should however be noted that macroscopic objects are usually not homogeneously magnetized. Magnetic domains, each with uniform magnetization, will form. The magnetic properties of nanoparticles will be covered in this section. Several factors contribute to the formation of domains on small scales. The most important contributions stem from the crystallographic anisotropy and the form anisotropy of a particle. A magnetization vector will point along a crystallographic easy axis when then particle is spherical and no external field is present.

A small nanoparticle will exhibit a single domain with an external stray field. This stray field increases when the nanoparticle increases in size up to a point when it is energetically favorable to form multiple domains. This transition depends on the energy required to form magnetic domain walls and the energy gained by the reduction of stray fields.

The nanoparticles that have been produced during the work of this thesis are smaller than $20\,\mathrm{nm}$. These small particles have a single domain of uniform magnetization and are also referred to as *Stoner-Wohlfarth*-particles.

Crystallographic structure, form and external influences of a nanoparticle may result in several energetically equivalent states. The simplest case, i.e. uni-axial magnetic anisotropy, leads to two equivalent states with anti-parallel orientation. A certain energy ΔE is required for the transition from one state to the other. If the thermal energy $k_\mathrm{B}T$ is similar to ΔE, then the magnetization can change spontaneously and will immediately reorient depending on external fields. This is called *superparamagnetism*. The switching rate ν for the spontaneous reorientation can be calculated with the Néel-Brown law

$$\nu = \nu_0 \cdot \exp\left(-\frac{\Delta E}{k_\mathrm{B}T}\right) \tag{2.1}$$

with the attempt frequency ν_0. The critical temperature, at which fluctuations become dominant, is called blocking temperature T_B, i.e. the magnetic state is blocked below T_B. Related to this is the magnetic anisotropy energy. It reflects the tendency of the magnetization to align along a specific direction.

[4–6]

2.1.2 Magnetism of free clusters

Billas et al. [7, 8] examined free clusters of Fe, Co, and Ni, their magnetic moment and its temperature dependence. These clusters were produced by a variable temperature laser vaporization cluster source. The collimating nozzle was adjusted to temperatures between 80 and 1000 K. The beam of collimated particles was passed through a Stern-Gerlach-magnet, photoionized, and subsequently detected by a time-of-flight mass spectrometer. The clusters' magnetic moment was determined as a function of temperature and cluster size. Ferromagnetism was found at all sizes. The smallest clusters, below 30 atoms, had a magnetic moment similar to single atoms.

Larger clusters had a decreased magnetic moment at 78 K. Oscillations of this were attributed to surface-induced spin-density waves. The magnetic moment approached the bulk-value at 150 Ni atoms. This corresponds to three atomic shells. Co and Fe approached bulk-value at 450 and 550 atoms respectively. This corresponds to four to five shells.

The magnetic moment decreased (independent of cluster size) with increasing temperature. Nickel clusters ($T_{\mathrm{C,\,bulk}} = 631\,\mathrm{K}$) retained a low magnetic moment for all sizes even at 700 K. Similar behavior was found for iron ($T_{\mathrm{C,\,bulk}} = 1043\,\mathrm{K}$) and cobalt ($T_{\mathrm{C,\,bulk}} = 1394\,\mathrm{K}$). Changes of the magnetic moment of Fe for different sizes indicated a phase transition from bcc to fcc. This occurs at 1150 K for bulk-iron but the transition was shifted to lower temperatures as cluster size decreased. The fcc phase is (in comparison to bcc) characterized by a low magnetic moment.

2.1.3 Magnetism of supported clusters

On the one hand free particles offer a good way to examine the propagation from single atoms to bulk without outer disturbance. Supported and embedded particles on the other hand are more suitable for technological applications. Two approaches exist to support particles as they can either be created from the gas phase and then deposited or they can aggregate from single atoms on a crystal surface. The interaction between the particle and its support influences the particle's properties and thus the magnetic anisotropy energy. Possible factors are hybridization, geometric changes as a result of the deposition, diffusion, alloying, and interaction between (adjacent) particles. [9]

Gambardella et al. [6] examined cobalt atoms and clusters on Pt(111) at low temperature. X-ray magnetic circular dichroism (XMCD), i.e. the difference between X-ray absorption spectra (XAS) of parallel and antiparallel photon helicity with respect to an applied magnetic field, was used to determine the magnetic properties. One advantage of XMCD is the possibility to discern between orbital moments and spin moments. This is an advantage over a Stern-Gerlach-magnet which will only yield the total magnetic moment. The clusters' sizes ranged from 3 to 40 atoms and had an increased orbital momentum, compared to single atoms. The orbital momentum decreased with increasing cluster size. A strong anisotropy, indicated by an increased XMCD signal at the out-of-plane magnetization, was observed. This has been attributed to the reduced coordination of surface ad-atoms, which leads to the localization of 3d-electrons. This increased the local density of states at the Fermi level and thus the spin-orbit energy. This is a contribution to the stronger magnetic moment.

Bode et al. [5] examined Fe islands of different shapes on Mo(110). These islands of 200 to 600 atoms had an out-of-plane magnetization that was examined by low-temperature spin-polarized scanning tunneling microscopy (SP-STM). The direction of magnetization was derived from the $\mathrm{d}I/\mathrm{d}U$ signal. Superparamagnetic switching was observed for individual islands. Elongated islands were switching 10 to 100 times faster than compact islands.

Edmonds et al. [10] examined Fe clusters of 300 to 475 atoms (1.89 to $2.20\,\mathrm{nm}$) after their deposition on highly-oriented pyrolytic graphite (HOPG). XMCD measurements yielded a $4\,\%$ increase in spin momentum and an $80\,\%$ increase in orbital momentum in comparison to single atoms. The increased orbital momentum was once again connected to the narrowing of the d-band and an increase in the density of states at the Fermi level. Other factors included spin-orbit coupling and reduced quenching due to the reduced symmetry.

Larger Fe nanoparticles have been investigated by Bansmann and Kleibert [11]. They were produced by an arc cluster ion source (see section 3.5), size-selected between 6 and $12\,\mathrm{nm}$, and deposited on ferromagnetic surfaces. Two methods were employed to determine the magnetism: Transverse magneto-optical Kerr effect (T-MOKE) in the soft X-ray regime and XMCD. Ni(111) and Co(0001) films were grown on W(110) to provide the in-plane magnetized substrates. $12\,\mathrm{nm}$ large Fe nanoparticles on the Co film and their element-specific hysteresis curves were recorded. A ferromagnetic coupling of the particles to the film was found and has been attributed to the film's exchange field. The ratio of orbital moment to spin moment was decreasing with particle size. The largest particles of $12\,\mathrm{nm}$ had an orbital-to-spin-moment ratio of almost twice the bulk value. FeCo nanoparticles ($7.5\,\mathrm{nm}$) were investigated on Ni(111)/W(110). Spin moments and orbital moments of both Fe and Co were enhanced compared to their respective bulk values.

2.1.4 Nanoparticle structure

A number of factors influence the structure of a nanoparticle, which includes the overall form and the internal lattice structure. Alloy nanoparticles may form complex structures due to the relative distribution of the different atomic species. The substrate is (once again) an important contributor to all properties.

This section will briefly introduce the formation of nanoparticles from the gas phase. The first step is usually the creation of metal vapor from bulk material. This may be done by heating, sputtering, laser ablation or other means. The vapor then needs to cool down for the atoms to agglomerate and to form clusters and nanoparticles. The cooling process is facilitated by the introduction of an inert gas. [9]

More details on the technical process can be found in sections 3.5 and 3.6.

Particle form and Wulff's theorem

A first approach to describe the form of a single crystal nanoparticle is *Wulff's theorem* [12]. According to this, the form of a crystal is determined by the speed at which its facets are growing. This includes the growth along the surface normal and the tangential spread of the surface. The latter is influenced by the growth adjacent facets. A direct result of this simple model is, that fast growing facets are spreading slower and vice versa. The resulting form is one of minimized total free surface energy, where the surface energy γ_i of each single facet i is proportional to its distance from the crystal center h_i:

$$\frac{\gamma_i}{h_i} = \text{constant} \tag{2.2}$$

The resulting equilibrium forms of the fcc and the bcc lattice at low temperature are shown in figure 2.2. The fcc structure's truncated octahedron is terminated by 8 $\{111\}$ facets and 6 $\{100\}$ facets. This form can be further defined by two integers which represent the number of atoms at the different edges. n is the number of atoms at the edge of two $\{111\}$ facets and m is the number of atoms at the edge of a $\{100\}$ facet. n and m are equal for macroscopic crystals. m tends towards zero on the nanoscale which corresponds to the disappearance of the $\{100\}$ facets. The previously hexagonal $\{111\}$ facets become triangular.

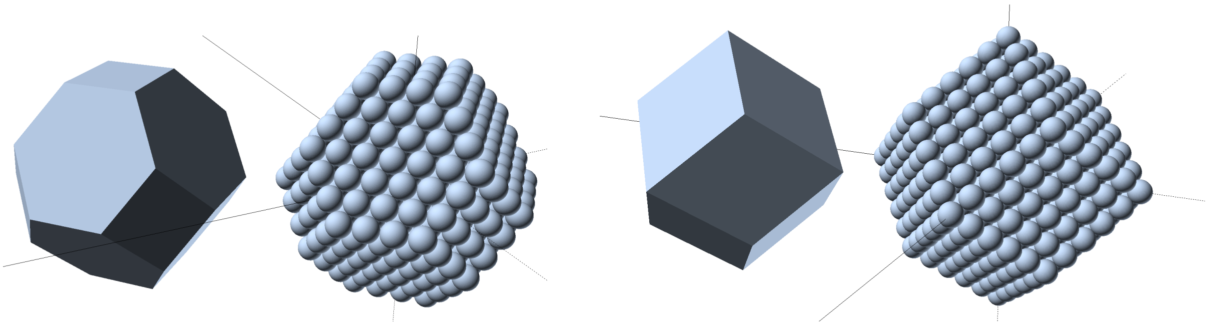

(a) An fcc crystal's truncated octahedron. The solid polygon (left) is featuring 8 hexagonal $\{111\}$ facets and 6 quadratic $\{100\}$ facets. The hard sphere model (right) is made of 586 atoms with $n = m = 4$.

(b) A bcc crystal's rhombic dodecahedron. The solid polygon (left) is featuring 12 rhombic $\{110\}$ facets and the hard sphere model (right) is made of 671 atoms.

Figure 2.2: Equilibrium forms of free particles according to Wulff's theorem. Lines indicate $\langle 100\rangle$-like axes.

A higher temperature increases the surface anisotropy and the equilibrium form gets rounded. The relevance on the nanometer scale and the influence of the substrate have been discussed in detail by Henry [13].

The discussion above is based on the assumption of an equilibrium form. Different contribution, e.g. an inhomogeneous influx of material, will affect the geometry [12]. Nanoparticles from the gas phase are grown far from equilibrium. Their surface structure is a result of the kinetics of crystal growth: A flat surface offers no adsorption sites and will grow very slowly. A kinked surface or, to a degree, a stepped surface offers adsorption sites and spontaneous growth is possible.

Baletto and Ferrando [14] used molecular dynamics (MD) simulations to determine the structure of transition and noble-metal nanoparticles up to sizes of 40 000 atoms. The simulated materials were Ag, Cu, Au, Pd, and Pt. All of these have fcc structure in bulk-material. A general trend was found for all materials concerning favorable structures. For Cu the transition from icosahedral to dodecahedral (to truncated octahedral) occurred at 1000 (1500) atoms. The transition from dodecahedral to truncated octahedron occurred at more than 30 000 atoms. The other materials showed the same trend but at smaller sizes. The truncated octahedron has been identified as an fcc structure while the other forms are associated with non-crystalline structures.

Barke et al. [15] produced large silver nanoparticles (several hundred nanometers) from a magnetron sputtering source (see section 3.6). Femtosecond pulses from a soft X-ray free-electron laser were scattered at individual, free nanoparticles and a wide variety of particle structures could be identified in the scattering patterns. These structures included those associated with fcc crystals, such as a truncated octahedron, and decahedral and icosahedral structures, which are not associated with low-index fcc facets, as well. High aspect ratios were also observed.

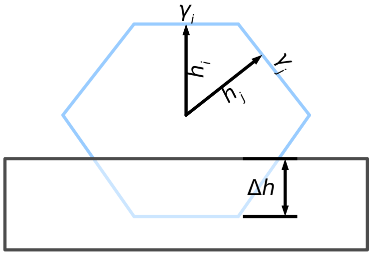

Figure 2.3: Equilibrium form of a supported crystal according to the Wulff-Kaishew theorem. The truncation Δh is proportional to the adhesion energy E_{adh}. Adapted from [13, fig. 2].

The *Wulff-Kaischew theorem* introduces the adhesion energy E_{adh}, i.e. the energy required to separate the crystal from a substrate. It yields the equilibrium form of a crystal on a substrate. The surface wetting is increased as the crystal gets truncated. The relation between truncation Δh (see figure 2.3) and the adhesion energy can be expressed as

$$\frac{\Delta h}{h_i} = \frac{E_{\mathrm{adh}}}{\gamma_i} \tag{2.3}$$

2.1.5 NiFe: clusters and nanoparticles

Nickel-iron alloy has an already complex behavior on the macroscopic scale (see section 2.2.2). Nanoparticles of nickel-iron have even more complicated magnetic and structural properties.

This subsection will give a short overview concerning NiFe nanoparticles and clusters.

Structure

The structure of small NiFe clusters with high concentration of Ni was examined by Parks et al. [16]. Clusters of 13 to 53 Ni atoms were prepared and the nitrogen adsorption was analyzed. Less nitrogen was adsorbed when a single Ni atom at the surface was replaced by Fe, while an Fe atom inside the clusters did not alter the adsorption. The clusters were created in a pulsed laser vaporization source from an alloy-target. The nitrogen adsorption took place in a flow-tube reactor. A reflectron time-of-flight mass spectrometer was used to determine the clusters' mass and possible Fe content. Clusters of 13, 19, 20, 23, 26, and 48 to 53 atoms were analyzed. The $Ni_{25}Fe_1$ cluster had a distinctly different form in comparison to Ni_{26} while the forms of all other Ni clusters were unaffected from the Fe replacement. These small clusters showed (poly-)icosahedral packing.

Magnetism

Margeat et al. [17] synthesized NiFe nanoparticles in a wet-chemical environment. The $(2.8\pm0.3)\,\mathrm{nm}$ small particles exhibited a polytetrahedral structure, possibly as a result of β-Mn structure, a cubic structure with 20 atoms per elementary cell. Larger particles, $(3.8\pm0.5)\,\mathrm{nm}$ in size, exhibited an fcc structure with bulk-like parameters. Clusters of both sizes were assumed to have Fe enrichment on the surface, a Ni core and an intermediate NiFe shell.

The magnetization was $(1.69\pm0.05)\,\mu_\mathrm{B}$ per atom, which is identical to the bulk value. The anisotropy energy was $K = 2.7\cdot10^5\,\mathrm{J\cdot m^{-3}}$, which is slightly less than that of Fe nanoparticles but a hundred times higher than bulk value. The blocking temperature was $T_\mathrm{B} = 17.6\,\mathrm{K}$.

DFT calculations

Theoretical studies of free NiFe clusters from first principles were done by Teeriniemi et al. [18]. These density functional theory (DFT) calculations covered clusters of 145 to 147 atoms which was equivalent to $1.5\,\mathrm{nm}$ in size. Fe_{145} favored a bcc structure. The switch to icosahedral structure occurred at approximately $Ni_{0.65}Fe_{0.35}$. Fcc was energetically unfavorable for all compositions. The relative distribution of atomic species has also been analyzed. The Fe atoms accumulated at the second outermost shell when the Ni content was high. Increased Fe concentration shifted more Fe atoms to sites below the edges and surfaces sites. The most stable cluster in this size range had a Ni core, a surrounding NiFe shell, and Fe atoms on the surface.

Clusters of approximately $2.0\,\mathrm{nm}$ size were simulated as well. The low surface-to-bulk ratio and changed surface sites made these clusters generally more stable. Bcc was still preferred at low Ni concentrations. $60\,\%$ nickel concentration was sufficient to create stable fcc alloys. The icosahedral structures were metastable at intermediate concentrations. Fe enrichment in the first sub-surface layer was similar to the previous findings.

The largest clusters at $3.0\,\mathrm{nm}$ size were dominated by fcc geometry. A $Ni_{600}Fe_{323}$ cluster featured a structure of alternating layers enriched by Fe or Ni, which is similar to bulk structure.

Catalyst for SW-CNTs synthesis

An important application of NiFe nanoparticles is the synthesis of single-wall carbon nanotubes (SW-CNTs) [19]. The nanoparticles were synthesized in a continuous-flow, atmospheric-pressure microplasma reactor while in-situ measurements were used to tune the particles' size and composition. The crystal structure was fcc for pure Ni and $Ni_{0.27}Fe_{0.73}$ alloy (lattice parameter $2.0\,\mathrm{Å}$ and $2.1\,\mathrm{Å}$ respectively). Coexistence of fcc and bcc occurred at $Ni_{0.5}Fe_{0.5}$ and at higher iron contents.

These nanoparticles were directed into a furnace where they facilitated the synthesis of single-wall carbon nanotubes. This required a $600\,^\circ\mathrm{C}$ atmosphere of $0.5\,\mathrm{sccm}$ acetylene and $50\,\mathrm{sccm}$ hydrogen. The Ni concentration could be used to tune the chirality of SW-CNTs. This has been related to the concentration dependent lattice sites of Fe (see above and [18]).

Other applications

A number of applications exist for FeNi nanoparticles beyond the synthesis of (chiral) SW-CNTs. Another catalytic application is the generation of hydrogen from hydrous hydrazine [20]. Hydrazine is a candidate for hydrogen storage as its complete decomposition releases up to $8\,\%_{\text{weight}}$ hydrogen. NiFe would offer a cheap alternative to more expensive noble metals.

CO methanation is also possible [18, 21]. Nickel surfaces serve as catalysts for the reaction of CO and $3H_2$ to CH_4 and H_2O. A double-stepped Ni surface, which may be found on nanoparticles' edges, can reduce the chemical bond of CO when hydrogen is present. The resulting CO-H is an intermediate form in the above mentioned reaction.

2.2 Alloys

This section will give a very brief overview over bulk material made from more than one metallic species. Its properties can also give insight into nanoparticles with similar composition.

The most common crystal structures for metallic elements are bcc, fcc, and hcp. These structures however do not reflect the complex electron configuration of the constituting atoms. The individual bonding between atoms, as a result of different electron configurations, determines the structure of multi-element compounds.

2.2.1 Terminology

Any mixture of metallic constituents is often called an alloy, but this designation is not always correct. **Alloy** designates a mixture of two or more metals and is characterized by structural disorder. An alloying compound may, depending on various factors, substitute atoms in the metallic lattice or it may occupy interstitial lattice sites. This can result in a wide-ranging structure of different grains.

A subgroup of alloys are **solid solutions**, which are formed when the constituting atoms differ by less than 15 % in size. The result is a lattice structure where each lattice point is occupied by an atom of either species. A solid solution has a wide range of possible mixing ratios. This is also called a substitutional solid solution.

An interstitial solid solution forms when small atoms occupy interstitial defect sites in a host lattice without changing this lattice.

An **intermetallic compound** is characterized by a fixed stoichiometry. The constituent atoms form distinct chemical bonds and assemble in a crystal lattice. This lattice has a short range order which gives a clear distinction to alloys. Covalent bonding may dominate over metallic bonding.

[23, 24]

2.2.2 Magnetic 3d-metal alloys

The properties of Fe, Co, and Ni are of special interest because these three elements and their alloys are the only materials that exhibit collective magnetism above room temperature. The alloys of FeCo, NiFe, and NiCo will be briefly introduced because

FeCo was the primary material of the previous doctorates, NiFe has been extensively used during this doctorate and NiCo was used briefly.

Nickel-iron

Nickel-iron-alloys are particularly interesting because of their magnetic properties and their related thermal-expansion characteristics. The most prominent alloys are Mu-metal and Invar. The former, also known as *Permalloy*, contains roughly 70 to 81 % nickel and is characterized by a high magnetic permeability and low coercivity, which makes it an ideal material for magnetic shielding. The latter is $Ni_{0.36}Fe_{0.64}$, which is characterized by a very low coefficient of thermal expansion.

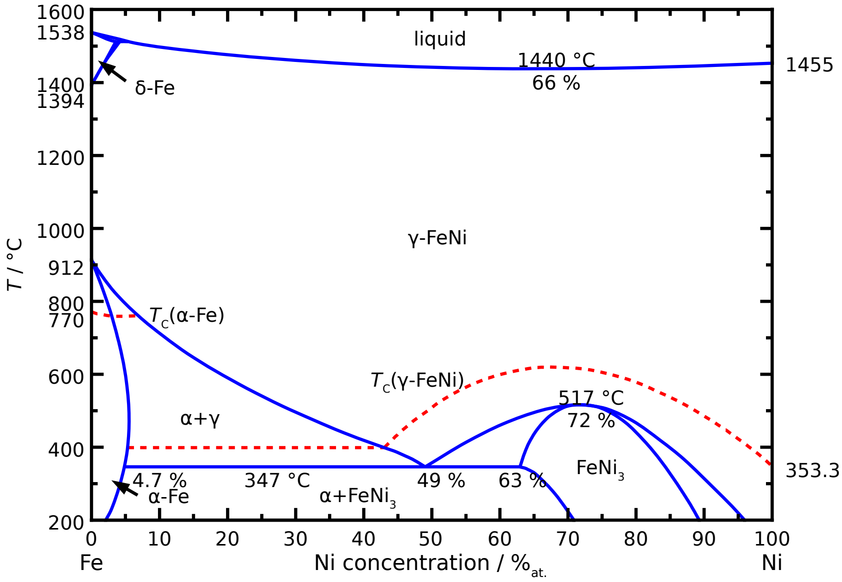

Figure 2.4: Phase diagram for (bulk) NiFe alloy. Curie temperatures are indicated by red, dashed lines. Adapted from [25, fig. 1] and [26, fig. 4.17].

Three different NiFe alloys were in use during this thesis: Commercial grade *Permenorm* with approximately 50 % Ni-content, high purity $Ni_{0.50}Fe_{0.50}$, and high purity $Ni_{0.25}Fe_{0.75}$. *Permenorm* had a purity of approximately 95 % while the high purity alloys were 99.9 % pure.

The phase diagram of NiFe alloy is shown in figure 2.4. The predominant phase is the γ-phase, which is, similar to austenite γ-Fe, a solid solution with an fcc structure. α-Fe only occurs for a Ni-fraction below 5 %, but an α+γ-phase exists for medium temperatures below 49 % Ni-fraction. A bcc structure exists below 347 °C. This phase will be obtained regardless of the cooling rate. [25, 27, 28]

Iron-cobalt

A bcc solid solution can be formed from iron and cobalt. The lattice parameter is 2.85 Å for the $Fe_{0.5}Co_{0.5}$ mixture.

The alloy used for nanoparticle production had a Vanadium content of 2 %, but lattice structure and lattice parameter are not significantly influenced by this. [28–30]

Nickel-cobalt

Nickel and cobalt atoms form a solid solution with fcc structure as long as the nickel amount exceeds $30\,\%$. $Ni_{0.5}Co_{0.5}$ has a lattice parameter of approximately $3.53\,Å$ and a density of $8850\,kg{\cdot}m^{-3}$. Additional superlattice ordering has been observed for Ni_3Co and NiCo. [28, 31]

2.2.3 Magnetic properties

The modern understanding of magnetism is based on the concept of spins: The movement of an electron (or any electric charge) results in an orbital magnetic moment and an electron's relativistic description in an external electromagnetic field gives rise to its spin magnetic moment.

More general, the magnetic properties of iron, cobalt, and nickel are a result of energy minimization. Electrons at the Fermi surface are transferred from the spin-down band to the spin-up band. The additional electrons in the spin-up band have an increased kinetic energy. This increase is usually energetically unfavorable but it may be overcompensated by obtaining Coulomb energy. The so-called *Stoner-criterion* for ferromagnetism gives a quantitative description of this condition. This *spontaneous spin splitting* is energetically favorable for Fe, Co, and Ni.

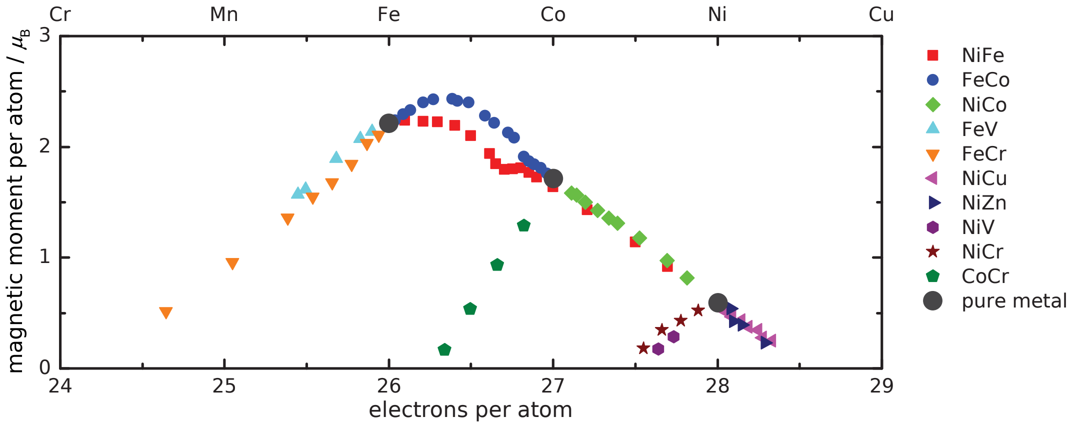

Figure 2.5: Slater-Pauling curve. Adapted from [4, fig. 3.12].

The saturation magnetization for 3d-metals and **alloys** is shown in figure 2.5. This is also called *Slater-Pauling curve*. Binary alloys of a ferromagnetic and a paramagnetic metal show linear behavior: The pure ferromagnet exhibits the maximum magnetization and the magnetic moment per atom decreases linearly when the paramagnetic amount increases. NiFe and NiCo have an (almost) linear characteristic. FeCo alloy has a maximum of almost $2.5\,\mu_B$ at $Fe_{0.7}Co_{0.3}$, i.e. this alloy has a higher saturation magnetization than the pure ferromagnets.

The kink in the curve of NiFe that occurs at approximately $37\,\%$ iron (8.7 electrons per atom) is a result of the fcc-bcc phase transition. [4, 5, 26]

2.3 Tungsten related surfaces

This section will present the defining properties of tungsten. Its oxide and carbide reconstruction have been used as well and they will be presented in the following subsections.

2.3.1 Tungsten

Tungsten was used most often as a substrate to support the nanoparticles.

Tungsten, symbol W, is a transition metal and has a melting point of $3422\,^{\circ}\mathrm{C}$. It crystallizes in a body-centered cubic structure with a lattice parameter of $316.5\,\mathrm{pm}$. Different tungsten surfaces have been studied since the 1960s when ultra-high vacuum became widely available and opened the door to clean surfaces. Among others, the low index-planes – i.e. (100), (110), and (111) – can be prepared [1, 32–34]. Figure 2.6 shows the surface structure for a bcc(110) facet in a hard sphere model. The bcc(110) facet has a centered rectangular lattice and features the highest surface density of all crystal planes of tungsten. Two W(110) planes have a distance of $223.8\,\mathrm{pm}$ (see section 3.7.1). The surface energy of the (110) surface is given as $4.005\,\mathrm{J{\cdot}m^{-2}}$ based on density functional theory [35].

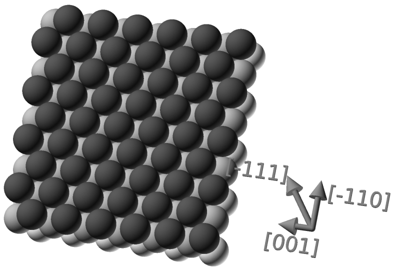

Figure 2.6: Hard sphere model for the (110) surface of a bcc crystal.

The influence of the surface energy's landscape on the diffusion of adsorbates is outlined in section 2.4.1.

W(110) is used as a substrate in surface sciences because of its high melting point and its low chemical reactivity. W(110) also has a relatively easy cleaning procedure (see further below) and does not undergo a surface reconstruction.

2.3.2 Tungsten carbide

The contamination of tungsten with carbon atoms was initially discovered by chance because freshly cut W(110) surfaces would not exhibit the expected LEED pattern. The observed pattern (figure 2.7) was identified by Stern [36] as an R$(15{\times}3)$ reconstruction of carbon.

This structure is a common result of carbon agglomeration at the (110) surface. Flash annealing at $T = 2000\,\mathrm{K}$ will evaporate all contaminants except carbon [37]. Chemical means – usually annealing in oxygen atmosphere – are a feasible approach to remove the carbon (see section 3.4.1 for experimental details).

It was originally proposed, given the LEED pattern, that the C atoms were forming a superlattice on the W(110) surface. Further studies based on LEED [38], X-ray diffraction [39], and Auger electron spectroscopy (AES) [40, 41] gave rise to different models. Bode et al. [42] were the first to publish atomically resolved STM-images with an observed unit cell of $(1.30{\pm}0.07)\,\mathrm{nm} \cdot (0.79{\pm}0.02)\,\mathrm{nm}$. The unit cells appeared as lines with a spacing of $1.3\,\mathrm{nm}$ at wide-area, low-resolution scans. Their proposed model, which

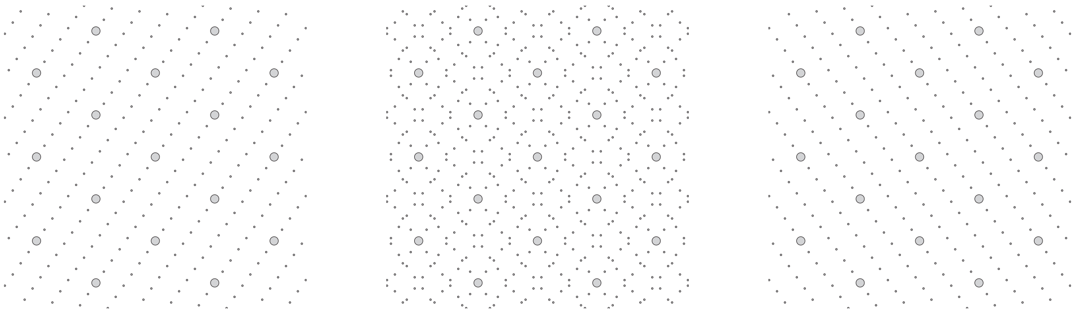
(a) 1st domain (b) superposition (c) 2nd domain

Figure 2.7: Diffraction patterns of the R(15×3) structure. W(110) spots are represented by large dots, small dots represent the reconstruction.

is also consistent with the results of the aforementioned publications, assumes that the carbon atoms are incorporated in the surface without any stoichiometry. The periodic deformation of the surface is caused by atoms being shifted normal to the surface plane to minimize the total surface energy.

A second reconstruction, R(15×12), can also form on W(110). However its preparation requires either a significantly higher preparation temperature [42] or a sudden cool-down from annealing [37]. The R(15×12) reconstruction has not been observed during the work on this thesis and the reader is encouraged to consult the aforementioned literature for more details.

2.3.3 Tungsten oxide

More than 60 years ago, Germer and May [43] used LEED to produce several reconstructions of oxygen on W(110) where the formation of the possible reconstructions depends on the amount of oxygen offered and the temperature.

When W(110) is exposed to oxygen at **low temperature** (between 300 and 1000 K), the oxygen dosage influences the surface reconstruction and one of three different LEED patterns will occur [43–45]. These patterns are related to half, three-quarters, and full coverage of oxygen. The associated reconstructions are p(2×1), p(2×2), and p(1×1) respectively. The last being almost identical to the pattern of clean W(110). The p(2×1) structure was observed after exposure to 1.6 L, while as much as 160 L were required to create the p(2×2) structure and 300 L for p(1×1). W(110) has four possible adsorptions sites (figure 2.8(a)): on-top *1*, center or long-bridge *2*, short-bridge *3*, and threefold-hollow *4* where the last two exhibit site degeneracy. The system's resulting degeneracy was studied by Wu et al. [46]. They also reported on the phase diagram which is shown in figure 2.8(b).

The respective surfaces were observed using STM by Johnson et al. [47]. Low coverage (Θ = 0.1 ML) lead to p(2×1) domains in the vicinity of step edges while a short order orientation along the [001] direction was found on terraces.

Oxygen exposure of W(110) at **elevated temperatures** results in a different set of surface reconstructions. Germer and May [43] gave a systematic overview of the different structures as observed in LEED. These structures occurred depending on oxygen exposure and temperature. Additional flash annealing lead to further structures. The most

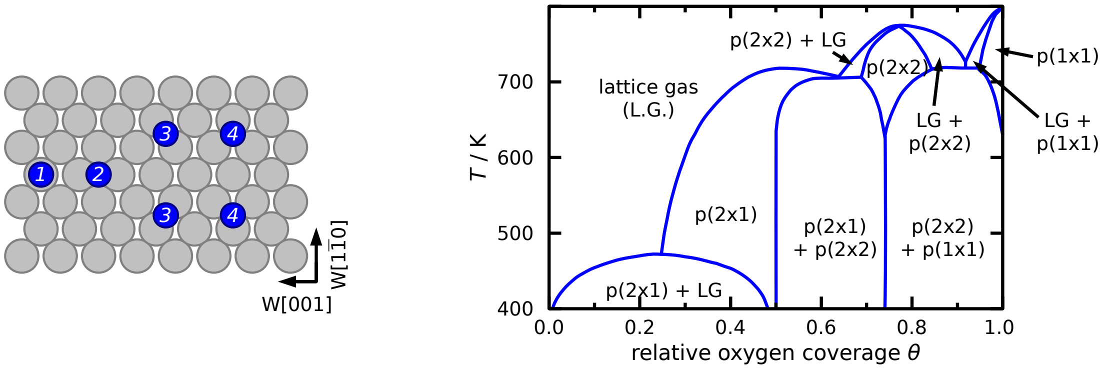

(a) Adsorption sites of O on W(110): *1* on-top, *2* center, *3* short-bridge (both sites), *4* threefold-hollow (both sites).

(b) Phase diagram for O/W(110).

Figure 2.8: Oxygen on tungsten. (b) adapted from [46, fig. 2a].

commonly found structure is the c(14×7) which was created by oxygen exposure of approximately 75 L at 1250 K. This would degrade to a c(21×7) structure at 1400 K, to a c(48×16) structure at 1650 K, and to a c(2×2) structure at 1800 K. Flashing at 2000 K was sufficient to restore the W(110) surface. The $c(48\times16)$ was produced by flashing a half monolayer at 1600 K at $p_{O_2} = 10^{-9}\,\mathrm{Torr}$. Additional structures were found in more recent studies as outlined by Radican et al. [48].

The c(14×7) structure is also called (1×1)×12 as it is assumed to be a superstructure of site-exchanged (1×1) domains with a regular 12-fold periodicity. The oxygen atoms are sitting in two equivalent threefold-hollow sites (*4* in figure 2.8(a)). This structure has domains along the W$\langle\bar{1}12\rangle$ direction. Some sources report orientations along W$\langle\bar{1}13\rangle$ or W$\langle\bar{3}37\rangle$. A structure along W$\langle 7\bar{7}6\rangle$ has been found too. All these patterns have in common that each consists of two equivalent overlayers. [47–51]

2.4 Single atoms and thin films

Adsorbates on a crystalline surface may grow in an oriented way. This is referred to as *epitaxy* or thin film growth when a coverage of one monolayer is exceeded. The growth is driven by thermodynamics and kinetic behavior. The former is responsible for general trends with regard to the surface energies. The latter is limiting the growth rate and results in non-equilibrium conditions. [1]

The deposition of individual atoms (or molecules) is a common approach to thin film growth. Several techniques exist, such as atomic layer deposition and sputter deposition. If a nanoparticle sits on a surface, then it may move as whole. A high surface energy will limit the particles' movement while a low surface energy can facilitate it. The former has been repeatedly observed for nanoparticles on tungsten [29, 52–55]. The latter was observed for example on graphene [56].

The general kinetics of nanoparticle movement will not be discussed because this thesis' nanoparticles were found to be immobile. The melting of nanoparticles (see section 2.4.2) strongly depends on the properties of the substrate. A number of differences exist between the growth of a thin film from individual atoms (e.g. atomic layer deposition) and by melting nanoparticles. The most striking difference is the distribution of source material. Evaporation will result in a stochastic distribution of atoms. The diffusion of these atoms is also called *intrinsic diffusion* because it lacks sources and traps. Nanoparticle deposition results in the stochastic distribution of these nanoparticles which serve as sources of atoms and the resulting diffusion is called *mass transfer diffusion*. [1, chap. 13]

The diffusion of atoms is one of the driving mechanisms behind the formation of surface structures.

2.4.1 Diffusion on W(110)

The structure of the substrate is an important factor for surface diffusion and its *crystallographic anisotropy* may reflect in a growing thin film. The W(110) surface will be discussed here as it is most relevant for this thesis.

Figure 2.9 shows the possible diffusion directions of adatoms on W(110). A single, free atom *1* can hop in any of the ⟨111⟩ directions. The direct hopping along ⟨001⟩ and especially along ⟨110⟩ is energetically unfavorable because it leads over on-top positions. An atom *2* will therefore not move along the island's edge because this would involve the on-top position. This atom may detach from the island which means that ⟨110⟩ edges do not grow. An atom *3* at a ⟨111⟩ edge may move along the island. The atom may stick permanently when it reaches a kink *4*. This mechanism leads to islands that are elongated along the [001] direction and such islands will preferably terminate in ⟨111⟩ edges. Köhler et al. have observed this experimentally for Fe on W(110) at 500 °C and kinetic Monte Carlo simulations were in support of the proposed model [57].

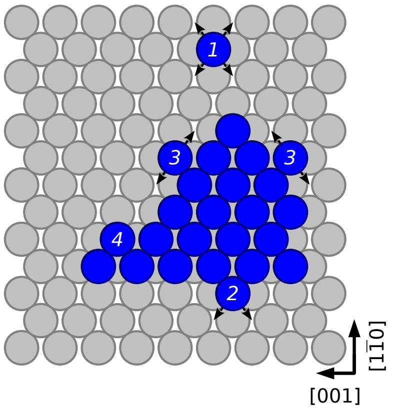

Figure 2.9: Diffusion of atoms ● on a bcc(110) surface ○ and the resulting island shape. Adapted from [57, fig. 4(a)].

The island formation as explained above leads to compact islands because the atoms can move relatively freely. If the temperature is reduced, the energy of atoms *2* and *3* (figure 2.9) may be insufficient for them to leave their respective positions. More generally, any atom that arrives at an island will get stuck because the binding energy at the island will exceed the thermal energy. The *hit-and-stick* regime is the most extreme case where any atom that arrives at an island (or even another atom) will achieve a stable state. The island will form branches of single-atom thickness. [1, sec. 14.2]

An increase in temperature will reduce the number of stable adsorption sites and the diffusion along island edges will increase, i.e. the branches of a ramified island will get wider.

Closed surface layer on W(110)

The formation of islands has been introduced in the previous subsection. So far we have assumed that the adsorbates form a pseudomorphic surface layer. This assumption is correct for homoepitaxy. It is generally only true for low-coverages, when discussing heteroepitaxy. This subsection will exemplary introduce the growth of Co on W(110): Pseudomorphic growth occurs up to a coverage of approximately 70 %.

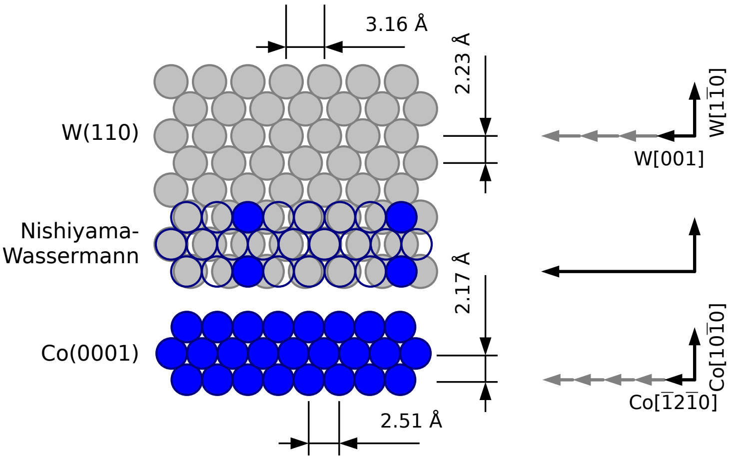

Figure 2.10: Hard sphere model. Bottom ●: Co(0001) equilibrium surface. Top, ●: W(110) equilibrium surface. Center: Strained Co forms a (4×1) structure with respect to W(110). Filled circles ● represent Co atoms in center positions. Empty circles ○ represent incommensurable Co atoms. With material from [58].

Figure 2.10 shows the growth mode that occurs at an increased coverage at which Co[$\bar{1}2\bar{1}0$] is parallel to W[001]. The Co layer is strained by 0.7 % along Co[$\bar{1}2\bar{1}0$] and by 2.7 % in perpendicular direction. This is called the Nishiyama-Wassermann orientation. The unit cell of the superstructure is four times larger than the W(110) orthogonal unit cell (4×1) which is almost equivalent to five unit cells of hcp Co. [58–60]

Morphological anisotropy

The aforementioned diffusion and the subsequent layer growth are further complicated because a W(110) single crystal does not exhibit a single bcc(110) plane, but many (110) terraces that are separated by terrace steps. These steps, which are typically one layer in height, can influence the diffusion on the surface.

The intralayer mass transport is confined to a single terrace and its diffusion mechanism has been explained above. The interlayer diffusion is a mass transport across steps. The energy landscape is, once again, the defining factor. An adatom at the lower side of a step has an increased coordination number, which results in a deeper potential well. This makes it more likely that an adatom will stick to the step. An adatom at the upper side of a step will experience a reduced coordination number because fewer binding partners are available. The resulting energy barrier is also called *Ehrlich-Schwoebel barrier*. The so-called *morphological anisotropy* is the anisotropy under the influence of steps. [1, sec. 13.4 & 14.3]

Geguzin et al. [61] (after [1, sec. 13.4]) examined the morphological anisotropy of a stepped W(110) surface. The steps were aligned along W[001] and the diffusion of Ni atoms at 1170 K was analyzed. They could show that the intralayer mass transfer was significantly higher than the interlayer transfer. The diffusion downstairs was also 50 % higher than upstairs.

2.4.2 Unrolling carpet effect on W(110)

The *unrolling carpet* effect (figure 2.11) is characterized by a stable film that surrounds a source of adatoms (e.g. a high islands or a nanoparticle). The effect is therefore a result of a strong concentration gradient. This film has a sharp boundary. The assumption is, that the first layer is tightly bound (possibly chemisorbed) to the substrate. Atoms in the second layer (on top of the carpet) have a low binding energy (possibly physisorbed) and behave similar to a two-dimensional gas. The first layer may consist of a single monolayer (ML) but it can also be thicker. [1, 62]

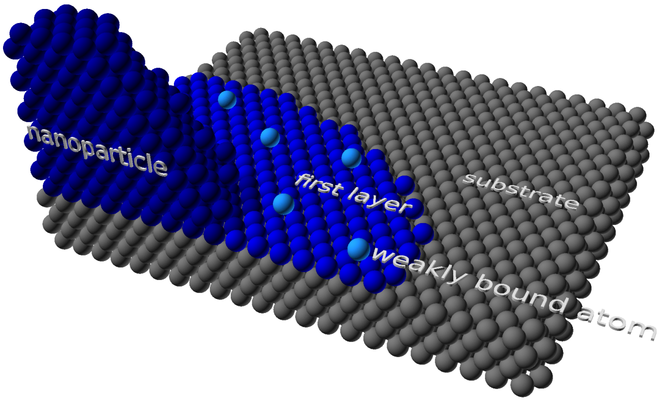

Figure 2.11: Hard sphere model of unrolling carpet: Atoms from a source (e.g. a *nanoparticle*) are spreading over the *substrate*. A tightly bound *first layer* has formed and is being continuously fed by *weakly bound atoms* on top which constitute a 2d-gas.

Butz and Wagner [63] evaporated 2 mm long filaments of Pd on different tungsten surfaces. Their results concerning the W(110) surface will be discussed here. These filaments were 100 to 150 µm wide and 15 to 20 ML high. The subsequent annealing of this quasi-1D system was observed with scanning Auger microscopy (SAM). A heat treatment at 1068 K created a 1 ML high diffusion zone with more than 1 µm in width and a sharp cut-off. Two further treatments (at the same temperature) broadened the diffusion zone and the cut-off softened. The formation of additional layers occurred only after the initial layer was spread out over several micrometers and this could be corrected by a longer annealing time.

This effect was studied by Reuter et al. [62] too. Round 3d-metal dots of 100 µm in diameter and 20 ML thickness were evaporated on a W(110) substrate. Dots of different materials were studied before and after annealing with scanning electron microscopy (SEM) and SAM. Two effects could be observed for Fe dots after annealing at 970 K. The dot was surrounded by a single monolayer (the *diffusion zone*) which was characterized by a sharp cut-off and had a slightly elliptical shape along $W\langle 1\bar{1}0\rangle$. The elongation was more pronounced after longer annealing (18 min vs. 5 min) and was a result of the crystallographic anisotropy (see section 2.4.1). The dot itself was reformed into a tight group of 30 ML high islands which were separated by a 1 ML Fe film. These islands showed an elongation along W$\langle 001 \rangle$. The position of the dot on the substrate (i.e. adjacent step edges) had no observable effect.

The experiment was repeated with dots of Co. The diffusion zone was elongated after 24 minutes at 820 K. The observed dots exhibited different directions of spreading and the authors assume, that the spreading was parallel to adjacent step edges of the substrate. The anisotropy decreased for higher temperatures (at shorter annealing times). 1070 K resulted in a slightly elliptical shape which bore a strong resemblance to the iron's diffusion zones. Ni dots behaved similar to Co dots but at higher temperatures (i.e. 150 K hotter).

The melting of Cu dots lead to other results: Annealing at 820 K transformed the dot into a tight group of islands. In between and around these islands was a 2 ML film of Cu. Around this film was a single monolayer film. Prolonged annealing resulted in the formation of a 1-ML-only film. This had been reported previously by Bauer et al. [64].

2.5 Nanoparticles on W(110)

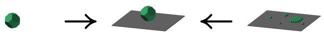

Bulut et al. [29] have examined nanoparticles of Fe and FeCo. These had been produced with the ACIS (see section 3.5) and deposited on W(110) for STM measurements. Deposition on grids for transmission electron microscopy ("TEM grids") allowed for complementary measurements with high-resolution TEM and energy dispersive X-ray spectroscopy (EDX). Different size regimes were obtained by changing the voltage $U_{\text{defl.}}$ of the quadrupole deflector. The height of the nanoparticles was measured by STM and compared with the diameter obtained by HR-TEM. The height on W(110) was between $h = (6.2 \pm 1.1)\,\text{nm}$ at $U_{\text{defl.}} = 250\,\text{V}$ and $h = (8.4 \pm 1.1)\,\text{nm}$ at $U_{\text{defl.}} = 1\,\text{kV}$. The respective diameter was between $d_{250\,\text{V}} = (7.2 \pm 0.9)\,\text{nm}$ and $d_{1\,\text{kV}} = (10.0 \pm 1.3)\,\text{nm}$. The aspect ratio (i.e. the height-to-width ration) was approximately $k = 0.85$. This flattening has been attributed to the surface energy of W(110) which is significantly higher than the surface energy of such nanoparticles. Atoms diffuse immediately after deposition from the particle to the surface.

The composition of these FeCo nanoparticles was analyzed with EDX. The result was $\text{Fe}_{0.55}\text{Co}_{0.44}\text{V}_{0.01}$ with a relative error of 10 %. The HR-TEM revealed $\{110\}$ facets which indicates that the nanoparticles had the form of a truncated rhombic dodecahedron. This features 12 facets of $\{110\}$ and 6 facets of $\{100\}$.

The alignment of nanoparticles on W(110) was studied by Kleibert et al. [65]. Reflection high-energy electron diffraction (RHEED) was used to study Fe nanoparticles with diameters between 2 and 25 nm. All sizes had a bcc structure with a form of a truncated dodecahedron, thus exhibiting $\{110\}$ and $\{001\}$ facets. Larger particles (25 nm and 13 nm) were found to have a bcc structure while exhibiting a random orientation with $\{001\}$ and $\{110\}$ facets facing upwards. Most nanoparticles of 4 nm size were oriented with Fe$[1\bar{1}0]$ pointing along W$[1\bar{1}0]$. This orientation was found for all nanoparticles of 2 nm size.

2.5.1 Influence of the deposition energy

Haberland et al. [66] used MD simulations to study the impinging of a Mo_{1043} cluster on a Mo(001) surface. Kinetic energies of 0.1, 1, and 10 eV per atom were simulated and the structural changes of the cluster and the surface were determined. It was found that a kinetic energy of 0.1 eV per atom caused a slight flattening of the cluster while the substrate remained unaffected. The deposition caused a temperature increase to 596 K. The conditions for a nanoparticle to retain its original form upon deposition are called *soft-landing* conditions. Both nanoparticle sources used during the work on this thesis (see sections 3.6 and 3.5) fulfill this condition. A kinetic energy of 1 eV per atom caused a strong flattening of the particle in conjunction with a maximum temperature of 1799 K. The landing at 10 eV per atom – referred to as *meteoric impact* – caused the propagation of shock waves through the substrate. The cluster was completely destroyed and an impact crater remained at the landing site while the temperature reached 6607 K.

The measurements of Bulut were extended by Rosellen et al. [53, 67] when a voltage U_{sub} was applied to the W(110) substrate. This allowed to accelerate or decelerate the negatively-charged FeCo particles before deposition, i.e. it allowed the tuning of their kinetic energy. Voltages between $U_{\text{sub}} = -10.0\,\text{kV}$ and $+2.5\,\text{kV}$ were applied and the particle height was once again determined by STM. Non-accelerated particles had a height of 7.5 nm. Acceleration of $U_{\text{sub}} = +1\,\text{kV}$, corresponding to $E_{\text{kin}} < 0.1\,\text{eV}\cdot\text{atom}^{-1}$, resulted in an increased height of 8.4 nm. This unexpected increase in height was attributed to the melting of the particles after impact and a subsequent recrystallization. Further acceleration ($U_{\text{sub}} = +2.5\,\text{kV}$, $E_{\text{kin}} \approx 0.2\,\text{eV}\cdot\text{atom}^{-1}$) and slight deceleration ($U_{\text{sub}} = -1.0\,\text{kV}$) caused no change in height. A deceleration at $U_{\text{sub}} = -2.5\,\text{kV}$ lead to a slight increase in height to 7.9 nm, possibly as a result of the reduced deformation during the softer landing. $U_{\text{sub}} = -10.0\,\text{kV}$ was sufficient to repulse all incoming nanoparticles and the substrate remained empty.

2.5.2 Melting of nanoparticles

The melting point of nanoparticles is generally lower compared to bulk material. This is correlated to the higher fraction of surface atoms. Ding et al. [68] have shown in a molecular-dynamics study how clusters are melting. The properties of a Fe_{586} cluster were simulated for heating steps of 50 K between 600 and 1400 K. Three temperature regimes have been found: (1) The cluster was solid up to 850 K. Atoms were increasingly vibrating at rising temperature but kept their original lattice positions. (2) The atoms at the core were close to their original lattice positions while surface atoms (i.e. atoms with reduced coordination number) were diffusing along the surface. This *surface melting* increased up to the melting point (1150 K). (3) This point was accompanied by a sudden collapse of the crystal structure and marks the beginning of the third regime. All atoms were diffusing at this temperature.

For example, Helveg et al. [70] found experimental evidence for surface melting. Nickel nanocrystals were formed by reduction in a reactive atmosphere and observed with TEM. The interaction with carbon-nanostructures in the environment was changing the form of the Ni nanoclusters. Mono-atomic step edges were formed.

Bulut [29, 30] examined the melting behavior of FeCo nanoparticles on W(110). He found no changes at a temperature of 573 K. A temperature of 923 K for one hour reduced the particles' heights below 4 nm. The onset of a bulk-like melting of the whole particle (i.e. not just the outer shell) occurred for some particles at 1023 K and for all particles at 1123 K. The melting occurred as a spreading of the nanoparticles along the

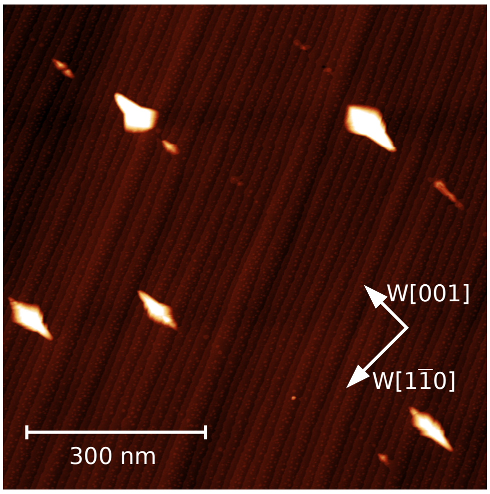

Figure 2.12: Anisotropic form of FeCo nanoparticles on W(110) after annealing at high temperature. 1.0 V; 0.1 nA [69]

W(110) direction (see figure 2.12). Small, one monolayer high islands were spread over the surface.

This was later extended by Rosellen [67] to Fe and Co nanoparticles of similar sizes. The effect was once again observed at high temperatures. An additional effect was found for Fe nanoparticles: 10 minutes of annealing at 640 K resulted in a monolayer of Fe atoms surrounding the nanoparticles. (See section 2.4.2 for details on the mechanism).

The coexistence of anisotropic, complete melting and unrolling carpet in the same system was explained by Rosellen by assuming, that a phase transition would occur at $T_{\text{critical}} = 640\,\text{K}$. Nanoparticles were to recrystallize spontaneously at T_{critical} and orient themselves along the W[1$\bar{1}$0] axis.

Smaller iron nanoparticles were produced as well and annealed for 15 minutes at 600 K. The annealing was repeated several times and the height was determined every time by STM. The initial height of 4.8 nm dropped to 3.0 nm after the first cycle and approached a stable value of 2.4 nm after several more cycles. A further reduction in height was not possible.

2.5.3 Anisotropic elongation on tungsten carbide

The results of the master's thesis of Werner [71] will be discussed in section 4.3.1. His work included a series of deposition tests with the ACIS, too. The goal was to determine the nanoparticle beam's position and the helium's influence on the particle formation. The tests were done on four consecutive days at which the surface contamination of the W(110) visibly increased. As it is not uncommon for quick testing, image quality was of little concern and the images suffered from tip oscillations, double-tips, and various instabilities. The deposition chamber experienced bad pressure ($p_{\text{ana}} \approx 5 \cdot 10^{-9}\,\text{mbar}$) as well. The W(110) substrate was flashed each morning and nanoparticles were deposited afterwards. The STM images (see figure 2.13) revealed elongated structures A after the deposition of nanoparticles P. The elongation was observed directly after deposition (see figures 2.13(a) and 2.13(b)) and also after annealing (30 minutes at up to

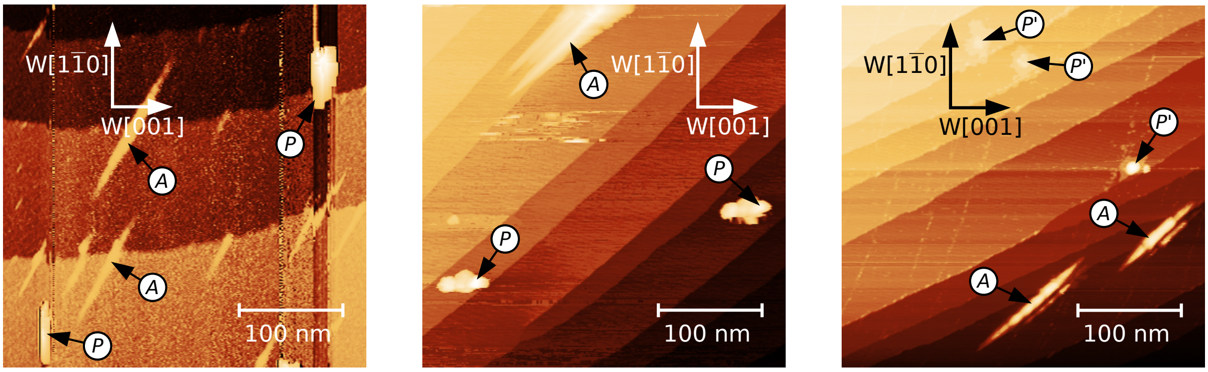

(a) 2^{nd} day: After deposition, without annealing. PtIr-Tip; 1.0 V; 0.8 nA.

(b) 3^{rd} day: After Deposition, without annealing. PtIr-multi-Tip; 0.5 V; 1.8 nA.

(c) 4^{th} day: After annealing for 30 minutes at up to 852 K. Nanoparticles P' showed *unrolling carpet*. PtIr-double-Tip; 0.5 V; 1.8 nA.

Figure 2.13: $Ni_{0.5}Fe_{0.5}$ nanoparticles (P) and anisotropic structures (A) on carbon-contaminated tungsten surface. Differences in alignment are most likely a result of scanner drift. The nanoparticles and elongations were duplicated by the double-tip in the same way. This clearly indicates that the elongations were a real surface-feature and not a result from a malformed tip.

852 K, see figure 2.13(c)). It was roughly parallel to W[1$\bar{1}$1]. These structures have not reappeared since the oxygen annealing at the end of the test series.

The structures A had a height of up to $h_{\mathrm{app.}} \approx 7\,\mathrm{nm}$ and a length of up to $200\,\mathrm{nm}$. Longer structures were also higher. The images that were taken after annealing revealed *unrolling carpet* behavior of the nanoparticles (P'). Despite of the high annealing temperature, the nanoparticles had not completely melted.

3 Experimental background

This chapter will outline the experimental setup that was used for this thesis' work as well as the experimental procedures involved.

A clean surface is a necessity for good results in the field of surface science. A common way to achieve a clean environment is the use of an ultra-high vacuum. Sufficient reduction of pressure reduces the molecular density of the residual gas and thus the number of atoms/molecules that hit the surface. This effect can be expressed by the mono-time, which is the time that is necessary to form one monolayer of adatoms when the sticking coefficient is one[1]. The mono-time depends on temperature, pressure, and molecular species. A mono-time of one hour for air at room temperature requires a pressure of 10^{-9} mbar [72]. Pressure below this value is commonly referred to as *ultra-high vacuum* (UHV).

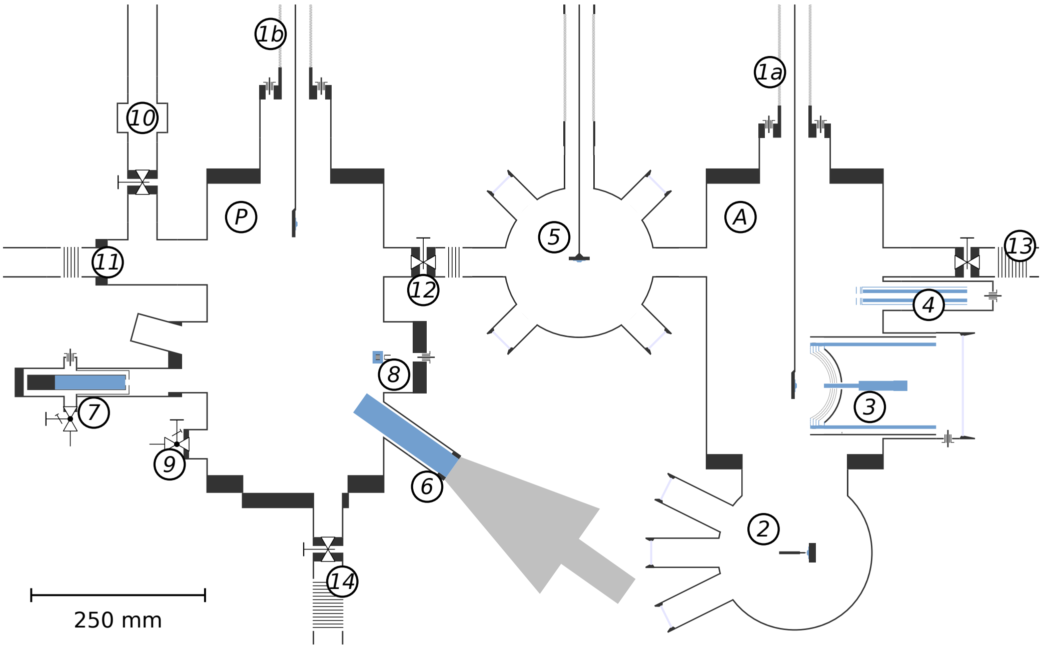

Figure 3.1: Schematic projection to the horizontal plane of the UHV system's main chambers: *A* analysis chamber, *P* preparation chamber, *1* main manipulators, *2* STM, *3* LEED/AES, *4* QMF, *5* MOKE chamber with manipulator, *6* triple evaporator, *7* sputter ion source, *8* electron bombardment heater, *9* leak valve, *10* load lock with magnetic transporter, *11* magnetic transporter for inter-chamber transport, *12* gate valve to separate chambers, *13* connection to ACIS, *14* connection to magnetron sputtering source. The setup from early 2017 is depicted. With material from [72–76].

---

[1] This provides the worst-case scenario. A lower sticking coefficient obviously leads to a lower coverage, thus to a longer mono-time.

3.1 Ultra-high vacuum (UHV)

Common procedures and technologies were applied to reach the UHV pressure range. The reader is encouraged to consult the available literature [1, 72, 77].

The experimental setup to achieve the required vacuum will be outlined in this section. The main parts of the system are two UHV chambers: The preparation chamber and the analysis chamber (a.k.a. STM chamber). A schematic projection to the horizontal plane is shown in figure 3.1.

Each chamber has a Bayard-Alpert type hot-cathode ion gauge and a set of four vacuum pumps. A turbo molecular pump (*HiPace 700*, $S_{\mathrm{N}_2} = 685\,\mathrm{l{\cdot}s^{-1}}$) backed by one dual-stage rotary vane pump ($S = 5.56\,\mathrm{l{\cdot}s^{-1}}$) is employed during pump-down and during high-gas-load operation. A gate valve can isolate each chamber from its turbo pump. An ion getter pump (IGP, *StarCell 300*, $S_{\mathrm{N}_2} = 240\,\mathrm{l{\cdot}s^{-1}}$) maintains the base pressure without disturbing vibrations[2] when the turbo pumps are off. Titanium sublimation pumps (TSP) are installed. These help to keep the pressure down but titanium must not be sublimated when a measurement is taking place because the released titanium would contaminate any sample. The pumping effect of a TSP is shown in figure 3.2[3].

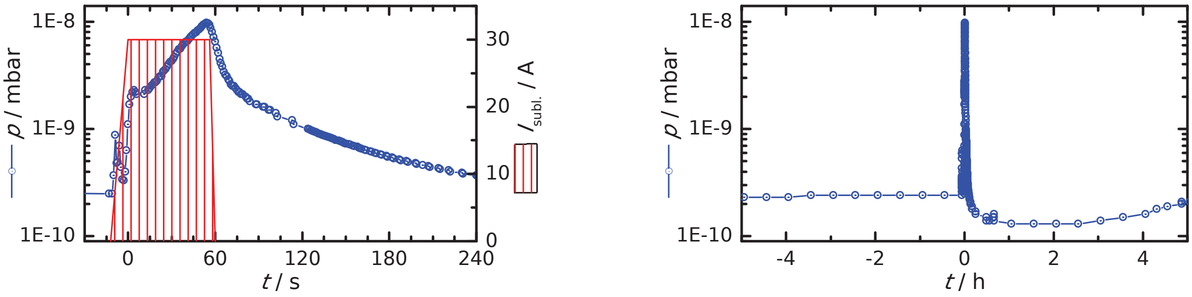

(a) Sublimation current and pressure during a sublimation cycle.

(b) Long-term effect of the titanium sublimation.

Figure 3.2: $p(t)$ curve of a single sublimation cycle.

A manipulator from *Vacuum Generators* with integrated sample heater and type-K thermocouples for temperature measurement (section 3.7.4) is installed in each of the chambers. The maximum continuous heating power is $80\,\mathrm{W}$ which yields a typical temperature of $900\,^\circ\mathrm{C}$. An increase to $90\,\mathrm{W}$ yields $950\,^\circ\mathrm{C}$ but this is limited to intervals of 20 minutes [79].

The **analysis chamber** comes with LEED / AES (*SpectaLEED*, Omicron) and STM (*MicroSPM*, Omicron). These are the main tools for surface analysis. A residual gas analyzer (*Prisma 200*, Pfeiffer) is additionally installed. The chamber has been prepared for the installation of a MOKE setup [80].

The **preparation chamber** is equipped with a triple rod evaporator (*EFM 3T*, Focus) and a sputtering gun (*ISE 5*, Focus) to prepare thin films and clean substrates. An electron bombardment heater is used when temperatures above $900\,^\circ\mathrm{C}$ are required. Gases can be introduced through a leak valve.

---

[2] vibrations pose a challenge during STM measurements

[3] Current is displayed as given by the TSP controller. Other controllers will indicate a different (i.e. higher) current because of their respective current control techniques [78].

Magnetic transporters and wobble sticks are used to move samples between the manipulators and other devices. New samples can be put into the system through a load-lock.

3.2 Scanning tunneling microscopy (STM)

This section will outline the basics of a scanning tunneling microscope. Gerd Binnig and Heinrich Rohrer have developed it in the early 1980s and received the Nobel Prize in Physics in 1986. The underlying physical concept is the eponymous quantum tunneling effect. A fine tip is brought into such close distance to a surface that electrons can tunnel between former and latter. A bias between tip and surface will result in a tunneling current. Its current density j for a situation as in figure 3.3 is given as:

$$j = \frac{D(V) \cdot V}{d} \cdot \exp\left(-A \cdot \Phi_{\mathrm{B}}^{1/2} \cdot d\right) \tag{3.1}$$

where V is the applied bias voltage, $D(V)$ are the electronic densities of state, d is the effective tunneling gap, and Φ_{B} is the gap's effective barrier height. A is a constant factor.

This relation is used in STM measurements: The tip is biased and brought into close proximity of the sample until a current can be detected. Many microscopes, including the one I used, are build such that the surface is facing downwards. The tip is approaching the surface from below (Z-direction) and it is then moved parallel to the surface in incremental steps. A change in current can be attributed to either a change in distance d or a change in the local density of states $D(V)$. This will yield an image of the surface encoded with a convolution of topography and local density of states. Two basic modes of operation exist. The tip is moving only parallel to the surface in *constant-height mode* and the current for each position is recorded and can be converted into a distance by equation 3.1. The *constant-current mode* requires the adjustment of the tip-sample-distance such that the current is matching a preset value. These adjustments in distance are recorded.

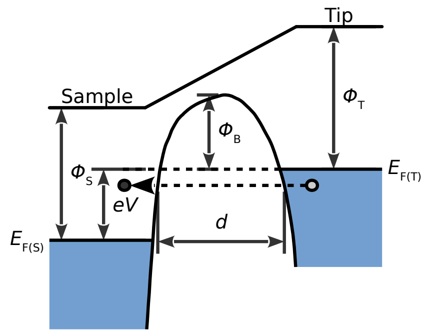

Figure 3.3: Tunneling gap between sample and tip with work function Φ_{S} and Φ_{T} and Fermi levels E_F. A negative voltage V is applied to the tip and the sample's empty states are being probed. Adapted from [1, fig. 7.16].

While constant-height mode has the advantage of fast-imaging, its severe disadvantage is the risk of tip-sample collision. This risk is greatly reduced in constant-current mode because the tip is kept from the sample at an (almost) fixed distance. Readjusting the tip's distance is nevertheless time-consuming.

The resolution is determined by several factors. The precise positioning of the tip, both horizontally and vertically, is one. This is achieved by piezoelectric ceramics which give a resolution of sub-Å over a range of several micrometers. The vertical resolution may also be limited by the current detection (pA-range), but properly shielded, multi-staged current-amplifiers will not worsen the piezo's precision. This puts the vertical resolution into the precision range of the piezo, i.e. sub-Å . The horizontal resolution is limited by the size of the tip, i.e. a structure smaller than the tip cannot be resolved. A perfect tip can terminate in a single atom.

The main components for STM can be derived from this: A tip which is atomically sharp and of well-known composition, a scanner to move the tip with the necessary precision, and an electronic feedback-loop to control the current and voltage of the gap. A computer system is controlling and recording the measurements. Additional requirements are a coarse motion drive to move the tip over distances outside of the piezo's reach and damping systems to reduce mechanical vibrations and electronic noise. [1]

The movement of the tip is typically following a pattern where each line is scanned in X-direction (fast-scan direction) and these lines are stacked in Y-direction (slow scan direction). The tip-sample distance is aligned in Z-direction.

Further details, especially the calibration, possible errors during measurements, and the data evaluation are outlined in sections 3.7.1 and 3.7.2.

3.3 Low-energy electron diffraction (LEED)

Low-energy electron diffraction is a method to determine the structure of a crystal surface. A surface structure may be identical to an equivalent crystal lattice plane in the bulk, but it can differ considerably. The differences are due to a number of reasons, among them surface relaxation, surface reconstruction, and adsorbates. Low-energy electrons have two main advantages when probing surfaces at an atomic scale: On the one hand electrons at $E_{\text{kin}} = 30$ to $200\,\text{eV}$ are surface sensitive because their penetration depth is in the order of a few monolayers [81]. On the other hand the corresponding de Broglie wavelength is similar to the periodicity of atomic dimensions and therefore suitable for diffraction ($100\,\text{eV} \mathrel{\hat{=}} 1\,\text{Å}$).

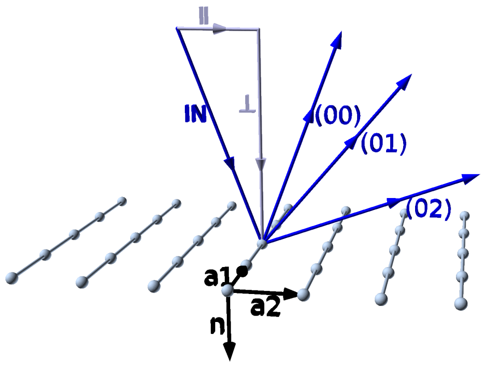

Figure 3.4: A plane (electron) wave is getting diffracted at an ordered surface with surface vectors $\vec{a}_1$ and $\vec{a}_2$. Reciprocal surface vectors are denoted $\vec{a}_1^*$ and $\vec{a}_2^*$.
IN incident beam $\vec{k}_0$ with perpendicular and parallel components.
(00) specular reflection, $\vec{k}^{\parallel}_{00} = \vec{k}^{\parallel}_{0}$,
(01) first-order diffraction, $\vec{k}^{\parallel}_{01} = \vec{k}^{\parallel}_{0} + \vec{g}_{01}$ with $\vec{g}_{01} = \vec{a}_2^*$,
(02) second-order diffraction, $\vec{k}^{\parallel}_{02} = \vec{k}^{\parallel}_{0} + \vec{g}_{02}$ with $\vec{g}_{02} = 2 \cdot \vec{a}_2^*$.
Adapted from [82, fig. 3.2].

Electrons are elastically scattered by the crystal lattice. Elastic scattering of a wave at a crystal lattice can be described by considering conservation of momentum and energy. This yields two relations between incident wave $\vec{k}_0$ and diffracted wave $\vec{k}$:

$$\vec{k} - \vec{k}_0 = \vec{g}_{hkl} \tag{3.2}$$

$$|\vec{k}| = |\vec{k}_0| \tag{3.3}$$

where $\vec{g}_{hkl}$ is a reciprocal vector of the crystal lattice.

Low energy electrons have a typical penetration depth of no more than 10 to 20 Å and the lattice involved in the scattering experiment is therefore mostly two-dimensional. In addition, the de Broglie wavelength of low-energy electrons is in the order of a few angstrom and is as such quite suitable for diffraction on an atomic scale. The reduction to two dimension reduces the conservation of momentum to the in-plane components and the scattering condition becomes:

$$\vec{k}^{\|} - \vec{k}_0^{\|} = \vec{g}_{hk} \tag{3.4}$$

The momentum vector component into / out of the surface is no longer conserved. Figure 3.4 shows the incident and diffracted waves in reciprocal space. [1, 82]

3.3.1 Experimental requirements

The experimental system (see figure 3.5) requires an electron gun (*1*) to produce a narrow beam of monochromatic electrons. The electrons are typically emitted from a hot cathode and a set of adjustable lenses is used to form the electron beam. The hot cathode is usually placed in such a way that its light cannot reach the sample surface.

The beam is diffracted at a sample surface (*2*) and the diffracted electrons are collected on a retarding-field analyzer. This is a spherical sector screen, which consists of four semi-transparent grids (*3*) and a fluorescent screen (*4*). The first (inner-most) grid is grounded to keep the space between sample and screen free from electric fields which could disrupt the imaging. The second and the third grid, the so-called suppressor grids, are at a retarding (negative) potential to reject lower-energy electrons from inelastic scattering. Only a narrow range of elastically scattered electrons can therefore pass the suppressor. The fourth screen is grounded to shield the high potential of to the fluorescent screen (+6 kV). It accelerates the electrons and stimulates fluorescence. The pattern of diffracted electrons can then be observed on the screen. The screen may be observed from the back or from the front.

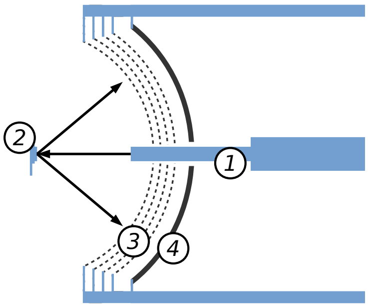

Figure 3.5: LEED instrument: *1* electron gun, *2* crystal surface, *3* four-grid suppressor, and *4* fluorescent screen. With material from [73].

It should be noted that the incident beam has a diameter of at least 0.2 mm. The observed pattern may therefore be a superposition of different surface domains from within the incident beam. [1, 73, 82]

Figure 3.1 (3) shows the position of the LEED in the vacuum chamber. Further details concerning the operation of a LEED system are outlined in section 3.7.3.

3.3.2 LEED pattern

The spots of a diffraction pattern would be infinitely sharp if the measurement would be done on a perfect, rigid, and infinitely extended crystal surface with a perfect device. The deviations of both the substrate and the device from perfection contribute to the widening of the spots. The incident electron energy is not perfectly mono-energetic. This results in a finite distribution of corresponding wavelengths which in return result in a finite distribution of diffraction angles. The incident beam is also not point-like because the electron source has a finite diameter and a finite distribution of angles of incident. Lastly the spatial resolution of the detector is limited. These factors are summarized in the *instrument response function*.

The sample may contribute to wider spots because of its finite size and the finite size of its crystal terraces. Contamination will widen the spots too. Inelastic electron scattering can also contribute.

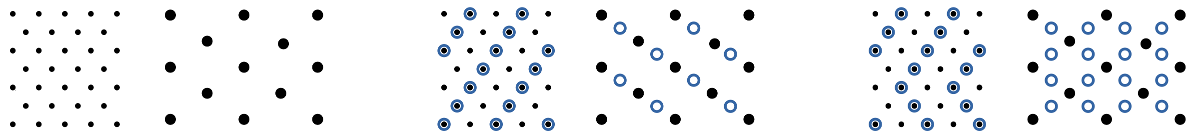

(a) bcc(110) (b) bcc(110)-p(1×2) (c) bcc(110)-p(1×2)+p(2×1)

Figure 3.6: Real space lattices (on the left of each subfigure) and LEED patterns (on the right) of different surfaces.

The pattern itself is (as mentioned before) a reciprocal representation of the surface lattice. The translation of a simple crystal plane is therefore straightforward and can be done easily (see figure 3.6(a)). The back-translation is similar. A more complicated pattern of a p(2×1) reconstruction of bcc(110) is shown in figure 3.6(b). Such a pattern would usually not be observable because two rotational domains co-exist (figure 3.6(c)). Recognizing a superstructure based on a given LEED pattern is significantly more difficult as a number of similar structures may exist. [1, 82]

3.4 Surface preparation

This section introduces the experimental details of surface preparation. W(110) is the most important surface, as it was used for most of the experiments. The other surfaces, i.e. W-carbide and W-oxide, can be prepared from clean W(110).

3.4.1 Preparation of a clean tungsten surface

The experiments in this thesis were based on two tungsten crystals with (110) orientation. These were used as a substrate for thin film growth and for the deposition of nanoparticles.

Rapid heating to a temperature above $2000\,\mathrm{K}$, so called *flashing*, is generally used to prepare a clean W(110) surface. Most contaminants evaporate at this temperature. Only carbon forms stable structures and cannot be removed by mere heating. The resulting W(110)/C-R$(15{\times}3)$ reconstruction was first described by Stern [36]. The carbon can be removed by oxygen annealing. An oxygen atmosphere of 10^{-6} to $10^{-7}\,\mathrm{mbar}$ and a surface temperature of $1500\,\mathrm{K}$ are necessary for the carbon to form CO and CO_2 which can be pumped away. Tungsten oxides are forming in the process. These can be removed by subsequent flashing above $2000\,\mathrm{K}$ [83].

3.4.2 Preparation of tungsten-carbide

As mentioned in the previous subsection (3.4.1), carbon agglomerates on a W(110) surface by diffusion from the bulk and must be removed by oxygen annealing to achieve a clean tungsten surface.

The intentional preparation of tungsten carbide is therefore quite simple: The sample will be annealed to promote the diffusion of carbon impurities from the bulk to the surface. Bode et al. prepared the W(110)/C-R$(15{\times}3)$ reconstruction by heating a tungsten single crystal under UHV conditions at $2400\,\mathrm{K}$. A different reconstruction, R$(15{\times}12)$, was found at $2600\,\mathrm{K}$ [42].

A temperature of $2000\,\mathrm{K}$ was chosen for the work in this thesis and was suitable to provide a reproducible W(110)/C-R$(15{\times}3)$ reconstruction. Only one of the two tungsten crystals was suitable for this work as the other one had been de-carbonized quite extensively as outlined in section 3.7.5.

See section 2.3.2 for details of the tungsten-carbide surface.

3.4.3 Preparation of W(110)/O-p(2×1)

The W(110)/O-p$(2{\times}1)$ surface can be prepared by offering oxygen to a W(110) substrate at room temperature. Oxygen on W(110) may result in one of several surface structures as outlined in section 2.3.3. The p$(2{\times}1)$ structure will occur at intermediary rates of exposure, i.e. several Langmuir. The results of the preparation are outlined in section 4.1.2.

3.4.4 Preparation of W(110)/O-((1×1)×12)

Annealing at approximately $1500\,\mathrm{K}$ in oxygen atmosphere results in the formation of W(110)/O-$((1{\times}1){\times}12)$ as outlined in section 2.3.3. A two step process is required when starting from a contaminated W(110) surface. The first step is cleaning W(110) by flashing, followed by oxygen annealing at $10^{-6}\,\mathrm{mbar}$ and subsequent flashing (see subsection 3.4.1).

The oxygen reconstruction is then prepared at $10^{-7}\,\mathrm{mbar}$. The pressure in the preparation chamber may exceed $5{\cdot}10^{-9}\,\mathrm{mbar}$ after the preparation. A quick transfer of the sample into the analysis chamber is therefore required. The results of this preparation method are shown in section 4.1.3.

3.5 Arc cluster ion source

The continuously-working arc cluster ion source[4] (*ACIS*) has first been described by Methling et al. [85, 86]. Figure 3.7 shows the ACIS itself and figure 3.8 shows its integration into the overall vacuum system. A hollow cylindrical cathode is made from the desired target material. In its center is a copper anode. A bias of several hundred volts is applied to the anode while argon is introduced through the back of the cathode. The resulting pressure is sufficient to spark an arc discharge between anode and cathode. This arc discharge is removing material from the cathode's inner wall. A dense plasma of metallic ions is forming as a result. Three-body collisions of metal atoms and argon remove the heat from the plasma and facilitate the condensation of clusters.

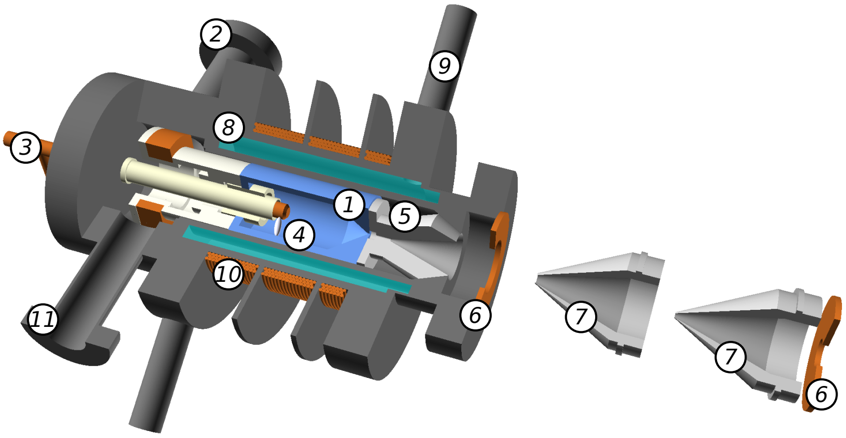

Figure 3.7: Schematic view of the arc cluster ion source. Inert gas is getting injected into the cathode *1* through port *2*. A voltage at the anode *3* has ignited an arc discharge *4*. The arc discharge is removing material from the cathode's inner wall and this material is condensating to nanoparticles and clusters. The gas flow is sweeping these particles through the extender *5*. Two apertures *6* and two skimmers *7* are forming a narrow beam of nanoparticles while removing the majority of the inert gas. The cathode's housing *8* is water-cooled *9* and the anode is water-cooled too. The solenoid *10* can produce a magnetic field which improves the movement of the arc discharge. Port *11* is providing a bypass for faster pump-down.

Several modes of operation are possible, which can be classified by the voltage drop during operation (*cathode fall*). A voltage of 11 to 16 V indicates a *Type I* focal spot. It forms as a result of contamination or oxidation of the cathode's surface. The arc discharge will remove the contaminant and this leads to the *Type II* focal spot. It can only occur on a clean surface and is characterized by a cathode fall of 20 to 25 V. [87]

The gas is leaving the hollow cathode through its front channel and is taking the clusters along. Further growth can occur during the clusters' acceleration. The extender marks the end of the ACIS itself. An adiabatic expansion of the carrier gas leads to further acceleration and cooling. Two skimmers, each equipped with vacuum pumps, collimate the cluster beam and reduce the pressure. The result is a narrow velocity distribution of the cluster beam.

---

[4] The term *continuously-working* should emphasize the difference to the *pulsed* arc cluster ion source (*PACIS*) [84]. It is not a *continuously-working* source in the strictest sense because the operation time of the ACIS is typically limited to a few minutes.

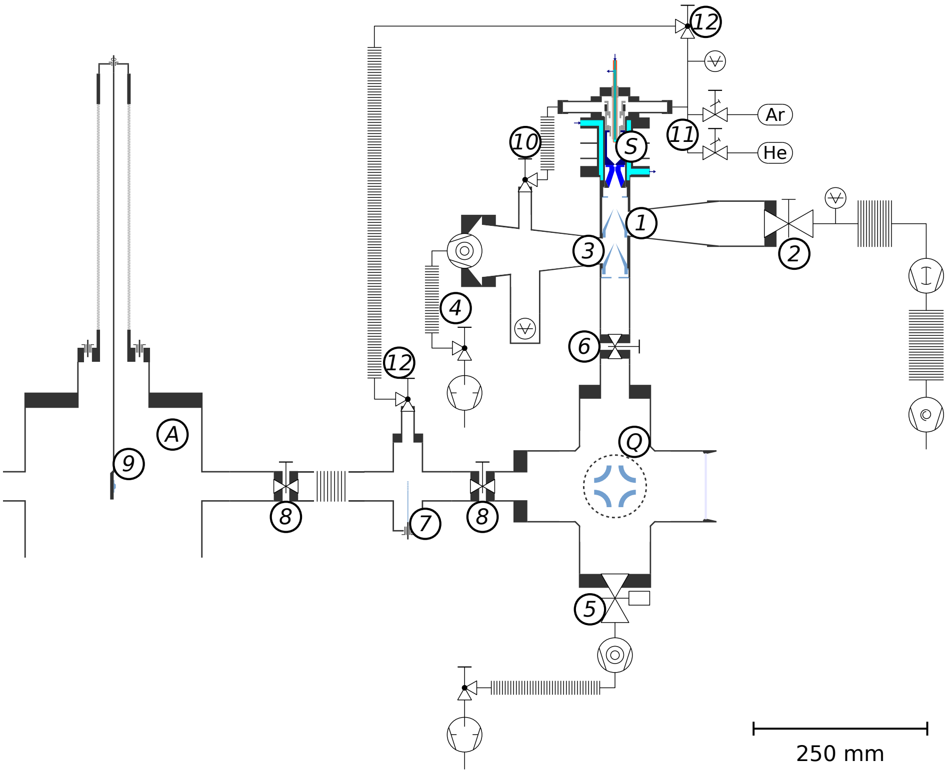

Figure 3.8: Schematic projection to the horizontal plane of the ACIS system:
A) analysis chamber (see figure 3.1 for details),
Q) quadrupole chamber with electrostatic quadrupole and shielding grid (not shown: ion gauge, IGP, TSP),
S) ACIS (see figure 3.7 for details),
1) 1st skimmer,
2) gate valve with roots pump ($42.5\,\mathrm{l} \cdot \mathrm{s}^{-1}$) and scroll pump,
3) 2nd skimmer,
4) turbo pump ($230\,\mathrm{l} \cdot \mathrm{s}^{-1}$) and rotary vane pump,
5) gate valve with turbo pump ($330\,\mathrm{l} \cdot \mathrm{s}^{-1}$) and rotary vane pump
6) gate valve to cut off ACIS from quadrupole,
7) connection tube with grid for current detection, TEM grids can be placed here,
8) gate valves to detach the connection tube,
9) deposition substrate on manipulator,
10) bypass for faster pump-down of the ACIS,
11) gas inlet (argon and helium),
12) bypass for pump-down of the connection tube. With material from [72, 76, 88].

About $50\,\%$ of the clusters are charged [85]. This and the narrow velocity distribution open the way to mass-selection in an electrostatic field. This field is generated by a quadrupole with a voltage $U_{\mathrm{defl.}} = \pm(0\ldots5)\,\mathrm{kV}$. Nanoparticles and clusters of selected size are deflected by $90°$ towards the analysis chamber. The pressure gets further reduced by another pump. A fine grid is connected to a picoampere-meter to measure the current of nanoparticles. The particles are landing on the substrate afterwards. [30, 85, 87, 89]

The tube connection between the chambers can be removed to allow vibration free STM operation. A bypass connects this tube to the end of the ACIS for pump-down after reattachment. Another bypass connects the end of the ACIS to the second stage's turbo pump. Both bypasses must be closed during cluster production. The turbo pumps may operate with separate fore-pumps (as shown in figure 3.8) but a shared rotary vane pump ($S = 4.4\,\mathrm{l{\cdot}s^{-1}}$) is also sufficient[5]. Water cooling of anode and cathode is necessary due to the high-power arc discharge (500 to $1000\,\mathrm{W}$).

3.6 Magnetron sputtering source

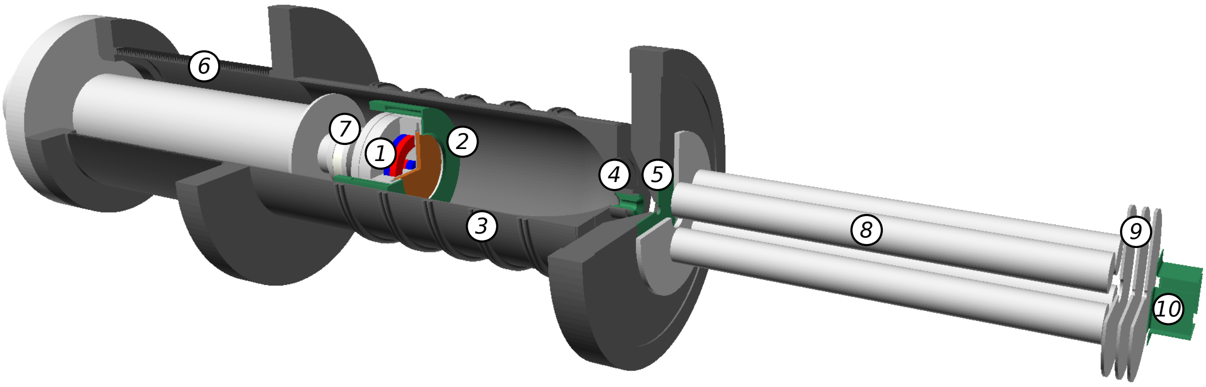

Figure 3.9: Schematic view: Magnetron sputtering source *NCU200U* (*1-7*) and quadrupole mass filter *QMF200* (*8-10*).

1) magnetron (cathode) with internal magnets (red / blue), internal water-cooling (not shown), and sputtering target at the front (copper-colored),
2) anode (green), argon gas is getting injected through the gap between anode and magnetron,
3) water-cooled aggregation region,
4) expansion nozzle (green, exchangeable, different diameters available), exit of the aggregation region to the first pumping stage,
5) aperture (green, exchangeable, different diameters available), entrance to the quadrupole mass filter,
6) edge-welded bellow to adjust the length of the aggregation region,
7) isolator, helium gas is getting injected here,
8) quadrupole rods,
9) triple stack of plates: grounded shield, ion collector plate, focusing lens,
10) XY-steering plates (green).

The magnetron sputtering source (figure 3.9), also called *Haberland-source*, was first employed by Haberland [91]. It is a combination of a magnetron sputter discharge to create an atomic vapor and a gas aggregation region in which said vapor condenses to clusters and nanoparticles. The growth of the nanoparticles depends on diffusion and drift inside the aggregation region. The diffusion is caused by the high pressure and is driving the formation of the nanoparticles through collisions. The drift is caused by the gas flow from the gas inlets to the expansion nozzle (i.e. the outlet) and the growth will stop when the nanoparticles are swept out. In the standard setup (as it is used here) argon gas is introduced into the region directly above the sputter target while helium

---

[5] Beware of accidental venting! [90]

gas is introduced into the aggregation region to facilitate the particle condensation. The resulting sizes are logarithmically-normal distributed (see section 2.1.4).

The flow inside the aggregation region is relatively stable, but this assumption does not hold true when considering the flow close to and inside the nozzle. The properties of the nanoparticles leaving the nozzle have been studied by several groups. Smirnov et al. [92] used an aggregation chamber with an additional electrode around the orifice to generate a secondary plasma in the aggregation region. Kousal et al. [93, 94] used electrostatic deflection plates downstream of the nozzle to widen the particle beam with respect to charge, mass, and velocity. Transmission electron microscopy (TEM) images were taken at different positions in the beam. The spatial distribution of particles is obviously a direct result of the nozzle's form and diameter. They found a velocity range from $30\,\mathrm{m{\cdot}s^{-1}}$ for large particles ($50\,\mathrm{nm}$) to more than $200\,\mathrm{m{\cdot}s^{-1}}$ for particles smaller than $7\,\mathrm{nm}$. The latter was a result of the acceleration inside the nozzle. The particles were either neutral or were carrying a single positive/negative charge.

3.6.1 Sputtering

Sputtering, i.e. the bombardment of a substrate with charged ions, has several applications. All have in common that atoms will be mechanically removed from the substrate. Inert ions are produced by a plasma discharge and accelerated in an electric field. The kinetic energy of these ions must be higher than the binding energy of the substrate, usually 10 to 100 times higher. The pressure (of inert gas) must be low enough to provide a mean free path for the acceleration of the ions and high enough to ignite a plasma. The amount of ions is obviously related to the sputtering yield. [95]

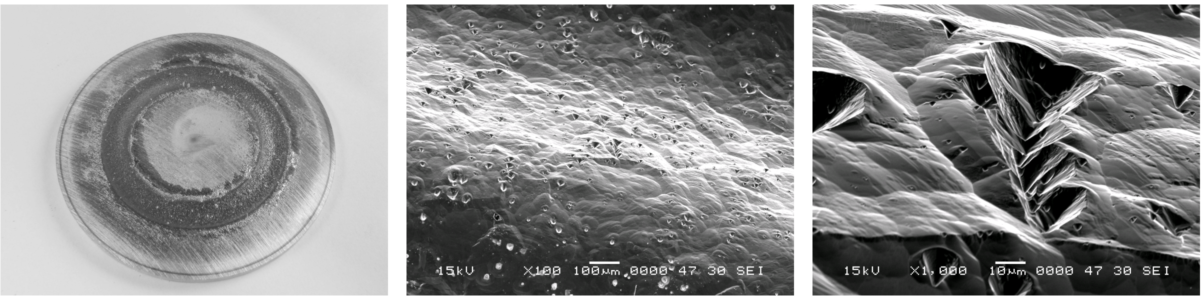

(a) Photo of a Co target: $50.8\,\mathrm{mm}$ diameter.

(b) SEM image of a $Ni_{0.5}Fe_{0.5}$ target: Part of the circular erosion rill.

(c) Magnification of (b): Craters in the erosion rill.

Figure 3.10: Erosion of sputtering targets at different magnifications.

The magnetron sputtering source requires a pressure that is also sufficient to promote the growth of nanoparticles due to collisions between sputtered atoms and the gas (as explained further below). The effect of sputtering on a target is shown in figure 3.10. X-ray fluorescence spectroscopy was used to determine the composition of the $Ni_{0.5}Fe_{0.5}$-alloy targets before and after their use. The composition was unaffected by the sputtering and this is a clear indication that the sputtering yield of Ni and Fe is very similar. The nanoparticles' composition should therefore be identical to the composition of the sputtering target.

Sputtering can also be used to remove impurities from a substrate and thus to obtain a clean surfaces (which usually requires subsequent annealing to heal the surface) and was first described by Farnsworth et al. [96]. This should not be confused with sputtering deposition.

3.6.2 Particle growth

The sputtering process releases atoms (and possibly small clusters) as a supersaturated vapor. This vapor is metastable and three-body collisions occur between two atoms (A) from the sputtering and one atom (G) from the buffering gas. The atoms (A) can form a dimer (A_2, called *nucleus*), when the gas atom removes the excess energy and thus satisfying the conservation of energy and momentum. The dimer may continue to grow via additional collisions. Smaller nuclei may also break up, depending on the experimental conditions. The *critical size* denotes the nucleus' size that it requires to be stable. This process is also called *nucleation*.

Larger clusters will grow from the nuclei by means of four different processes [97, 98]:

- Free atoms (A) may collide with the nuclei (A_n) which is called *attachment of atoms*.
- *Coalescence* happens when smaller clusters evaporate and adjacent larger clusters are growing by absorbing the evaporant. This process occurs close to the critical size (see above) and is also known as Oswald ripening.
- Two liquid drops, nuclei A_n and A_m, may come into contact and form a single, larger drop (A_{n+m}). This is called *coagulation*.
- Two solid clusters may come into contact and form a single, larger cluster, which is called *aggregation*. The primordial clusters may partially retain their structure and thus are forming fractal aggregates. Fractal aggregates were neither observed during this thesis' work nor are there any reports from other groups working with this nanoparticle source [15, 99, 100].

3.6.3 Size distribution

The size of the nanoparticles is determined by the time spent in cooling. This residence time is stochastically distributed, due to the **diffusion** of nanoparticles in the gas and the overall **drift** towards the exit of the aggregation region. The result is a **log-normal** size distribution (e.g. Granqvist et al. [101]), i.e. a Gaussian distribution plotted against an exponential abscissa. The mechanism inside the gas aggregation region was explained by Kiss et al. and validated in numerical simulations [102]. Their model is based on the assumptions, that (1) the growth of a particle is proportional to its surface area and that (2) the residence time inside the grow-zone is log-normally distributed. This holds true when taking both diffusion and drift into consideration.

The log-normal height distribution $f(d)$ can be expressed as

$$f(d) = f_0 + \frac{A}{\sqrt{2\pi} \cdot \ln \sigma} \cdot \exp\left(-\frac{(\ln d - \ln d_0)^2}{2 \cdot (\ln \sigma)^2}\right) \tag{3.5}$$

where d_0 denotes the mean diameter, σ is the standard deviation and A is a scaling factor. f_0 is the vertical offset of the distribution, e.g. the average underground. The size distribution of nanoparticles does not exhibit an underground, i.e. $f_0 = 0$. [101]

The size distribution will retain its log-normal form after mass-filtering since a convolution of a log-normal distribution (from the nanoparticle source) with a Gaussian distribution (from a mass-filter) is still log-normal.

3.6.4 Size selection – The quadrupole mass filter

A quadrupole mass filter (QMF) consists of four parallel rods arranged in a quadratic manner. These rods should have a hyperbolic profile for an ideal field geometry. Actual rods are commonly round cylinders. The radius r_{rod} of each rod is 1.144 times larger than the so-called field radius r_0, i.e. half the distance between opposite rods (see figure 3.11(a)). Opposing rods form pairs of the same potential and a voltage of

$$V_{\text{quad}} = U + V \cdot \cos(\omega \cdot t) \tag{3.6}$$

is a applied between the two pairs.

The full solution of the equations of motion will not be given here [103, 104]. A short outline of the solution will be introduced and the practical applications will be discussed. Two parameters are introduced

$$a = \frac{8 \cdot Q \cdot U}{m \cdot r_0^2 \cdot \omega^2} \tag{3.7}$$

$$q = \frac{4 \cdot Q \cdot V}{m \cdot r_0^2 \cdot \omega^2} \tag{3.8}$$

where Q is the charge of an ion with mass m. These parameters are used to solve the Mathieu equation which describes the ion trajectories. A trajectory is stable if its amplitude is smaller than r_0. An ion with a higher amplitude will touch a quadrupole rod and neutralize there. Stability in x- and y-plane can be considered independently due to the symmetry of the quadrupole. An ion will pass the filter if it fulfills the stability conditions in both planes. The motion upon entering the QMF has no influence on the stability of the trajectory.

Figure 3.11(c) shows the stability diagrams for the parameters a and q. The regions of stable trajectories in x and in y direction are highlighted separately. The regions of overlap (*1*–*3*) corresponds to stability in both directions. Region *1* is of special interest for the operation of a quadrupole. Figure 3.11(b) shows the upper half of this region. Assuming single charged ions and with $a/q = 2U/V$ follows that all masses are aligned on the *operation line* and the masses in the stable region have stable trajectories. Tuning the ratio U/V is changing the resolution $\Delta m/Q$. Δm approaches zero when the operation line is crossing the tip of the stable region at $\frac{2 \cdot U}{V} = \frac{0.237}{0.706} = 0.336$. Any mass of $q < 0.92$ has a stable trajectory when the operation line is horizontal, i.e. $U = 0$. [103–105]

3.6.5 Experimental realization

A commercially available magnetron sputtering source from *Oxford Applied Research* has been installed, tested and utilized during the work of this thesis. The *NC200U* was designed for UHV environments and optimized for high sputtering rates [106].

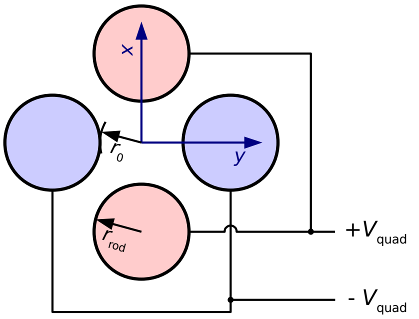

(a) Cross section of cylindrical rods.

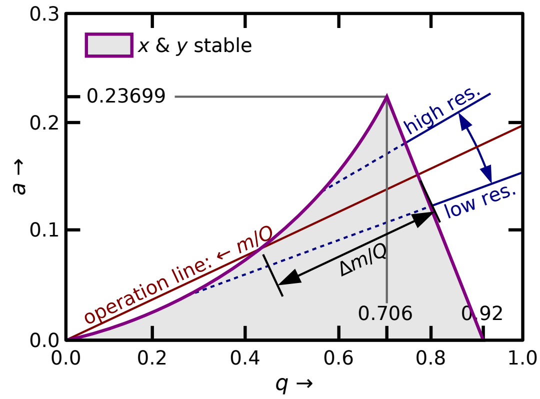

(b) Upper half of stability region 1. The operation line is only determined by the ratio U/V. Adapted from [77, 104, 105].

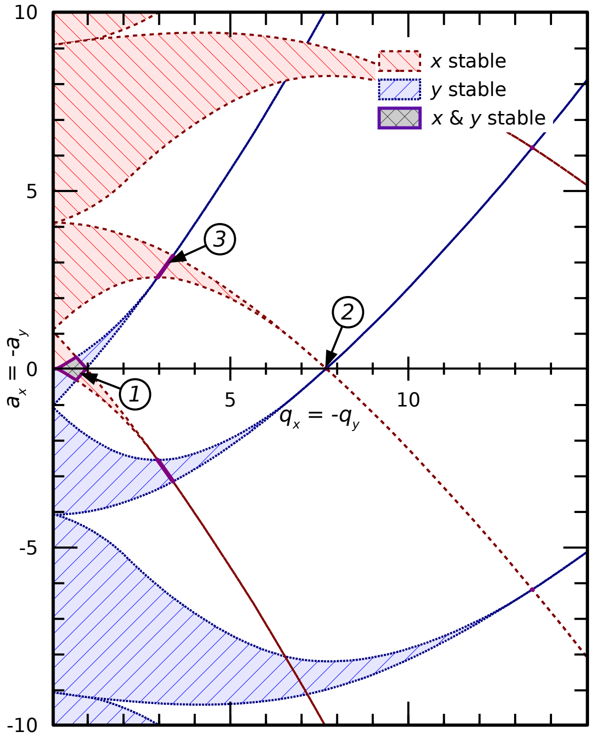

(c) Stability diagram of a QMF. Adapted from [103, 104].

Figure 3.11: Quadrupole mass filter.

A quadrupole mass filter with cylindrical rods is installed downstream of the cluster source. It is a *QMF200* by *Oxford Applied Research* which is designed to analyze and filter the charged particles from the *NC200U* [107].

The parameters of the source can be controlled via computer with the *QUVI2* software provided by *Oxford Applied Research*. This includes all the parameters for the nanoparticle generation, except the aggregation length. The software can also control the QMF. The frequency $f = \frac{\omega}{2\pi} = (3...100)\,\mathrm{kHz}$ and the AC-voltage $V = (1...250)\,\mathrm{V}$ can be adjusted and the software will calculate the corresponding mass. The nanoparticles' atomicity based on the atomic weight and the expected diameter based on the density of the sputter target's material will be calculated as well. The filtering width $\Delta m/m$ can be adjusted between $2\,\%$ and $100\,\%$ and the U-V-ratio is set accordingly.

The necessary deflection voltage of the XY-steering plates was determined experimentally by changing the voltage between 0 and $100\,\mathrm{V}$ for a given particle mass until the current on the sample was maximal. The value was then generalized to

$$V_X = 0.6427\,\mathrm{V} \cdot \frac{n_{\mathrm{Co}}}{1000} \cdot \frac{\Delta X}{1\,\mathrm{mm}} \cdot \frac{80\,\mathrm{mm}}{\Delta Z} \tag{3.9}$$

where V_X is the voltage to deflect a nanoparticle made of n_{Co} Co atoms. The sample is at position ΔX off the central beam and at a distance ΔZ from the deflection plates

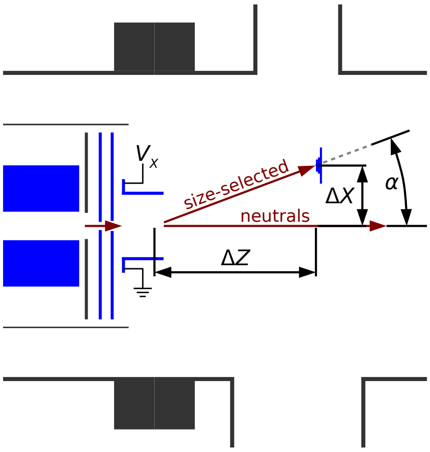

Figure 3.12: Deflection of nanoparticles in X-direction at the exit of the QMF.

(figure 3.12). The face of the quadrupole's exit flange is used as a reference position for the deflection plates. The steering plates for the Y-direction work in the same fashion.

Several different setups have been realized during the work for this thesis, each being an improvement over the previous one. This section will highlight the two latest setups. It should be mentioned that the preparation chamber is not sufficiently equipped to directly attach the cluster source.

Classical setup

Figure 3.13 shows the setup as it was used during the majority of experiments. It features a rather long distance between the QMF *2*, *3* and the substrate for deposition *5* ($\approx 0.8\,\mathrm{m}$). This setup is based on the deposition concept of the ACIS (see section 3.5), i.e. separate vacuum chambers for particle production, mass filtering, and deposition.

The connection between source and preparation chamber *6* has flexible bellows on both sides *7*, i.e. the connection will adjust when the source is repositioned. Thus it is possible to deposit in and outside of the source's central axis. The maximum deflection angle is shown in the figure. The position of the deposition substrate can be checked with a gold-plated mirror[6] inside the connector. This mirror can be retracted so that it is not blocking the particle beam. The connection can be vented and evacuated *8*, *9* without breaking the vacuum of neither source nor preparation chamber. The connector's venting and decoupling is necessary to reduce mechanical vibration of the STM. Ion getter pump (IGP) and titanium sublimation pump (TSP) are preserving UHV conditions when the turbo pumps are off. The bypass *10* can be opened in this case and is enhancing the pumping of the second stage.

Three turbo pump stages are reducing the pressure from the aggregation region to the preparation chamber. Two turbos with $S_{\mathrm{N}_2} = 520\,\mathrm{l{\cdot}s^{-1}}$ turbos[7] *12* are handling the main gas-load ahead of the QMF in combination with a dual-stage rotary-vane pump of $S = 5.56\,\mathrm{l{\cdot}s^{-1}}$. Similar fore-pumps are provided for the $S_{\mathrm{N}_2} = 250\,\mathrm{l{\cdot}s^{-1}}$ turbo *13* after the QMF and the $S_{\mathrm{N}_2} = 685\,\mathrm{l{\cdot}s^{-1}}$ turbo at the preparation chamber (not shown).

---

[6] Special thanks to Stefan Manderla for manufacturing the mirror.

[7] A single *TMU 520* would provide sufficient pumping speed but may not handle the high gas flow.

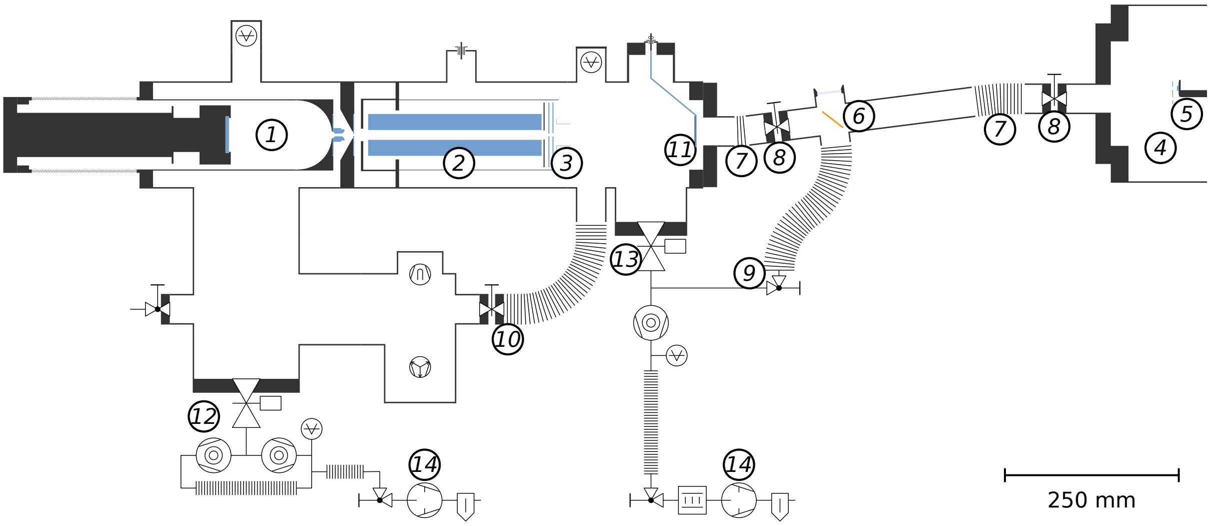

Figure 3.13: Schematic view of the *classical setup*:

1) magnetron sputtering source (see figure 3.9 for more details),
2) quadrupole mass filter,
3) ion collector plate, focusing lens, XY-steering plates,
4) preparation chamber (see also figure 3.1),
5) fixed aperture, deposition substrate on manipulator,
6) connection tube with retractable mirror for substrate inspection,
7) bellows to adjust the connection tube,
8) gate valves to detach the connection tube,
9) bypass with valve for connection tube,
10) bypass with valve for faster pumping of the 2nd stage,
11) shutter,
12) 1st turbo stage ($2\times\ 520\,\mathrm{l{\cdot}s^{-1}}$) with gate valve,
13) 2nd turbo stage ($250\,\mathrm{l{\cdot}s^{-1}}$) with gate valve,
14) fore-pumps. With material from [72, 76, 88, 108].

One advantage of this setup is the easy integration into an existing vacuum system, because a small flange (CF40) is sufficient at the preparation chamber and the sample transfer is kept simple. The differential pumping stage at the QMF is reducing the operational pressure at the substrate by a factor of about 20.

The major drawbacks are the long distance from QMF to substrate and the small angle to separate charged from neutral particles. The former does not pose a problem in itself other than a reduced particle yield. The latter was considered negligible. Other groups had reported smaller angles (e.g. $2°$ in [109]) and initial testing indicated a complete separation at an angle of $\alpha = 1.6°$ (see section 3.6.7). It should be noted that this does not hold true for all cases even at $\alpha = 5°$ (e.g. sections 4.2.1, 4.2.2, 4.2.3). It should also be noted that the widening of the (neutral) particle beam depends on the diameters of the magnetron's nozzle and aperture. Diameters larger than $3\,\mathrm{mm}$ require additional consideration.

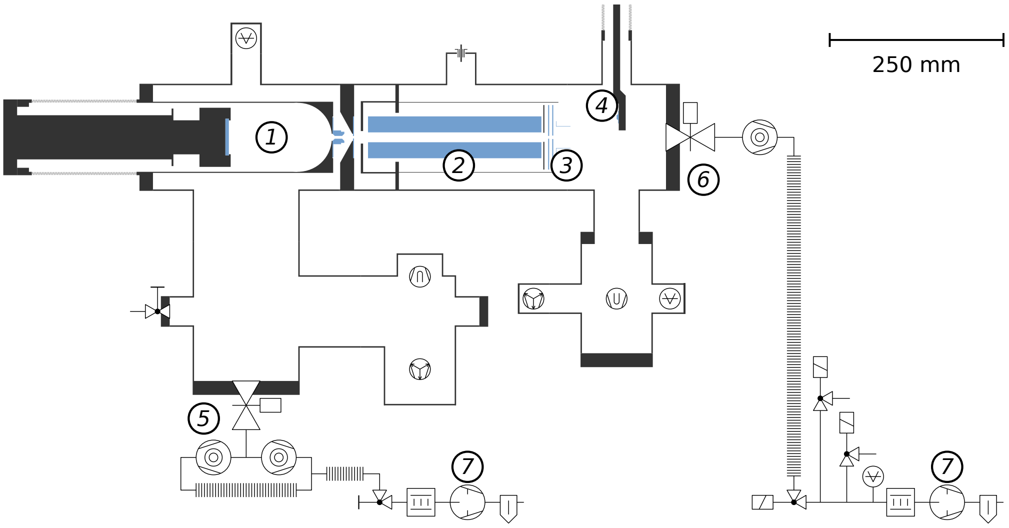

Figure 3.14: Schematic view of the *brand-new setup*:
1) magnetron sputtering source,
2) quadrupole mass filter,
3) ion collector plate, focusing lens, XY-steering plates,
4) deposition substrate on manipulator,
5) 1st turbo stage with gate valve (2× $520\,\mathrm{l{\cdot}s^{-1}}$),
6) 2nd turbo stage with gate valve ($520\,\mathrm{l{\cdot}s^{-1}}$),
7) fore-pumps. With material from [72, 76, 108].

Brand-new setup

Figure 3.14 shows the *brand-new setup*. It was introduced to alleviate the problems of the previous one (figure 3.13). The substrate's position, roughly $7\,\mathrm{cm}$ downstream of the QMF-exit 3, is the key improvement. The higher gas load during operation is getting compensated by purer gas (6N instead of 5N) and a larger turbo pump ($S_{\mathrm{N_2}} = 520\,\mathrm{l{\cdot}s^{-1}}$ instead of $S_{\mathrm{N_2}} = 250\,\mathrm{l{\cdot}s^{-1}}$). Substrates can be transported through a new connection (not shown) from the preparation chamber into the source chamber.[8] The deposition area has been equipped with it's own IGP and TSP. That is why the bypass has been removed.

The manipulator 4, which is now holding the substrate, allows movement along the vertical axis (X-axis with respect to the QMF) and rotation around the same. The substrate can thus move into and out-off the source's central axis and rotate to deposit nanoparticle under different angles.

This manipulator will be further improved by L. Knaup by the addition of a second axis of rotation. The axis is horizontal and parallel to the substrate surface. This will allow a surface-normal deposition of nanoparticles even if the sample is outside of the central beam. It will also allow the deposition under any angle from every direction, i.e. it is possible to vary the angle of elevation and the azimuth angle.

---

[8] It is possible (but untested) to connect the source to the institute's *Hydrogen* and *SPLEED* chambers in the other labs.

3.6.6 Practical considerations

A strong magnetic field is required for an efficient ionization of the argon gas. Employing a ferromagnetic sputter-target will partially shield the magnetic field and therefore sets additional requirements for the operational parameters. Typical gas flow parameters, as reported by e.g. Hartmann et al. [100], are not feasible because the reduced magnetic field demands a higher argon flux ($F_{\mathrm{Ar}} \gtrapprox 60\,\mathrm{sccm}$). These fluxes are quite sufficient to produces larger nanoparticles but are not suitable for smaller nanoparticles and clusters.

Nanoparticles agglomerate over time on all beam-facing components and can create an insulating film. This effect is the strongest for the aperture after the first pumping stage because the particle flux is highest at this point and will quickly create an insulating layer. Subsequent charge build-up creates a repulsive electric field that disrupts the particle beam. This may result in a beam degradation or even a complete (spontaneous) cut-off. It can be prevented by employing apertures that are larger in diameter than the aggregation-nozzle[9] or by a careful alignment of said apertures. Particle build-up also affects the quadrupole mass filter.

The new setup alleviates these problems. A larger nozzle ($d_{\mathrm{nozzle}} = 5\,\mathrm{mm}$) in combination with a much thinner sputter-target ($h_{\mathrm{target}} = 1\,\mathrm{mm}$) opens the way to a lower gas flux ($F_{\mathrm{Ar}} \leqq 40\,\mathrm{sccm}$). The quadrupole and the second pumping stage rest on linear guides. The quadrupole can now be removed without disassembling the second pumping stage.

3.6.7 Exemplary results

This section will present exemplary results to highlight the technical capabilities of the magnetron sputtering source and its quadrupole mass filter. The sputtering target was made of *Permenorm* ($\mathrm{Ni_{0.5}Fe_{0.5}}$) and the substrate for deposition was W(110).

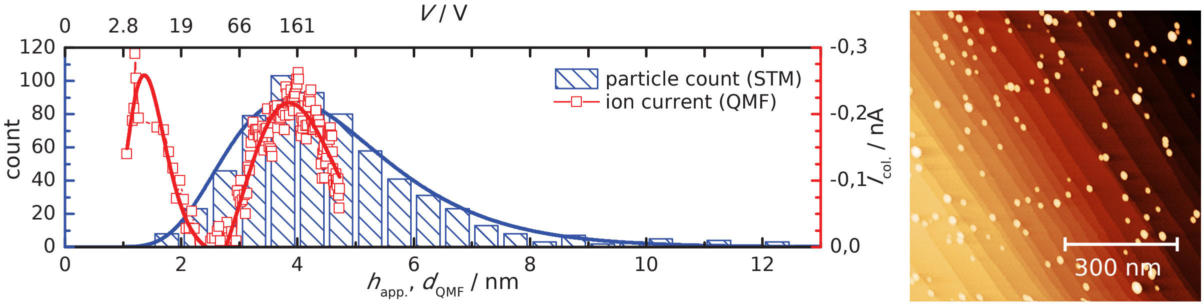

(a) Ion current from the quadrupole mass filter in comparison with the distribution of particle heights from STM (right image).

(b) After 5 minutes of deposition. W-Tip; 0.2 V; 0.8 nA

Figure 3.15: Ion spectrum from the quadrupole mass filter and apparent height of the nanoparticles after deposition. The ion spectrum was obtained before deposition and the QMF was off during deposition.

One of the first results is shown in figure 3.15(b). The magnetron was set to a sputtering current of 160 mA at gas fluxes of 80 sccm Ar and 5 sccm He. This resulted in a mag-

---

[9] Ingo Barke, personal communication, March 2016

netron power of $48\,\mathrm{W}$. The aggregation length was set to maximum. The quadrupole mass filter was set to $10\,\mathrm{kHz}$ and was used to measure the ion current spectrum. It was off during deposition to obtain unfiltered particles. The substrate was positioned in the center of the beam axis.

The ion spectrum had a bimodal distribution with two maxima (red curves in figure 3.15(a)). One at $d_{\text{QMF}} = 1.4\,\mathrm{nm}$ and one at $d_{\text{QMF}} = 4.0\,\mathrm{nm}$. The latter can be associated with the actual nanoparticles as seen in the histogram obtained from the STM. The former is an artifact from insufficient filtering. The AC voltage V of the quadrupole is below $20\,\mathrm{V}$ at this particle sizes. This voltage may be too low to remove the heaviest nanoparticles over the finite length of the QMF rods. Alternatively the DC voltage U may be lower than the minimum output value of the controller. The U/V-ratio may be lower than expected as a result. The controller also exhibits unstable output behavior when a voltage is about $10\,\mathrm{V}$ or less.

The STM data yielded a log-normal height distribution with a similar average height but a distribution that was about twice as wide. It is not entirely clear what causes the increased width. One possibility is that the conditions in the magnetron source are changing over time. A spectrum taken after deposition revealed that the number of larger particles was slightly reduced.[10] Another possibility is size-dependent charging. Larger nanoparticles have a preference to carry a positive charge. The positive charge may result in a net-zero current at certain particle sizes which effectively masks the actual particle current. Another possibility are particles that are double-charged.

Figures 3.16(a) to 3.16(c) show the height distribution of the nanoparticles after deposition. The magnetron's parameters were identical to the previous experiment but the mass filter was set to an AC-voltage of $V = 108\,\mathrm{V}$, $161\,\mathrm{V}$, and $230\,\mathrm{V}$ respectively. This corresponds to particle sizes of $d_{\text{QMF}} = 3.5\,\mathrm{nm}$, $4.0\,\mathrm{nm}$, and $4.5\,\mathrm{nm}$. The resulting spectra are a superposition of the neutral particles' broad distribution and the narrow distribution from the QMF. The number of charged particles can be estimated by comparing the peak of size-selected (and therefore charged) nanoparticles with the expected neutral background. This yields a charging ratio of approximately one third.

The magnetron source was moved to offset the substrate out of the beam of neutral particles. A deflection voltage of $10\,\mathrm{V}$ was sufficient to deflect the pre-selected 4.0-nm-particles from the QMF by $1.6°$ to the substrate. The height distribution is shown in figure 3.16(d). The major peak of the distribution is at $h_{\text{app., 1st max}} = (3.89 \pm 0.21)\,\mathrm{nm}$ and is represented by a total of 95 nanoparticles. The width of the distribution is $\Delta d/d = 10\,\%$ or $\Delta V/V = 32\,\%$. This is in good agreement with the QMF setting of $\Delta m/m = 20\,\%$ if we consider the broadening of the height as a result of the STM measurement and the data analysis (see section 3.7.2).

A second, smaller peak is at $h_{\text{app., 2nd max}} = (5.10 \pm 0.16)\,\mathrm{nm}$ and is represented by 8 particles. These nanoparticles have approximately twice the volume compared to the larger peak:

$$\begin{aligned} V_{\text{1st max}} &\propto h^3_{\text{app., 1st max}} = 58.9\,\mathrm{nm}^3 \\ V_{\text{2nd max}} &\propto h^3_{\text{app., 2nd max}} = 132.7\,\mathrm{nm}^3 \end{aligned} \tag{3.10}$$

---

[10] The shift in particle size was a result of a charge build-up on beam facing components. This problem was solved for later operations.

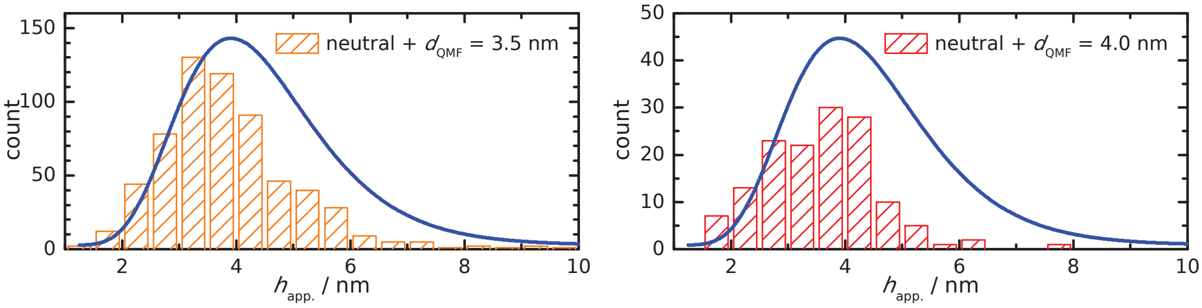

(a) Charged particles selected for $d_{QMF} = 3.5\,\mathrm{nm}$ and neutral particles of all sizes.

(b) Charged particles selected for $d_{QMF} = 4.0\,\mathrm{nm}$ and neutral particles of all sizes.

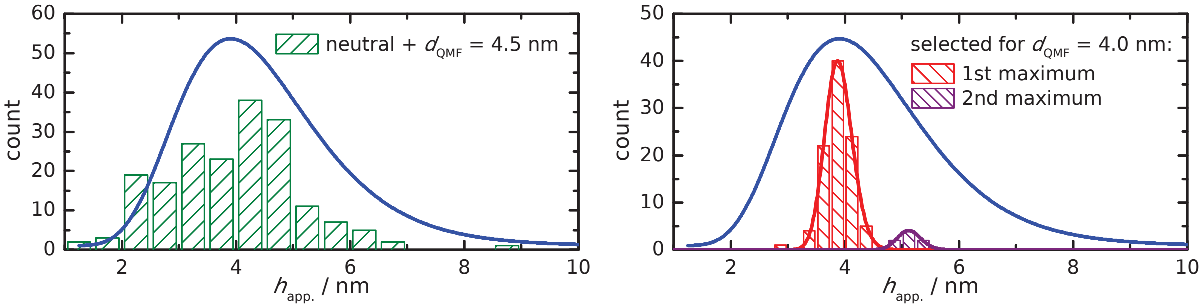

(c) Charged particles selected for $d_{QMF} = 4.5\,\mathrm{nm}$ and neutral particles of all sizes.

(d) Charged particles selected for $d_{QMF} = 4.0\,\mathrm{nm}$ and separated from the neutral beam by $1.6°$.

Figure 3.16: Apparent height of nanoparticles under different deposition conditions. The blue curve is representing the height distribution of the unfiltered particle beam from figure 3.15(a).

A nanoparticle with exactly twice the volume of the a 1st-peak-particle would have a height of

$$\begin{aligned} h_{\text{expected, 2nd max}} &= \left(2 \cdot h^3_{\text{app., 1st max}}\right)^{\frac{1}{3}} \\ &= \sqrt[3]{2} \cdot h_{\text{app., 1st max}} \\ &= 4.90\,\mathrm{nm} \end{aligned} \tag{3.11}$$

The difference between calculated and observed height is most likely due to the low number of 2nd-maximum-particles, i.e. the height is statistically not very reliable. An agglomeration of nanoparticles seems very unlikely because the surface density is less than 0.6 nanoparticles per square-micrometer at a deposition time of 15 minutes. It seems more likely that these particles carried a double charge when passing through the QMF. The relative amount of double charged particles can be calculated by comparing the amounts of single and double charged particles (95 versus 8) and by taking into consideration the log-normal distribution (see figure 3.15(a)). Approximately $11\,\%$ of the charged nanoparticles carried a double-negative charge.

Figure 3.16(d) shows no nanoparticles outside of the selected size range. This implies that the angle of $1.6°$ was sufficient to separate the charged particles from the neutral beam.

3.7 Materials and methods

The section will give an overview of the calibration and possible errors involved in the measurements. The methods of data acquisition and data analysis will be discussed. The latter includes, if applicable, the computer software. The reader is encouraged to skip forward to chapter 4.

3.7.1 STM measurement

STM imaging involves several factors that can influence image quality and scientific significance. The user's influence on the data processing (e.g. [110]) will not be discussed.

Tip form and gap voltage

An STM image is always a convolution of the surface's topography and the tip's form. A blunt tip will therefore blur surface features. If a tip has multiple ends (a *multi-tip*) then some (or all) surface features will appear once per tip-end. Such a condition can be difficult (or even impossible) to detect. Multi-tips are particularly troublesome if the surface has a high aspect-ratio, e.g. individual nanoparticles on a flat surface. A multi-tip may have no influence on a flat surface because the longest tip is always close to the surface while the secondary tips are far away. The effect of the shorter tip is particularly small considering the tunneling current's exponential dependence on the distance (see equation 3.1). Figure 3.17 shows an image taken with a multi-tip. Each of the nanoparticles appears as a group of approximately 11 elevations. The $W(110)$ far away from the nanoparticles can be mapped easily nonetheless (figure 3.17(b)).

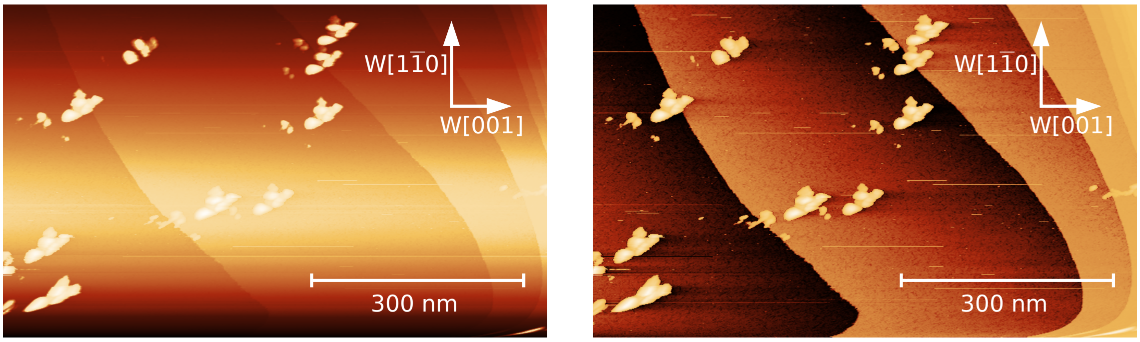

(a) Globally tilted for maximum flatness, linear color mapping. Z-drift at the lower end of the image.

(b) Z-drift was removed by aligning rows by *median of differences*. Globally tilted for maximum flatness, non-linear color mapping. Strong bending of tungsten step-edges at the lower end of the image indicates XY-drift.

Figure 3.17: STM image of eleven NiFe nanoparticles on $W(110)$, PtIr-multi-tip; $1.0\,V$; $0.8\,nA$.

Several techniques have been utilized to sharpen the STM tips and they will not be outlined here. Tip sharpening was done when images appeared blurry (blunt tip) or when features were found multiple times (multi-tip).

The gap voltage and, to a lesser extend, the tunneling current are influencing the topological imaging. This is a well known property of any STM.

Three different kinds of tips were used. Etched tungsten tips by *Omicron*, tungsten tips etched in-house, and cut PtIr tips. Self-manufactured tips were carefully cleaned and baked at > 120 °C for at least 12 h in ultra-high vacuum.

Tip material, gap voltage and tunneling current will be stated for each STM image in this thesis.

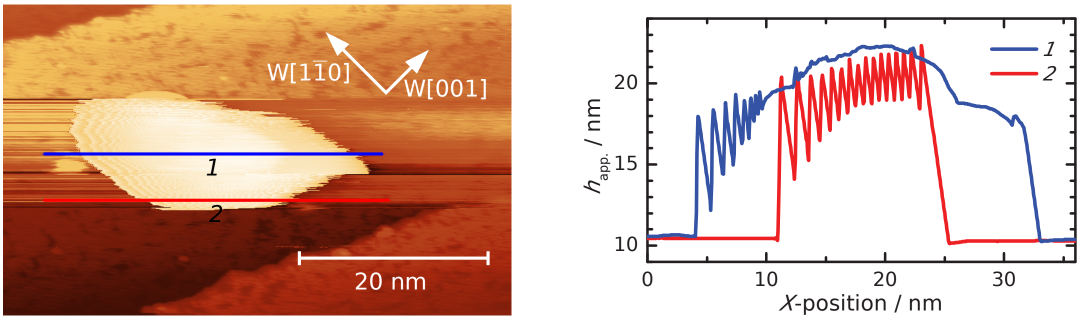

(a) STM image, adaptive non-linear color mapping; PtIr-tip; 1.0 V; 1.8 nA

(b) height profiles as designated in (a)

Figure 3.18: STM image of an annealed NiFe nanoparticle on W(110), encircled by oscillations due to adsorbates at the tip's sides (see section 4.3.1 for details).

Adsorbates at the sides of a tip can create an additional problem. This can cause intermittent tunneling when the tip is close to a steep object (e.g. a nanoparticle) and results in strong vertical oscillation of the tip (see figure 3.18).[11] This problem is generally much more prominent in PtIr tips.

Adverse effects Blunt tip: A structured surface may appear flat when the tip is wider than the surface features. A flat surface in STM is therefore not conclusive as to the actual surface flatness.

Multi-tip: A single feature (e.g. a nanoparticle) will appear once each time per tip. Twice as many nanoparticles would appear during scanning with a double tip. A height distribution from such an image would be swamped with as many artifacts as real data points.

Tip oscillations: height reading may be too high or generally unreliable.

Drift

STMs are prone to drifting as many users of STMs can confirm. That is, the tip is showing unintended movement in addition to the XY-scanning and the *constant* height may not be constant. The resulting images are distorted along one or more axes. X-drift (Y-Drift) is particularly strong after wide positional changes in X-direction (Y-direction).

The drift (and related image distortions) will disappear after some time (of scanning) at one position (see figure 3.17). Waiting thus helps. Either a scan gets restarted when

---

[11] Heinz Hövel, personal communication, March 2016

XY-drift is reasonably low or a scan gets repeated (and the first image may be discarded) or a pre-set delay time between change in position and scanning is used. It should be noted that drift in Z-direction is almost impossible to spot during scanning and is mostly visible in post-measurement evaluations (see 3.7.2).

Adverse effects XY-drift: Directions and orientations cannot be reliably identified. Y-drift: The scanned area can be to large or to small. Z-drift: Height distribution may be affected.

Noise

Mechanical vibrations and electronic noise can influence the imaging process. Due to scanning, a periodic signal (in time) will show as a periodic signal in space. Electronic noise is reduced by filters, reduction of ground-loops, and shielding of microscope and control unit. Mechanical noise is reduced by two sets of dampers. Sources of vibrations are eliminated when possible, i.e. turbo pumps and fore-pumps are off and fore-pumps in adjacent labs are put on steel springs.

Calibration

The piezos of an STM need to be calibrated to determine the relation of spatial deflection to applied voltage. This relation can be expressed as a (3×3) matrix:

$$\begin{pmatrix} XX & XY & 0 \\ YX & YY & 0 \\ 0 & 0 & ZZ \end{pmatrix} \tag{3.12}$$

The diagonal components are describing the sensitivity for each direction, i.e. the voltage required to attain a certain tip-deflection. The off-diagonal components are called crosstalk, i.e. XY is describing the movement in X-direction when a voltage at Y is applied. Cross-talk between Z and the other directions is almost always zero.

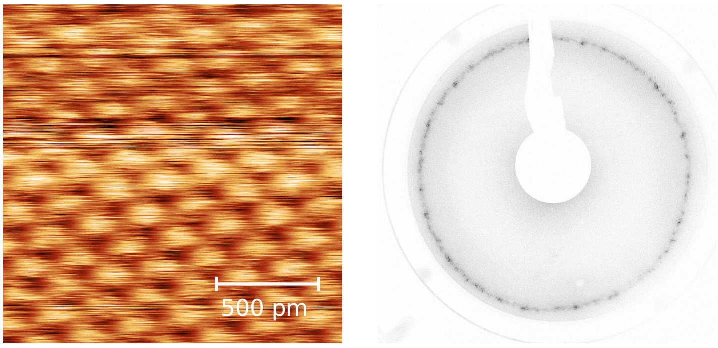

(a) STM image, PtIr-tip; 0.1 V; 1.5 nA

(b) LEED pattern, 69.8 eV

Figure 3.19: Highly oriented pyrolytic graphite (HOPG).

The sensitivity can be attained by imaging a surface with a well known structure. Atomically resolved highly oriented pyrolytic graphite (HOPG, figure 3.19(a)) is a common surface for X- and Y-calibration. This surface was prepared by exfoliation and subsequent transfer into the vacuum system. Fast scanning speed and small image size pose significant problems for calibration on HOPG. Non-negligible drift (see above) occurred throughout the imaging. HOPG substrate does not have a globally uniform orientation of its crystal axes (figure 3.19(b)). It should also be noted that the deflection of the piezo is not strictly linear and re-calibration is explicitly recommended when scanning micrometer sized areas [111].

Because of these obstacles, calibration was done on a tungsten carbide surface (see section 3.4.2 for preparation). Tungsten carbide can be observed at scanning conditions similar to those employed for nanoparticles. This calibration was therefore deemed more important but both surfaces returned the same calibration factors.

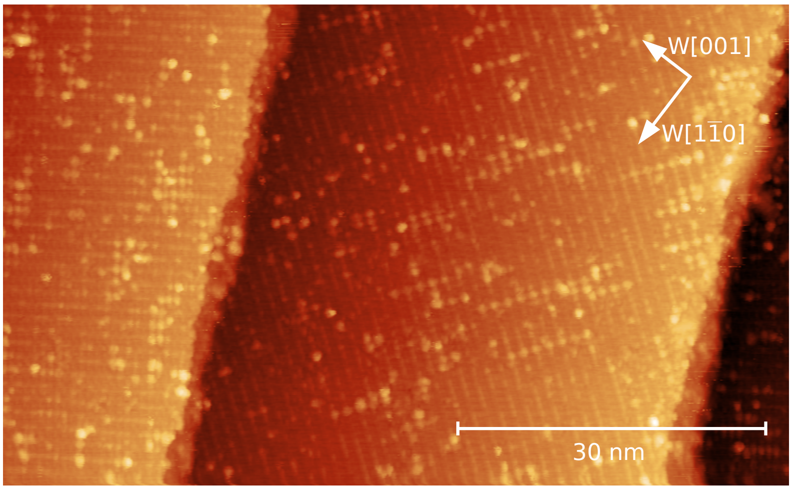

Figure 3.20: STM image of both orientational domains of tungsten carbide, PtIr-tip; 1.0 V; 0.8 nA.

The first step in the calibration was the selection of a suitable surface area. An area where, both rotational domains were visible, was selected and repeatedly scanned to reduce the drift as far as possible. Figure 3.20 shows the final image from this measurement set. Both domains were Fourier-transformed and the distance between the lines was determined by the position of their respective features in Fourier-space. The expected periodicity of $(1.30\pm0.07)\,\mathrm{nm}$ has been reported by Bode et al. [42]. Adsorbates have been found on the zigzag lines only. The well-known orientation of both domains gave additional confidence concerning the reliability of this calibration.

The Z-component was calibrated on clean W(110).[12] The step height was determined with *Gwyddion 2.45*. Multiple (i.e. less than 20) profiles were drawn across different terrace steps in fast-scan (X) direction. The *smooth bent step* fit function was used to determine the step height in each profile and the results were averaged.

The expected step height can be calculated from bulk density, atomic weight, and crystal structure:

$$V_{\square} = \frac{m_{\square}}{\rho_{\mathrm{W}}} = \frac{2\cdot m_{\mathrm{W}}}{\rho_{\mathrm{W}}} = 3.1717\cdot10^{-29}\,\mathrm{m}^3 \tag{3.13}$$

$$a_{(100)} = \sqrt[3]{V_{\square}} = 316.5\,\mathrm{pm} \tag{3.14}$$

$$a_{(110)} = \frac{1}{\sqrt{2}}\cdot a_{(100)} = 223.8\,\mathrm{pm} \tag{3.15}$$

---

[12] Images were globally tilted but not processed in any other way

with lattice constant $a_{(100)}$ and distance between neighboring (110) facets $a_{(110)}$ which is the terrace step height.

The resulting calibration has a margin of error below $3\,\%$ in drift-free conditions. This calibration has been entered into the STM acquisition software (*Scala 5.0*). Images that were taken before the calibration was done have been corrected afterwards.

Actual calibration Calibration measurements for X and Y were done on 8 April 2016 on tungsten-carbide and reference measurements on HOPG were done on 5 April 2016. Already existing images of clean tungsten have been used for Z-calibration. The resulting calibration (relative to the factory settings) is:

$$M_{\text{adj.}} = \begin{pmatrix} 0.761 & 0 & 0 \\ 0 & 0.465 & 0 \\ 0 & 0 & 0.900 \end{pmatrix} \tag{3.16}$$

This has been entered into the Scala software and new images are automatically scaled accordingly.[13] Please note that the Scala software takes the inverse values of matrix 3.16.

Coarse position

The coarse position must be taken into consideration during the evaluation of STM images. The coarse movement is (unlike the fine position) not along X, Y, and Z, but along R, Φ, and Z [111]. This means that any sidewards movement results in a slight rotation. The coarse XY-movement is limited to a circular area of $6\,\mathrm{mm}$ diameter. Sample rotation is therefore limited to $\Phi \approx \pm 6.7°$. A substrate itself may exhibit a slight rotation with respect to its holder.

The change of the coarse position allows the scanning of different substrate areas. Different areas on the sample may yield different results, which depends on the homogeneity of the sample treatment. The rotation of the sample must be taken into account when the orientation of surface structures gets analyzed. The crystal surface axes – as given in the images – are aligned without regard to this effects. Two different approaches were taken for precise angular measurement: (*1*) The axis orientation was determined by LEED. (*2*) The angle between different structures on the same images was determined with high precision.

The tungsten crystal itself is mostly, but not everywhere, in perfect conditions. Some scratches hinder imaging. Images were only taken when tungsten step edges were found. Images of nondescript surfaces were not taken into consideration and a new coarse position was chosen.

3.7.2 STM data evaluation

The typical steps to process an STM image will be outlined in this subsection. This will be explained for *Gwyddion* (version 2.35 and later). *SPIP* (version 5.1.11 by *ImageMetrology A/S*) has also been used on occasion and any special consideration regarding this software will be mentioned.

---

[13] The calibration of the STM at the time of any measurement can be checked in the parameter file (*.par*). The *scanner description* name in the parameter file should be *MICROH1_N_2017-06.SCA*. The factory calibration is called *MICROH1_N.SCA*.

First step is the *plane leveling* or *facet leveling* to compensate for the tilt of the substrate with respect to the STM. The alignment of rows by *median of differences* can be employed to reduce Z-drift or a bending in Z-direction (see figure 3.17). Re-leveling might be required. The advantages of each leveling methods are outlined in the *Gwyddion user guide* [112].

Acquisition of particle heights

The height of the nanoparticles has been determined by three different methods. The simplest method is to **draw a profile line** over a selected nanoparticle and determine the height difference between substrate and the nanoparticle's peak. The profile should be drawn in fast-scan direction and the substrate should be flat (leveled) around the nanoparticle. The profile must cross the peak of the particle, i.e. the nanoparticle's peak position must be properly selected. The average substrate elevation has to be determined based on the single profile. The method will work under difficult conditions, such as an oscillating tip (see figure 3.18) but it requires several estimates on the side of the user. The manual selection of measurement points is making this method slow and unreliable.

A faster approach is to manually **draw a mask** around each nanoparticle in a picture. The difference between maximum and minimum elevation inside a mask relates to the height of the nanoparticle. This method depends on a low-noise surface which is locally flat around each nanoparticle. A local slope will increase the calculated height and must be avoided. The effect of noise can be calculated by drawing masks of similar size at empty surface areas. The difference between maximum and minimum elevation will yield the error bars of this method. This method requires a medium amount of work from the user and is not overly sensitive to (possibly wrong) estimates.

The fastest method to process nanoparticles is Gwyddion's **automated *Grain Analysis*** method called *Mark by Otsu's*. This method will split the height data of an entire image in two classes. Areas of high data are assumed to be particles [112]. This method works very well on flat surfaces but it will fail on surfaces of high curvature. Exhaustive flattening, typically low-order polynomial background subtraction, is necessary. This method will return several parameters of the detected grains. The height can be calculated by subtracting the average surface elevation from each nanoparticle's maximum height. The surface must be as flat as possible. This can be achieved by excluding the nanoparticles from the further flattening process[14] and then applying high-order polynomial background subtraction. The substrate's root mean square elevation yields the error bars of this method. Nanoparticles which are close together will be recognized as a single grain. Manual splitting of grains is the standard solution and not overly time-consuming.

The last two methods can be combined: *Mark by Otsu's* is used to draw a (small) mask around each nanoparticle. Every mask is then expanded by a few pixels to include its surrounding surface. The maximum height difference inside a mask yields the height of the respective nanoparticle. This method utilizes the fast particle recognition of *Mark by Otsu's* but it does not require extensive background subtraction.

---

[14] Excluding nanoparticles is simple because they have been highlighted.

Acquisition of island size and equivalent spherical diameter

The analysis of a single monolayer high islands requires several steps:

First the surface area A of a given island is determined by means of *thresholding*, also known as *flooding*. That is, any area in the image which exceeds a certain height is highlighted.

The size of this area is converted into a number of atoms: The surface density can be estimated based on pseudomorphic growth on the $\mathrm{W}(110)$ surface. That means that the number of atoms per area N_{atom} in the island is equal to the number of surface atoms of $\mathrm{W}(110)$:

$$N_{\text{atom}} = N_{\text{W(110)}} = 14.1\,\text{atoms·nm}^{-2} \tag{3.17}$$

This is just a rough estimate because the growth mode of an island – especially at a varying coverage – is not always known. Fe, Ni, and Co atoms are smaller than W atoms and thus the surface density of these atoms will be higher than or equal to that of $\mathrm{W}(110)$. (See also section 2.4.1). The total number of atoms in a given island is

$$n_{\text{atom}} = A \cdot N_{\text{atom}}. \tag{3.18}$$

The number of atoms needs to be converted into an equivalent volume. This is based on the bulk density ρ of the corresponding material. The total volume of the island is

$$\begin{aligned} V &= n_{\text{atom}} \cdot V_{\text{single atom}} \\ &= n_{\text{atom}} \cdot \frac{M}{\rho} \end{aligned} \tag{3.19}$$

with the atomic weight M. The weighted average is used in case of an alloy.

The volume can be converted into the diameter $d_{\text{equiv.}}$ of a sphere:

$$\begin{aligned} V &= \frac{4\pi}{3} \cdot r^3 \\ \Leftrightarrow d_{\text{equiv.}} &= \sqrt[3]{\frac{6}{\pi} \cdot V} \end{aligned} \tag{3.20}$$

Some islands were accompanied by a nanoparticle. The volume of the nanoparticle was estimated based on its apparent height and the equivalent diameter was calculated from the combined volume of island and nanoparticle.

3.7.3 LEED

A LEED system does not require an overly complicated calibration but some consideration is required nonetheless. The parameters were taken from the calibration sheet for the given instrument and the system was operated as outlined in the manual [73]. Voltages for the lenses were adjusted until sharp spots were achieved. The energy of the incident electron beam is stated for every LEED image that was taken and the beam was focused on the center of the substrate unless stated otherwise. Every substrates was grounded to avoid charging. The *SpectaLEED* is a rear-view LEED, i.e. the electron gun is blocking the view on the central spot in most images.

The patterns were recorded with a hand-held digital camera. *ImageJ* was used to crop the images and adjust the brightness. The images were also converted to gray scale and inverted. No correction was made for the spherical projection of the LEED screen. Blurry images are mostly a result of camera shake or improper focusing. It will be stated if blurriness was not a result of image capturing.

3.7.4 Sample heating and temperature measurement

The temperature has significant influence on the dynamic behavior of a sample. It is therefore necessary to get precise temperature readings and to know the properties of the heating systems. This section gives an overview of the different types of thermometers and introduces the different heaters.

Thermocouples

A thermocouple operates on the Seebeck effect and requires a physical contact at its point of measurement. Both of the main manipulators are equipped with two thermocouples of Type K. The points of measurement are adjacent to the sample where the distance between substrate and thermocouple causes a difference between actual temperature and read-out. The response time can be in the order of several minutes as shown in figure 3.21.

Radiation thermometers

Radiation thermometers, also called pyrometers, offer an optical (i.e. non-contact) way to measure temperatures. A black-body of non-zero temperature emits (infrared) light and the spectral density is described by Planck's law. The optical properties of real-life objects are not those of a black-body. These are called gray-bodies and the difference in emission between gray- and black-body is expressed as the *emissivity* $\varepsilon(\lambda, T)$. Knowledge of the emissivity is necessary to calculate the actual temperature based on the spectral emission. [113, 114]

Two pyrometers have been used. The *Ircon Ultimax Plus UX 20P* is a narrow band radiation thermometer, i.e. it determines the temperature by measuring the emission at a single, fixed wavelength. The wavelength of measurement is $\lambda = 0.96\,\mu\mathrm{m}$ and this results in a temperature range of 600 to $3000\,^{\circ}\mathrm{C}$. The standard use-case is the electron bombardment heating (*flashing*) and oxygen annealing of tungsten substrates. High temperature annealing of nanoparticles at $T \approx 1000\,\mathrm{K}$ is another application.

The *Raytek MI3 2M* operates at $\lambda = 1.6\,\mu\mathrm{m}$ which puts it at a temperature range of 250 to $1400\,^{\circ}\mathrm{C}$. It's main use-case is the annealing of substrates.

A number of experiments have been done to determine the precise emissivity of various metals. This depends not just on the composition of the material but on the temperature, the angle of emission and on surface corrugation [115]. Pending further development in this field, the emissivity is set to $\varepsilon = 0.3$ for measurements on polished tungsten crystals. Measurements are done at normal emission when possible (e.g. on the manipulators). The angle for electron bombardment heating is roughly 55° from the surface normal vector.

Sample annealing on the manipulators' integrated heaters

Samples were usually annealed on the integrated heater of the manipulator in the analysis or preparation chamber (see section 3.1). The electric current to reach the desired temperature was selected from a calibration sheet (see table A.2) and previous measurements were taken in consideration. A laboratory power supply was set to the desired current with a precision of 0.01 A (least significant digit). The current was adjusted during annealing when necessary.

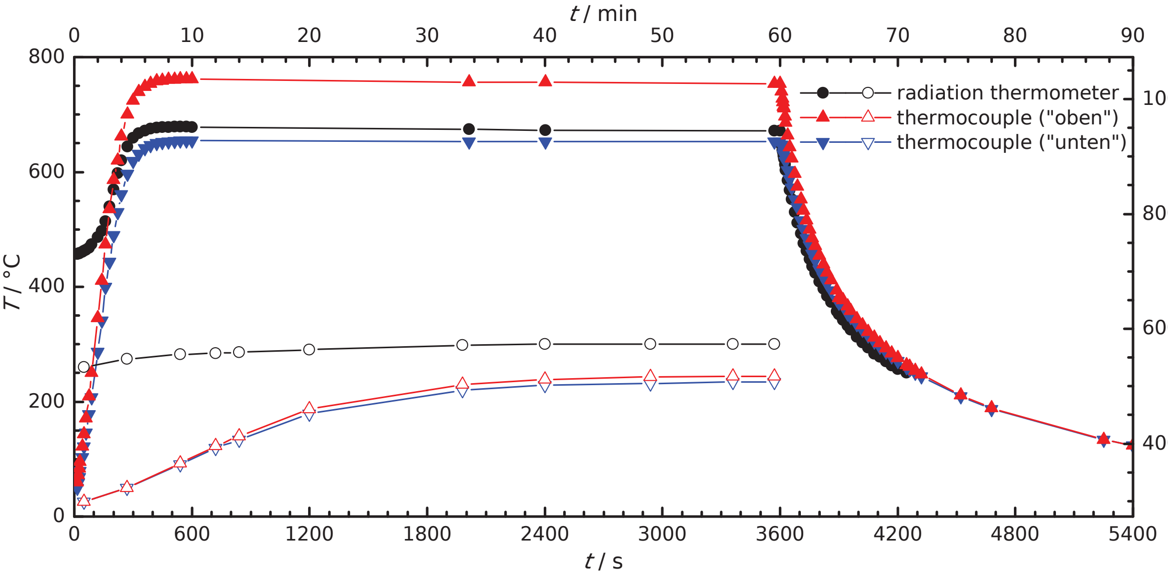

Figure 3.21: Temperature curves for the sample heater in the analysis chamber. Open symbols: 0.85 A / 3.4 W. Closed symbols: 2.4 A / 45 W. Annealing duration: 1 hour.

The **annealing duration** as given in chapter 4 is the time between activation and deactivation of the power supply. Figure 3.21 shows the typical response time for two different currents. The **annealing temperature** is the highest observed temperature while the power supply was on.

3.7.5 Tungsten substrates and their cleaning

Two different tungsten single crystals were used. Both have a (110) surface with different in-plane orientations. The larger one, edge length approximately 6 mm, has the [001] in horizontal direction, i.e. parallel to the STM's X-axis. The smaller one ($\approx 5\,\mathrm{mm}$) has its [001] direction pointing to the upper left corner at 45°. The laboratory diary and other records refer to the smaller one as *Düsseldorfer* and the larger one as *Dortmunder*.

Carbon has been thoroughly removed from the larger one's bulk by annealing in oxygen atmosphere for one week, courtesy of W. Rosellen. Further oxygen annealing is therefore rarely required. 50 flashing cycles at up to 2000 K were done during testing without changes of the LEED pattern. Oxygen annealing is carried out more often than that and it is safe to assume a carbon-free surface. Such thorough cleaning has not been carried out on the smaller one and oxygen annealing is therefore regularly required. Repeated annealing results in the W(110)/C-R(15×3) pattern as outlined in section 3.4.

The larger one was used regularly for this thesis and annealed when deemed appropriate. The smaller one was used on occasion and has been oxygen annealed regularly. Oxygen annealing was carried out before each deposition of $Ni_{0.5}Fe_{0.5}$ nanoparticles when subsequent tempering had been planed. See section 4.3.1 for these measurements.

3.7.6 Software

Data analysis was done with two different software solutions. *LibreOffice Calc* was used to accumulate data (e.g. nanoparticle height) and to perform simple calculations. *OriginPro 9.0G* was used for graph plotting, data fitting, and statistical analyses.

4 Results and discussion

This chapter covers the detailed results of my measurements. It includes the preparation of the substrates, the deposition and annealing of cobalt nanoparticles on these substrates, and the deposition and annealing of nickel-iron nanoparticles on W(110). Nickel-cobalt nanoparticles will be touched as well.

The section for each measurement also includes a short paragraph about the preparation steps and will conclude with a discussion of the results.

A brief overview of all results and a short discussion will be given in section 4.5.

4.1 Tungsten related surfaces

This section will introduce the preparation of the tungsten related surfaces for the later deposition of nanoparticles.

4.1.1 Carbon on W(110)

Sample preparation

The W(110) substrate with the higher carbon content (*Düsseldorfer*) was repeatedly annealed at 2000 K as outlined in section 3.7.5.

Results

The W(110)/C-R(15×3) reconstruction formed as a result of the annealing. LEED pattern and STM image are in perfect agreement (figure 4.1). The particular LEED image was selected because one of the rotational domains is better visible than the other. This is a typical case when the electron beam is close to the edge of the substrate (e.g. [36]). The STM image was selected because both rotational domains are visible on adjacent terraces.

This is in perfect agreement with the results of Bode et al. [42] as outlined in section 2.3.2.

4.1.2 Oxygen on W(110) at room temperature

The distinct pattern of the p(2×1) is well suited to find oxygen contamination (i.e. air) in the vacuum system. Accidental production of p(1×1) is unlikely due to the large amount of oxygen required. This is of particular significance during deposition of nanoparticles. The connecting tubes between the main chambers and the nanoparticle sources have to be removed to allow vibration-free STM. These connections do not feature pressure gauges but they are vented, re-sealed, and baked before every deposition by different (and sometimes inexperienced) operators. Figure 4.2 shows LEED

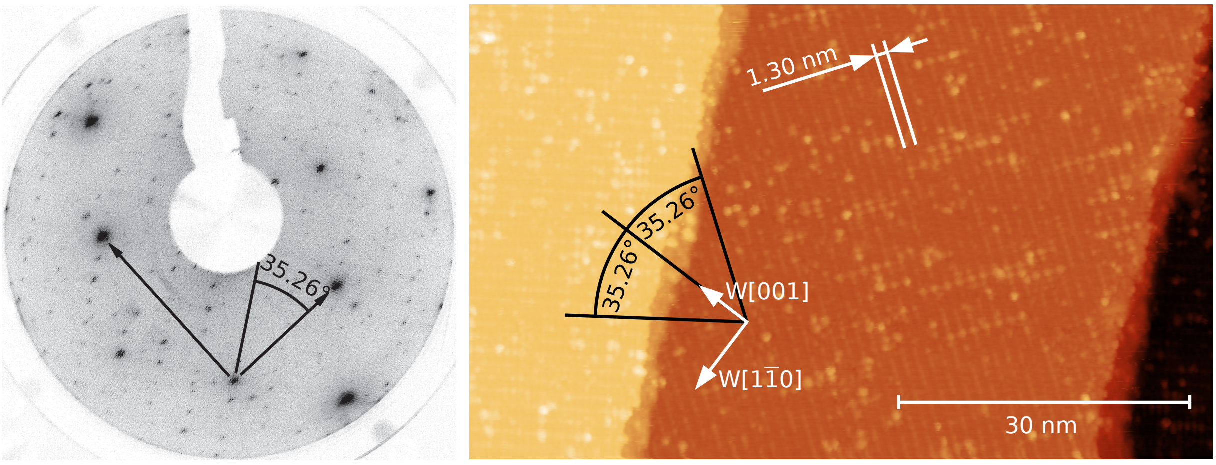

(a) LEED image (134 eV)

(b) STM image: The rotational domain on the left terrace corresponds with the diffraction pattern of the LEED image. PtIr-Tip; 1.0 V; 0.8 nA

Figure 4.1: C-R(15×3) reconstruction on W(110) after repeated annealing.

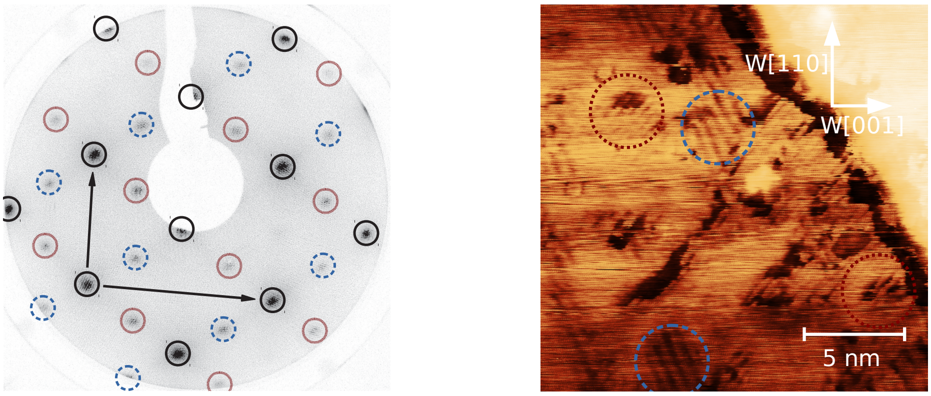

(a) LEED image (112 eV)

(b) STM image: W-Tip; 1.0 V; 0.8 nA

Figure 4.2: Oxygen structure on W(110) after exposure to low amounts of oxygen. Left: After co-deposition of Co nanoparticles and air. O-p(2×1) has formed after 18 minutes of exposure. Nanoparticles are not visible in LEED. Right: after 40 minutes of operation while the particle beam itself was blocked. Rotational domains are highlighted.

and STM images with a known leak in the connection between the magnetron sputtering source and the preparation chamber. A very rough estimate puts the exposure to ambient air at 8 L and 18 L.

The high gas load during particle deposition will mask a possible leak. An observant operator will nevertheless observe the increased base pressure upon completion. The reconstruction and its preparation are in agreement with previous publications (see section 2.3.3).

STM of p(2×1) reveals a highly irregular surface without long-ranged orientation(s). This makes it difficult to interpret data from the deposition and annealing of nanoparticles.

4.1.3 Oxygen on W(110) at elevated temperatures

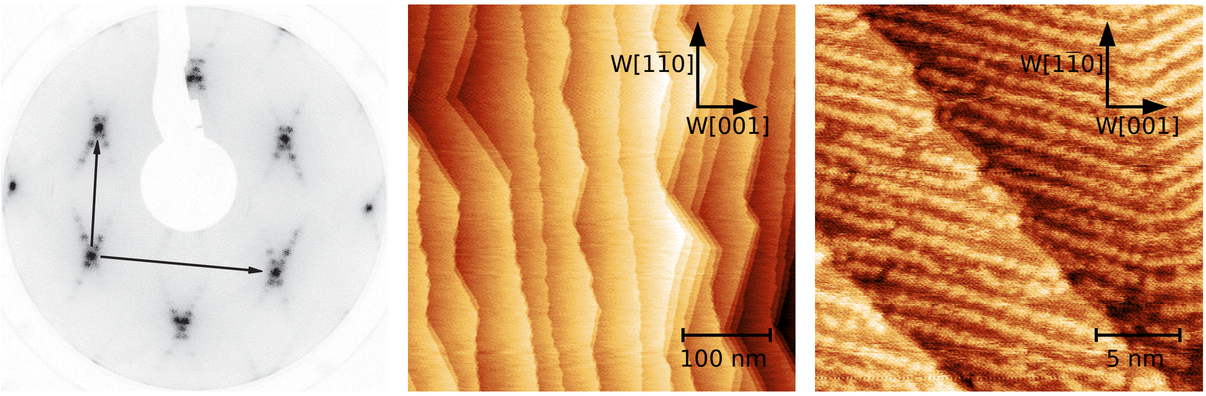

(a) LEED image: Tungsten structure with satellite spots of oxygen (126 eV)

(b) STM image: Highly ordered step edges of tungsten oxide. PtIr-Tip; 1.0 V; 0.8 nA

(c) STM image: Both rotational domains of oxidation lines. PtIr-Tip; 1.0 V; 0.8 nA

Figure 4.3: W(110) after 20 minutes of annealing at 1500 K and $1.1 \cdot 10^{-7}$ mbar oxygen pressure.

Figure 4.3 shows the LEED and STM image that were obtained after annealing at 1500 K in oxygen atmosphere ($p_{O_2} = 1.1 \cdot 10^{-7}$ mbar, 100 L). The orientation of the satellite spots in LEED (figure 4.3(a)) is in agreement with the oxidation lines in real space (figure 4.3(c)). These lines are oriented at an angle of ≈±23° with respect to W[001]. This is in good agreement with the (1×1)×12 reconstruction which has an expected value of ±25.24°, i.e. orientation along $W\langle 1\bar{1}3\rangle$ (see section 2.3.3). The surface exhibits a better ordering than clean W(110) with long straight terrace steps. The observed line distance is (1.45 ± 0.07) nm which is similar to STM observation by Johnson et al. (≈20 Å) [47]. It should be noted though that they did observe reconstruction along the $W\langle 1\bar{1}2\rangle$ axes.

The (1×1)×12 along $W\langle 1\bar{1}3\rangle$ is the only high temperature reconstruction of tungsten oxide that could be observed during this thesis' work.

4.2 Cobalt nanoparticles

This section covers the production of cobalt nanoparticles in the magnetron sputtering source, their deposition on different substrates, and their annealing.

4.2.1 Cobalt nanoparticles on W(110)

Previous publication The measurements for this subsection were part of J. Schubert's bachelor's thesis [116]. I have analyzed the resulting data independently and without his help.

Composition of raw material The nanoparticles were produced in the magnetron sputtering source. The sputtering target from *Hauner* was made of Co with a purity of $99.99\,\%$.

Sample preparation

The $\mathrm{W}(110)$ surface was cleaned by flashing before the deposition of nanoparticles. The detailed procedure can be found in section 3.4.1.

The nanoparticles were produced in the magnetron sputtering source. Two depositions were made at different positions of the substrate. The quadrupole mass filter was adjusted to different particle masses for both depositions. One deposition, on the left side of the substrate, was set to a mass of $m_{\mathrm{QMF}} \approx 6.51{\cdot}10^5\,\mathrm{amu}$ and a filtering width of $10\,\%$. This is equivalent to a mean particle diameter of approximately $6.08\,\mathrm{nm}$. The other deposition was set to $m_{\mathrm{QMF}} \approx 1.08{\cdot}10^6\,\mathrm{amu} \mathrel{\hat{=}} d_{\mathrm{QMF}} = 7.19\,\mathrm{nm}$. The deflection voltage of the steering plates was set accordingly.

The samples were analyzed by STM after deposition and subsequently annealed for 15 minutes at a pre-selected heating current. Comparative STM measurements were done when the samples were back to room temperature. Some samples were annealed several times and they were scanned each time after cool-down. The nanoparticles were annealed at temperatures ranging from 533 to $927\,\mathrm{K}$.

Results

Annealing at the lowest temperature ($T = 533\,\mathrm{K}$) was sufficient to start the melting process. This sample was then annealed a second time at identical conditions to further the melting process. This resulted in particles as shown in figure 4.4(a). The melting process resulted in an unrolling carpet. The height distributions of the particles after deposition and after both annealing steps are shown in figure 4.5. The initial heights are smaller than the diameters that were derived from the mass filter's parameters. This can be attributed to two factors: The calculation of a particle's diameter from its mass is based on the assumptions of bulk density and a spherical form. Both assumptions are just loose approximations. Flattening upon landing can cause a deviation from the spherical form (see section 2.5).

The distributions are characterized by a shift towards smaller heights. The shifting occurs for all observed particle heights. The loss of height increases approximately linear with annealing time. No material is lost to evaporation as atoms diffuse from the nanoparticles' surface to the surrounding diffusion zone. The relatively small diffusion zone indicates that the annealing temperature was just barely higher than the temperature required for surface melting.

The diffusion zone *1* and the adjacent nanoparticle were analyzed in more detail. The particle had a height of $h_{\mathrm{app.}} = 5.6\,\mathrm{nm}$ and the diffusion zone contained enough material

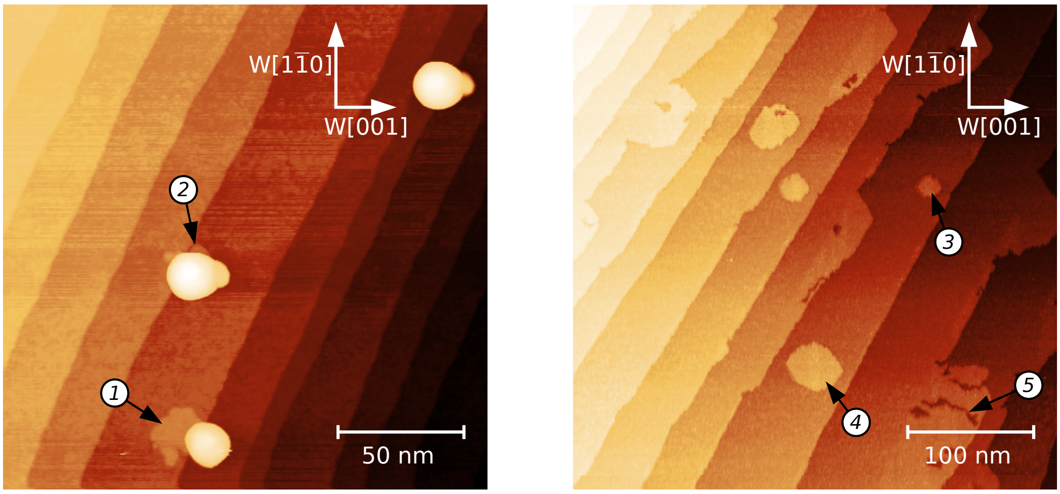

(a) After two annealing steps at 533 K: The lower nanoparticles (*1*, *2*) show unrolling carpet behavior.

(b) After annealing at 593 K: Monolayer islands but no nanoparticles are remaining. Island *3* contains material equivalent to a 4.1 nm sphere. Island *4* contains material equivalent to a 7.0 nm sphere. Vacancy island *5*.

Figure 4.4: STM images of Co nanoparticles on W(110). Pre-selected particle diameter was $d_{\text{QMF}} = 6.08\,\text{nm}$. W-Tip; 1.0 V; 0.8 nA

for a spherical, bulk-like particle with a diameter of $d_{\text{equiv.}} \approx 4.1\,\text{nm}$. The combination of these two would yield a nanoparticle with $d_{\text{equiv.}} \approx 6.2\,\text{nm}$. Therefore, the diffusion zone could stem from the adjacent particle or it could be a remainder of another nanoparticle. The bimodal height distribution for this sample is shown in figure 4.5(a) and can support both theories. The melting of one particle seems more likely because the diffusion zone at other nanoparticles (e.g. *2*, $d_{\text{equiv.}} \approx 2.1\,\text{nm}$) is significantly smaller.

Figure 4.4(b) shows the result of 15 minutes of annealing at up to 593 K. This temperature was sufficient for the nanoparticles to melt completely. One monolayer high islands were remaining. Similar results were found for all higher annealing temperatures. An increase in temperature lead to an increased diffusion. The islands were therefore further spread across the surface and started to agglomerate at the substrate's step edges.

The annealing at 593 K also created vacancy islands (see *5* in figure 4.4(b)). One should expect that islands are merging upon contact (see section 2.4). A possible explanation may be that these islands have different crystallographic orientations, which is only possible if the island growth is non-pseudomorphic. Strain-induced dislocations which make it energetically unfavorable to fill these gaps are another possibility. The wedge-shaped islands downstairs of the terrace steps were another characteristic. These had one edge which was almost parallel to the step edge and one which met the step edge at a steep angle.

The surface area of the islands was examined: Island *3* (figure 4.4(b), diameter according to QMF: $d_{\text{QMF}} = 6.08\,\text{nm}$) contains enough material to create a spherical, bulk-like nanoparticle with diameter $d_{\text{equiv.}} \approx 4.1\,\text{nm}$. If we consider that some material had agglomerated at nearby step edges, then we can assume that this islands is the remainder

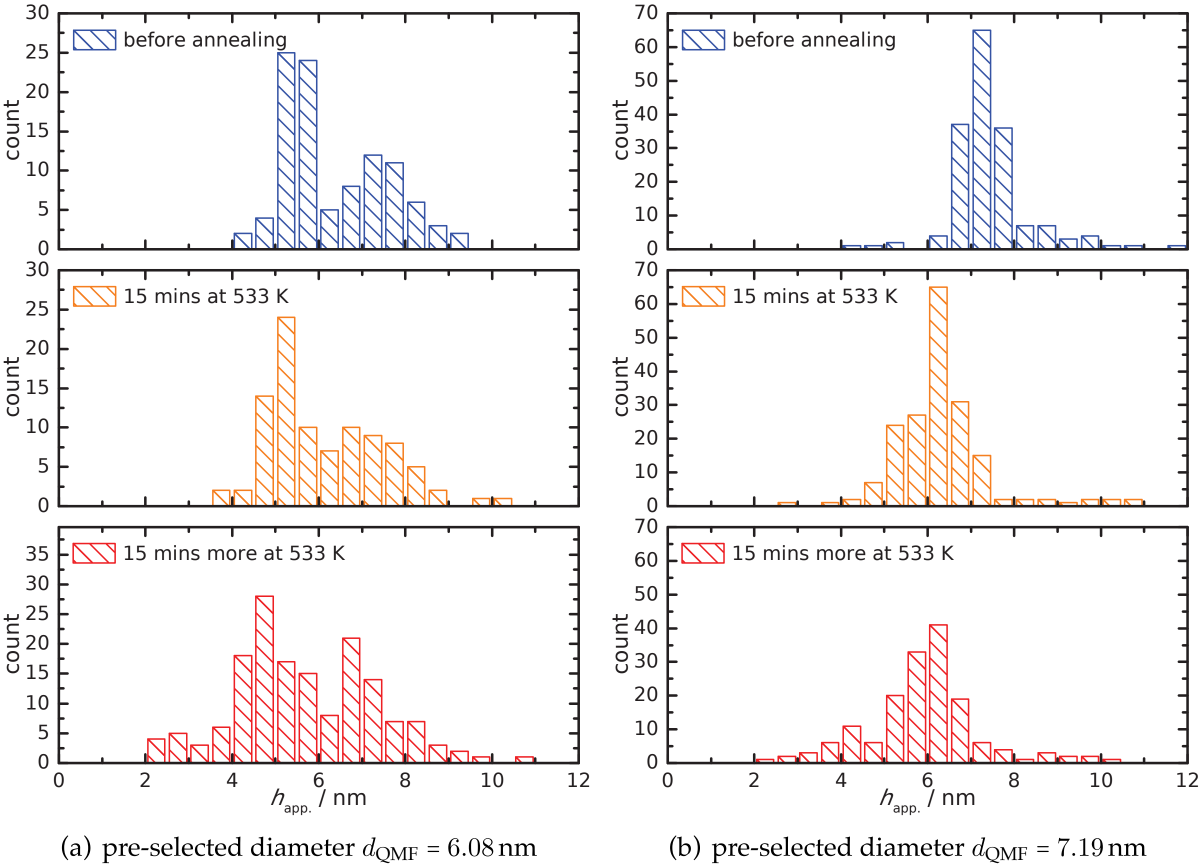

(a) pre-selected diameter $d_{\mathrm{QMF}} = 6.08\,\mathrm{nm}$ (b) pre-selected diameter $d_{\mathrm{QMF}} = 7.19\,\mathrm{nm}$

Figure 4.5: Distribution of apparent height for Co nanoparticles on W(110) based on STM measurements. Heights were recorded after deposition and after two annealing steps at $533\,\mathrm{K}$. The wide, bimodal form of the height distribution is a result of the insufficient separation between size-selected and neutral particles (see also section 3.6).

of a nanoparticle. Island 4 had a five times larger surface area. The corresponding diameter would be $d_{\mathrm{equiv.}} \approx 7.0\,\mathrm{nm}$. Given these results one can assume that each island represents the remainder of one nanoparticle.

In general, island edges were oriented along the $\mathrm{W}\langle 111\rangle$ axes. Annealing temperatures of up to $783\,\mathrm{K}$ (figure 4.6(a)) lead to sharper island corners and the edges' orientation became more pronounced. The wedges were elongated perpendicular to the terrace steps. This indicates a transition towards step meandering (e.g. [117, sec. 4.7.2]) and it indicates a significantly increased surface mobility of the Co atoms.

The highest temperature ($927\,\mathrm{K}$, see figure 4.6(b)) caused a complete melting of all nanoparticles. Most Co atoms were attached in an even line at the terrace steps. The widest terraces ($100\,\mathrm{nm}$ and wider) featured large monolayer island. These islands showed a preferred orientation along the terrace step edges, which is an indicator of morphological anisotropy.

There was no indication of an anisotropic melting as it has been reported by Rosellen for nanoparticles with an average height of $9.5\,\mathrm{nm}$ [67, sec. 4.6.2]. The nanoparticles in this work have a very wide size distribution up to a height of $h_{\mathrm{app.}} \approx 12\,\mathrm{nm}$ (see figure 4.5). This means that the differences of the melting processes cannot be explained by a difference in height.

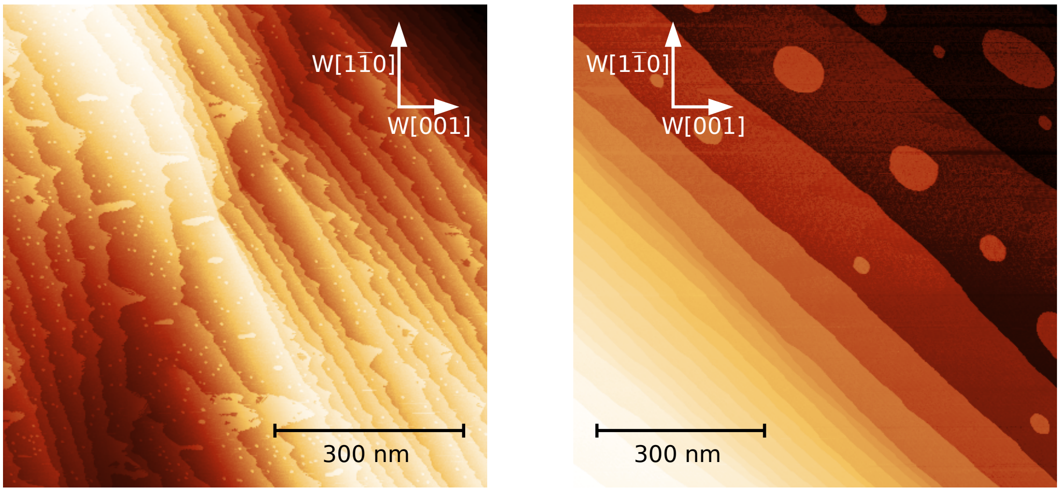

(a) After annealing for 15 minutes to 783 K. Meandering shapes and islands are elongated.

(b) After annealing for 15 minutes to 927 K. Co atoms have agglomerated downstairs of the terrace steps. Large elliptic islands have formed on the largest terraces.

Figure 4.6: STM images of Co nanoparticles on W(110) after high-temperature annealing. The remaining Co structures are one monolayer high and are indicative of a high surface mobility. Pre-selected particle diameter $d_{\mathrm{QMF}} = 7.19\,\mathrm{nm}$. W-Tip; 1.0 V; 0.8 nA

4.2.2 Cobalt nanoparticles on W(110)/C-R(15×3)

Composition of raw material The nanoparticles were produced in the magnetron sputtering source. The sputtering target from *Hauner* was made of Co with a purity of $99.99\,\%$.

Sample preparation

The tungsten carbide surface was prepared by repeated annealing of a W(110) crystal. This caused the agglomeration of carbon at the surface and resulted in the formation of the C-R$(15{\times}3)$ reconstruction (see also section 2.3.2).

The nanoparticles from the magnetron sputtering source were selected to a mass of $m_{\mathrm{QMF}} \approx 1.08{\cdot}10^6\,\mathrm{amu}$ which corresponds to a particle diameter of $d_{\mathrm{QMF}} \approx 7.19\,\mathrm{nm}$. The steering plates were used to deflect the charged particles towards the substrate. This setup is identical to the setup for the larger particles in section 4.2.1 .

Two samples were prepared. One was repeatedly annealed at increasing temperatures and was examined at room temperature after each annealing step. Each annealing step lasted 15 minutes and the temperature was increased in the following steps: $518\,\mathrm{K}$[1], $533\,\mathrm{K}$, $544\,\mathrm{K}$, and $556\,\mathrm{K}$. A final annealing step of $573\,\mathrm{K}$ lasted 60 minutes.

The other sample was annealed once for 15 minutes to $550\,\mathrm{K}$. This sample was examined in more detail to obtain a height distribution with high statistical significance.

---

[1] This temperature has been estimated based on the heater's typical response.

Results of the 1st sample: temperature dependence

The nanoparticles on tungsten carbide had an initial height distribution similar to the distribution that was observed on W(110) (see section 4.2.1). This indicates, that the change in substrate did not affect the particles itself at deposition. No significant change in height or form of the nanoparticles was observed at $544\,\text{K}$ and below. Typical results of the first sample, annealed at $556\,\text{K}$, are shown in figure 4.7(a). Unrolling carpet could be observed for some of the nanoparticles but others were still intact. The area of selected diffusion zones was analyzed. The combined volume of the diffusion zone *1* and its adjacent nanoparticle would yield a sphere of $d_{\text{equiv.}} \approx 6.3\,\text{nm}$. *2* would yield $d_{\text{equiv.}} \approx 7.9\,\text{nm}$. Both of these values are well within the initial size range. This suggests that each diffusion zone stemmed from the adjacent nanoparticle only.

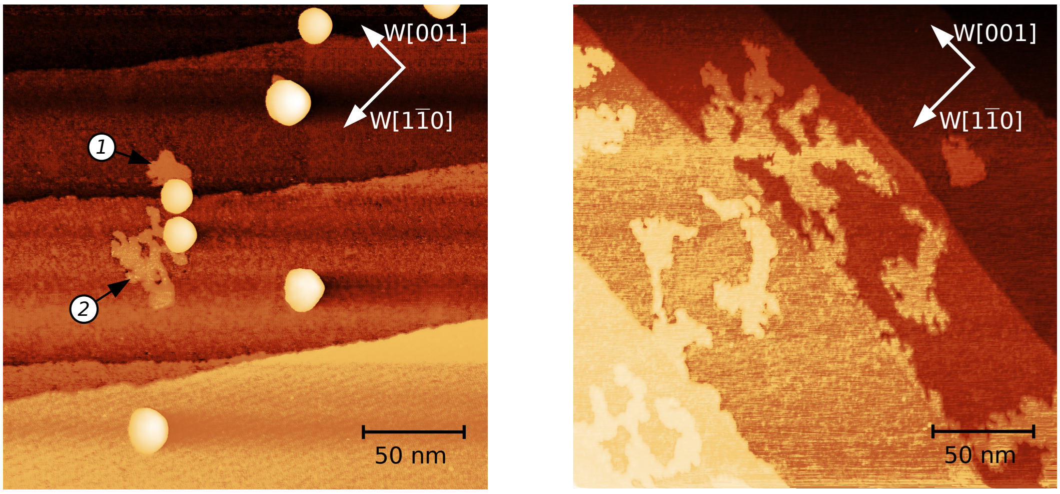

(a) After annealing for 15 minutes at up to $556\,\text{K}$. Some nanoparticles have a reduced height as a result of unrolling carpet.

(b) After annealing for 60 minutes at up to $573\,\text{K}$. Some nanoparticles are completely transformed to islands. Other nanoparticles (not shown) are still intact.

Figure 4.7: STM images of Co nanoparticles on W(110)/C-R(15×3) after annealing. W-Tip; $1.0\,\text{V}$; $0.8\,\text{nA}$

The melting continued at the next higher annealing step. Some nanoparticles turned into ramified islands (figure 4.7(b)) but other nanoparticles were still intact (not shown). The ramified shape makes it difficult to ascertain where the material came from, i.e. at what position the original nanoparticle was.

Results of the 2nd sample: site dependence at 550 K

The second sample was annealed and subsequently examined in more detail. The height distribution, that was taken before the annealing, was obtained at the sample's center (figure 4.8(a), blue). It is known from previous measurements that the area of examination does not affect the results as long as that area was exposed to the beam of nanoparticle. The height distribution that was taken before annealing is therefore representative of the overall ensemble. Figure 4.8(b) shows the different positions on the substrate. Position *A* was slightly above the center and was virtually identical to

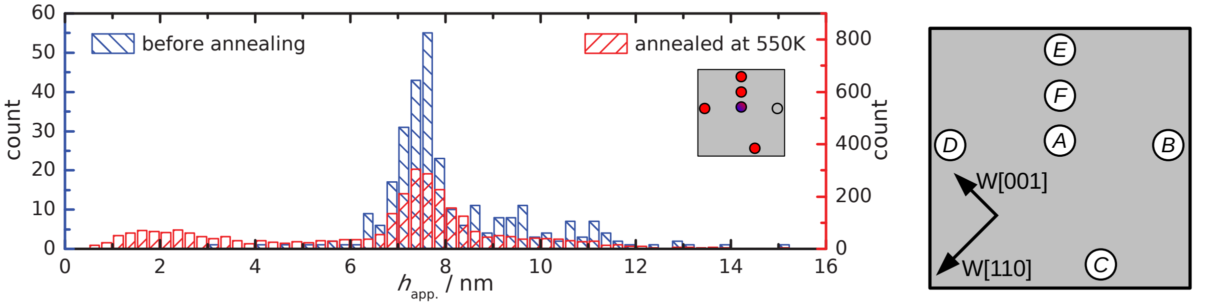

(a) Ordinates are scaled in accordance with examined surface area.

(b) Map of the substrate.

Figure 4.8: Second sample of Co nanoparticles on tungsten carbide. Height distribution after deposition (position *A*) and cumulative height distribution after annealing at 550 K (positions *A* and *C*–*F*).

the position which was examined before the annealing. Position *B*, at the right edge of the sample, contained less than 5 nanoparticles per square-micrometer. This position was obviously on the edge of the particle's beam and will not be discussed any further. Position *C* was at the bottom edge of the substrate a third to the right. Position *D* was at the substrate's left edge. Position *E* was at the substrate's upper edge and position *F* was midway between positions *A* and *E*.

An annealing temperature of 550 K was chosen because it was just below the temperature at which melting had started on the first sample. The number of intact nanoparticles varied significantly. Less than half of the nanoparticles in area *F* (figure 4.13(b)) were intact and the remainders showed unrolling carpet behavior or had been reduced to a monolayer island. Area *E* exhibited a similar degree of progression (figure 4.12(b)). Almost all nanoparticles were intact in areas *C* (figure 4.10) and *D* (figure 4.11) where just a few percent showed signs of (complete) melting. Area *A* (figure 4.9(b)) resembled the average distribution.

The height distribution after annealing (figure 4.8(a), red) shows that many nanoparticles had retained their original height but some had shrunk. The number of intact nanoparticles was diminished but there was no general movement towards smaller sizes as it was observed for Co on W(110). This effect was most pronounced at position *F* (figure 4.13). Some particles were melting earlier than others. This is in strong

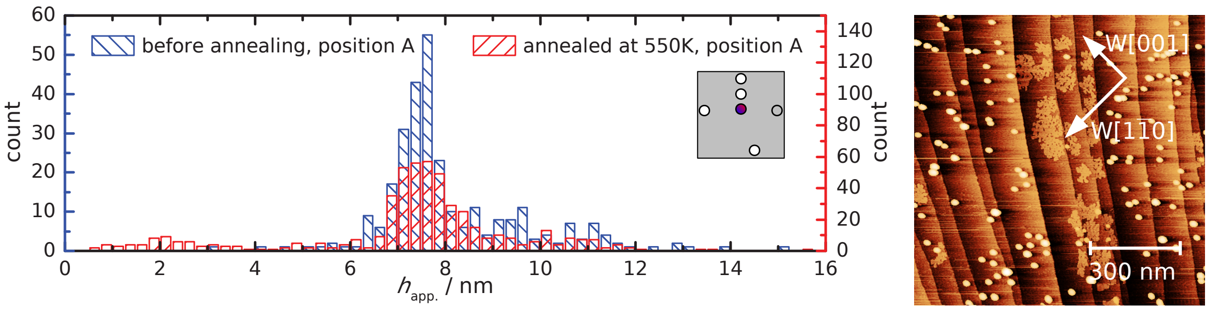

(a) Position *A*: slightly above center

(b) W-Tip; 1.0 V; 0.8 nA

Figure 4.9: Second sample of Co nanoparticles on tungsten carbide. Height distribution before and after annealing at 550 K.

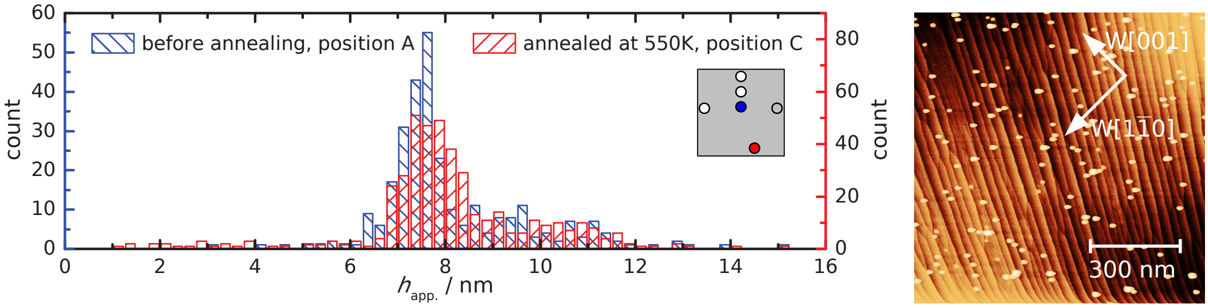

(a) Position *C*: lower edge to the right (b) W-Tip; .15 V; 0.8 nA

Figure 4.10: Second sample of Co nanoparticles on tungsten carbide. Height distribution before and after annealing at 550 K.

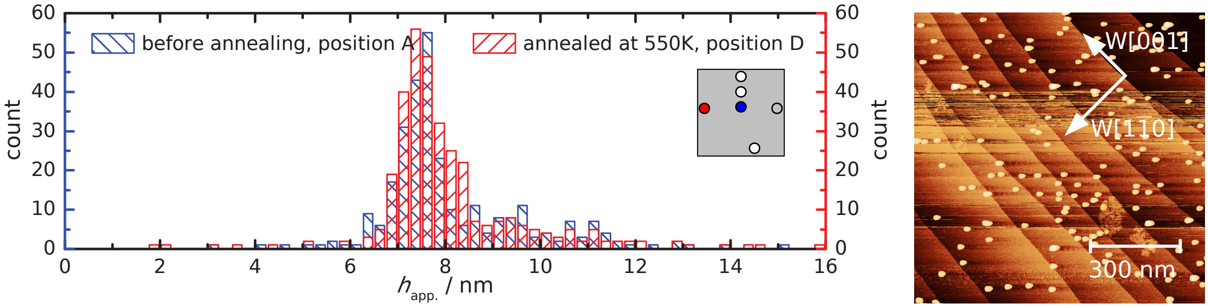

(a) Position *D*: left edge (b) W-Tip; .15 V; 0.8 nA

Figure 4.11: Second sample of Co nanoparticles on tungsten carbide. Height distribution before and after annealing at 550 K.

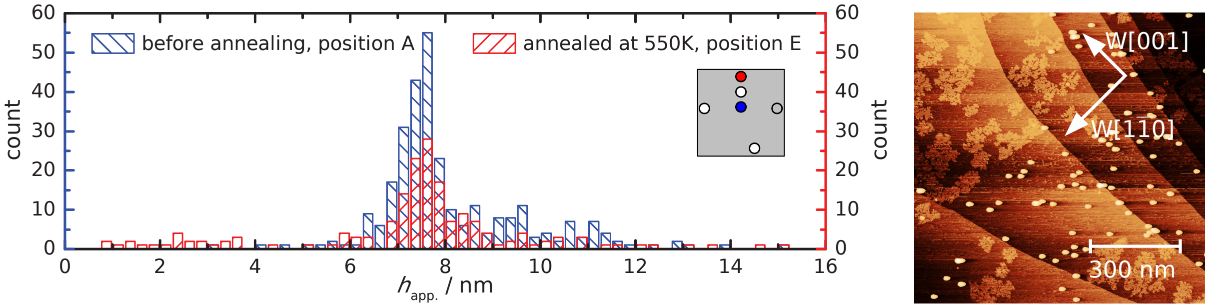

(a) Position *E*: upper edge (b) W-Tip; .15 V; 0.8 nA

Figure 4.12: Second sample of Co nanoparticles on tungsten carbide. Height distribution before and after annealing at 550 K.

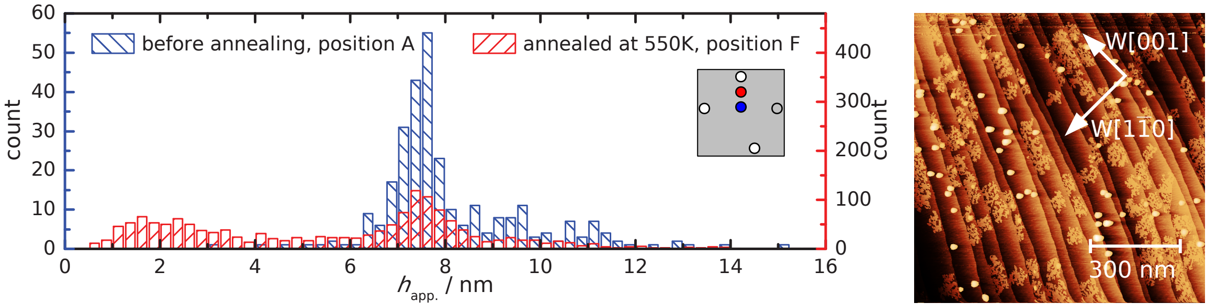

(a) Position *F*: half-way up (b) W-Tip; 1.0 V; 0.8 nA

Figure 4.13: Second sample of Co nanoparticles on tungsten carbide. Height distribution before and after annealing at 550 K.

contrast to the behavior on clean tungsten where all nanoparticles displayed signs of melting (see section 4.2.1).

The melting behavior showed a general trend with respect to the position on the substrate: Nanoparticles on the left side were predominantly intact while more nanoparticles on the right side had melted. This is probably a result of a slight temperature gradient caused by the manipulator's heating stage. The sample is isolated from the heating stage by a small gap and radiation is the primary mechanism of heat transfer. The sample holder has a round hole for the radiation to reach the sample's bottom. The edges of the sample are in contact with the sample holder and, as such, are shielded from the radiation. The direct contact with the sample holder and the reduced radiation may be sufficient to introduce a small temperature difference. The measurements of the first sample had determined the melting point with an accuracy of better than 10 K. It is feasible, that the temperature was slightly below the melting point or that the heat-up was slower on the edges of the sample.

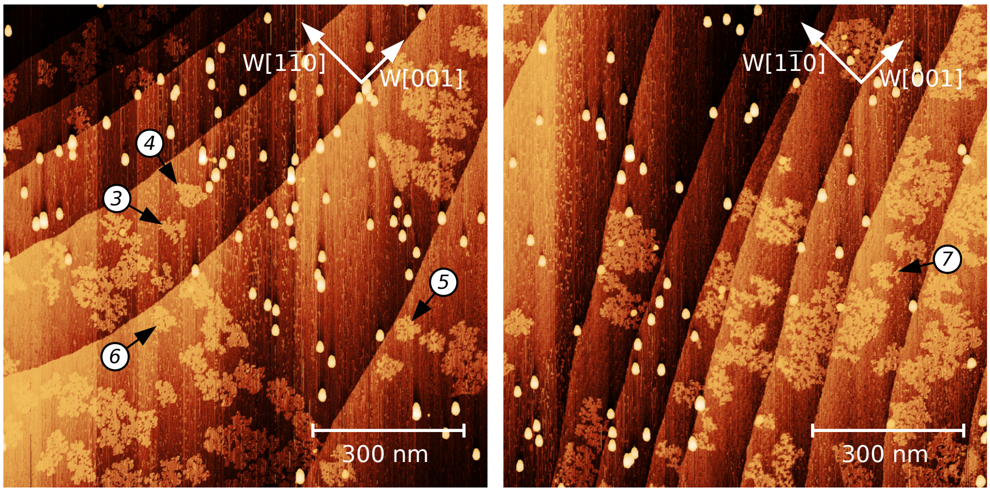

(a) (b)

Figure 4.14: Co nanoparticles on tungsten carbide after annealing at 550 K (second sample, position *E*). The STM images show some areas that feature intact nanoparticles and other areas that are covered with islands. W-Tip; 0.15 V; 0.8 nA

Two images, taken at the upper edge of the substrate (position *E*), are shown in figure 4.14. A size analysis of selected islands (*3–7*) revealed, that each of the smaller islands contained enough material to form a sphere of $\overline{d}_{\text{equiv.}} = (7.88 \pm 0.35)\,\mathrm{nm}$. This value is in good agreement with the height of the nanoparticles after deposition, i.e. these islands are each a remainder of one or possibly two nanoparticles. Wide ranging diffusion can be excluded because it would have lead to islands of arbitrary sizes.

This area was characterized by similar numbers of intact nanoparticles and monolayer islands. These two species were not evenly distributed. Some areas were covered with islands while other areas contained only nanoparticles. This split-up in different domains could indicate different substrate domains, such as different states of carbonization. Another, more likely explanation is that the split-up was the result of an *avalanche-like* melting. This could work like this: The melting point of the Co nanoparticles on W(110)/C-R(15×3) was $30\,\mathrm{K}$ higher compared to clean W(110). (One might also say that the carbon had a stabilizing effect on the nanoparticles.) One nanoparticle would start melting at some point and an unrolling carpet would spread around it. This diffusion area could reach other nanoparticles in its vicinity. The carbon's stabilizing effect would then be diminished and these nanoparticles would start melting too. The resulting unrolling carpet could reach further nanoparticles and the melting would spread even further.

The boundaries between empty and island-covered substrate can give further insights into the mechanisms. Figure 4.14(a) shows a straight boundary roughly parallel to W$[1\overline{1}0]$ across the central terrace. This boundary could indicate a diffusion barrier, such as a phase boundary.

4.2.3 Cobalt nanoparticles on W(110)/O-((1×1)×12)

Composition of raw material The nanoparticles were produced in the magnetron sputtering source. The sputtering target from *Hauner* was made of Co with a purity of $99.99\,\%$.

Sample preparation

The W(110)/O-$((1\times1)\times12)$ surface was prepared by oxygen annealing at $(1500\pm75)\,\mathrm{K}$ of a clean W(110) single crystal (see also section 4.1.3).

A first oxygen annealing was carried out to remove carbide from previous measurements. This was done for 20 minutes at $p_{\mathrm{O}_2} = 2\cdot10^{-6}\,\mathrm{mbar}$, followed by titanium sublimation to reduce the pressure and two subsequent flashing cycles at $2000\,\mathrm{K}$ and $1700\,\mathrm{K}$.

The O-$((1\times1)\times12)$ structure was prepared before each nanoparticle deposition. This was done at $p_{\mathrm{O}_2} = 10^{-7}\,\mathrm{mbar}$ for 20 minutes ($90\,\mathrm{L}$). The substrate was then quickly transferred to the analysis chamber ($p_{\text{ana}} < 3\cdot10^{-10}\,\mathrm{mbar}$) for LEED (e.g. figure 4.3(a)). Titanium sublimation was carried out during this time to reduce the preparation (deposition) chamber's pressure to $p_{\text{pre}} < 2\cdot10^{-9}\,\mathrm{mbar}$.[2] The sample was transferred back to the analysis chamber after 20 minutes of deposition.

---

[2] This is the best pressure that could be achieved within reasonable time. Later modifications of the magnetron sputtering source have eliminated this problem.

sample	**processing step**	***t* / min**	***T* / K**	**notes & observations**
A	oxygen annealing	20	1500	-
	LEED	-	*RT*	W(110)/O-(1×1)×12
	nanoparticle deposition	20	*RT*	-
	STM	-	*RT*	Co nanoparticles
	annealing	15	465	*estimated temperature*
	LEED	-	*RT*	W(110)/O-(1×1)×12
	STM	-	*RT*	*no apparent change*
	annealing	15	495	*estimated temperature*
	LEED	-	*RT*	W(110)/O-(1×1)×12
	STM	-	*RT*	*no apparent change*
	annealing	15	524	
	LEED	-	*RT*	W(110)/O-(1×1)×12
	STM	-	*RT*	*no apparent change*
	annealing	15	543	
	LEED	-	*RT*	W(110)/O-(1×1)×12
	STM	-	*RT*	*no apparent change*
	annealing	15	554	
	LEED	-	*RT*	W(110)/O-(1×1)×12
	STM	-	*RT*	*no apparent change*
	annealing	15	569	
	STM	-	*RT*	slight height reduction
B	oxygen annealing	20	1500	-
	LEED	-	*RT*	W(110)/O-(1×1)×12
	nanoparticle deposition	20	*RT*	-
	STM	-	*RT*	Co nanoparticles
	annealing	15	581	
	STM	-	*RT*	height reduction
	annealing	15	718	
	STM	-	*RT*	further height reduction
C	oxygen annealing	20	1500	-
	LEED	-	*RT*	W(110)/O-(1×1)×12
	nanoparticle deposition	20	*RT*	-
	STM	-	*RT*	Co nanoparticles
	annealing	7	1061	-
	STM	-	*RT*	height reduction, particle elongation, surface reconstruction
	LEED	-	*RT*	satellite lines along W$[1\bar{1}0]$

Table 4.1: Steps for preparation and examination of each sample.

STM measurements were done to determine the nanoparticles' sites and height distribution. Each sample was annealed at different temperatures and STM images were taken after sample cool-down. Procedures for each sample are outlined in table 4.1.

Results

Neither did the Co nanoparticles on sample *A* show any change nor did the LEED pattern change below $560\,\mathrm{K}$. A slight reduction in apparent height was observed at the final temperature step of $569\,\mathrm{K}$ (see figure 4.15). The average height shifted from $(8.4\pm1.6)\,\mathrm{nm}$ to $(7.4\pm2.3)\,\mathrm{nm}$. It is questionable if this change was statistically significant due to the broad height distribution on the one hand and a very low number of scanned nanoparticles on the other hand (50 particles at $569\,\mathrm{K}$). The nanoparticles appeared as round objects without any visible orientation and without signs of unrolling carpet.

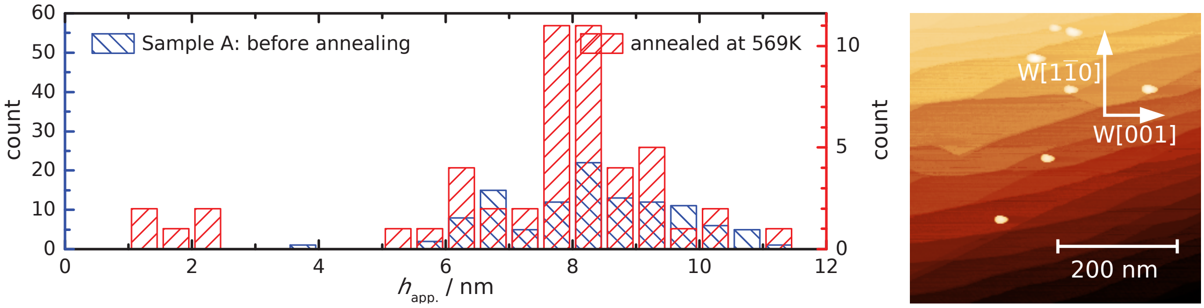

(a) ordinates are scaled in accordance with examined surface area (b) W-Tip; $1.0\,\mathrm{V}$; $0.3\,\mathrm{nA}$

Figure 4.15: Sample *A*: height distribution before and after annealing. STM image was taken after annealing at $569\,\mathrm{K}$.

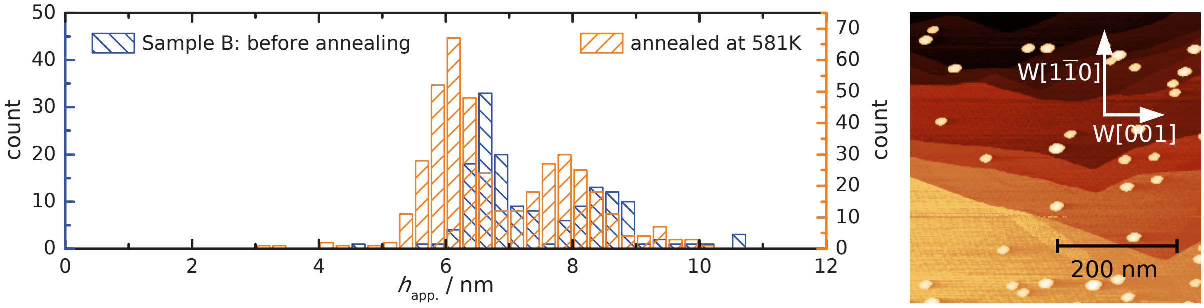

(a) ordinates are scaled in accordance with examined surface area (b) W-Tip; $1.0\,\mathrm{V}$; $0.8\,\mathrm{nA}$

Figure 4.16: Sample *B*: height distribution before and after annealing. STM image was taken after annealing at $581\,\mathrm{K}$.

Two additional samples, *B* and *C*, were prepared under identical conditions and annealed at higher temperatures. These were scanned more thoroughly to improve the statistical quality. Figures 4.16 and 4.17 show the distributions of apparent height. A distinct shift towards smaller sizes occurred at each annealing step. The average particle density per image on sample *B* dropped from $\rho_{\mathrm{NP}} = (154\pm5)\,\mathrm{\mu m}^{-2}$, after the first annealing, to $\rho_{\mathrm{NP}} = (122\pm38)\,\mathrm{\mu m}^{-2}$, after the second annealing. Density readings before

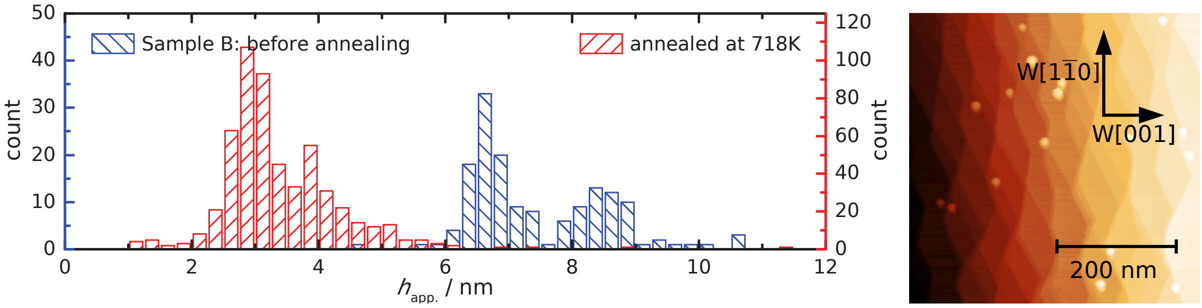

(a) ordinates are scaled in accordance with examined surface area (b) W-Tip; 1.0 V; 0.8 nA

Figure 4.17: Sample *B*: height distribution before and after annealing. STM image was taken after annealing at 718 K.

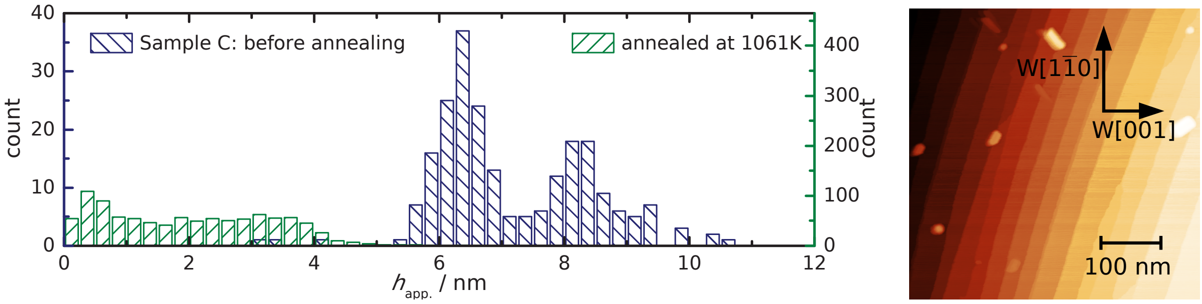

(a) ordinates are scaled in accordance with examined surface area (b) W-Tip; 1.0 V; 0.8 nA

Figure 4.18: Sample *C*: height distribution before and after annealing. STM image was taken after annealing at 1061 K.

annealing were not available due to strong, non-linear drift. Similar drift, although not as strong, was responsible for the large standard deviation after the second annealing. The nanoparticles lost height but they did not gain in width[3]. The formation of islands around existing particles or at terrace steps was not observed. A likely explanation for this behavior is, that the Co was incorporated into the surface structure. The lowest terrace in figure 4.16(b) exhibited two different domains which indicates a surface reconstruction too.

Sample *C* (annealed at 1061 K) showed a stronger reduction in height which was accompanied by a decrease in nanoparticle density from $\rho_{\mathrm{NP}} = 93\,\mu\mathrm{m}^{-2}$ to $35\,\mu\mathrm{m}^{-2}$.[4] The STM image 4.18 revealed elongated particles and a reconstructed surface structure. Roughly one third of all nanoparticles were sufficiently elongated to determine their orientation. The angular distribution is shown in figure 4.19(a). This distribution had two maxima pointing along the W[$1\bar{1}1$] and W[$1\bar{1}\bar{1}$] directions. The mean angle of these maxima was $\pm(36.4\pm10.3)^\circ$ with respect to W[$1\bar{1}0$]. This direction is similar to the aforementioned W$\langle 1\bar{1}1\rangle$ axes along $\pm35.26^\circ$.

In conclusion, if we assume, that the oxygen reconstruction is responsible for the orientation of the particles, then the two particle-directions each corresponded with a

---

[3] Changes in width are generally difficult to observe due to STM-tip convolution.

[4] This corresponds to a total number of particles of 226 and 988 respectively.

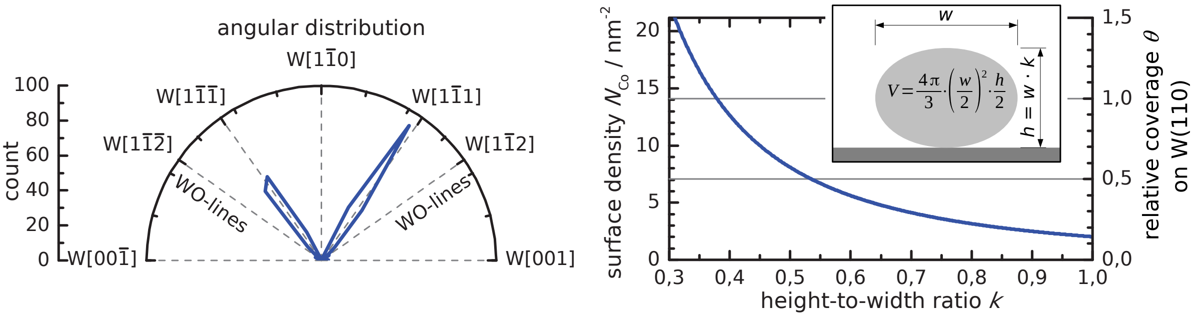

(a) Angular distribution of nanoparticles' orientations.

(b) Available Co coverage for figure 4.18. Inset: Simplified model to calculate the volume of a flattened nanoparticle.

Figure 4.19: Nanoparticle orientation and surface coverage after annealing at 1061 K (sample C).

surface-domain. If we assume that the tungsten surface is responsible for the orientation, then the two particle-directions were a result of the two-fold symmetry of W(110).

Surface reconstruction Figure 4.20 (see also 4.18(b)) shows, how the melting of Co nanoparticles caused a reconstruction of the tungsten-oxide surface. Horizontal lines had appeared. LEED in the center of the sample showed vertical satellite lines along the tungsten spots which are in agreement with the STM image. This new pattern was observed in the center of the sample, i.e. where nanoparticles had been deposited. The W(110)/O-((1×1)×12) pattern was still visible at the edges of the sample, i.e. outside of the area of deposition. This is a clear indication that the tungsten-oxide itself was stable at 1061 K, which is in agreement with previous reports [43, 49]. The additional Co nanoparticles/atoms are therefore responsible for the reconstruction.

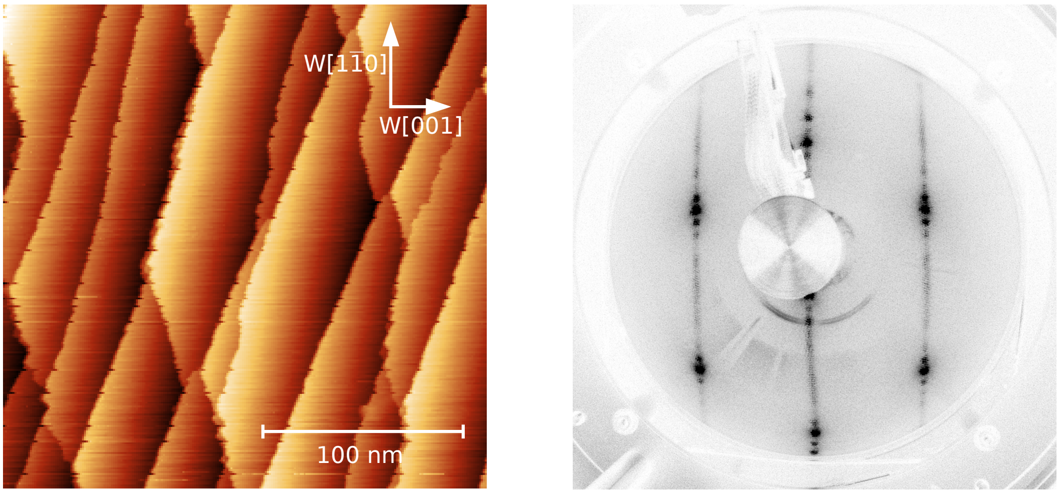

(a) STM image: W-Tip; 1.0 V; 0.8 nA

(b) LEED image (86 eV)

Figure 4.20: Sample C after annealing at 1061 K: Formation of horizontal lines along W[001] as a result of surface reconstruction.

The distance between lines was $d_{\text{lines}} = (2.99\pm0.59)\,\text{nm}$ which was obtained from a fast Fourier transform of STM images (resolution of $949\,\text{pm}\cdot\text{pixel}^{-1}$). According to this, the line distance is approximately 6.68 times larger than the lattice spacing of tungsten in $[1\bar{1}0]$-direction or $2\cdot6.68 = 13.36$ times larger than the distance between adjacent W$[001]$-rows. The distance between adjacent satellite spots of the LEED image is approximately 13.8 times smaller than the distance between tungsten spots in $[1\bar{1}0]$-direction.

The satellite spots were fainting further away from the main spots. This fainting and the non-integral number of unit-cells indicate a short-ordered relation between the tungsten and the surface reconstruction.

The maximum surface coverage from the melting of nanoparticles is an important factor to understand this process. The number of Co atoms N_{Co} per area can be calculated as follows:

$$\begin{aligned} N_{\text{Co}} &= \frac{1}{A}\cdot\frac{\sum_{i=1}^{n} m_i}{m_{\text{Co}}} \\ &= \frac{\rho_{\text{Co}}}{A\cdot m_{\text{Co}}}\cdot\sum_{i=1}^{n} V_i \\ &= \frac{\rho_{\text{Co}}}{A\cdot m_{\text{Co}}}\cdot\frac{\pi}{6\cdot k^2}\cdot\sum_{i=1}^{n} h_i^3 \end{aligned} \tag{4.1}$$

with apparent height h, the flattening (i.e. the height-to-width ratio) k, density $\rho_{\text{Co}} = 8900\,\text{kg}\cdot\text{m}^{-3}$, and atomic weight $m_{\text{Co}} = 9.78609\cdot10^{-26}\,\text{kg}$ [118]. The summation[5] included all particles in area A before annealing. It was based on the assumption that the observed height distribution was representative of the whole sample. The assumed geometric form is shown in the inset of figure 4.19(b).

The number of atoms obtained from this calculation had to be put in relation to the number of free sites. Pseudomorphic growth on W(110) was assumed to get a first estimate. The corresponding surface density is $N_{\text{Co}} = 14.1\,\text{atoms}\cdot\text{nm}^{-2}$. Figure 4.19(b) shows the number of cobalt atoms per surface area and the relative coverage θ for different aspect ratios k. For the given sample the relative coverage on W(110) would be $\theta = 0.19$ for an aspect ratio of $k = 0.85$ [119].

4.2.4 Cobalt nanoparticles on W(110)/O-p(2×1)

Composition of raw material The nanoparticles were produced in the magnetron sputtering source. The Co sputtering target from *MaTecK* had a purity of $99.9\,\%$.

Sample preparation

The W(110)/O-p(2×1) surface was prepared as outlined in section 4.1.2. Air was introduced at the connecting tube between the source chamber and preparation chamber during deposition. Two depositions were made on the same substrate. The QMF was set to $d_{\text{QMF}} = 6.35\,\text{nm}$ for deposition on the lefthand side and $d_{\text{QMF}} = 8.30\,\text{nm}$ on the righthand side. Four annealing steps were done at temperatures of 553, 573, and two times $593\,\text{K}$. Each annealing lasted 15 minutes.

The p(2×1) structure was identified by LEED at the end of the measurements (figure 4.21(a)).

---

[5] This is equivalent to an integration over the height distribution in figure 4.18(a) before annealing.

Results

The deposition resulted in a particle density of $\rho_{\mathrm{NP}} = 167\,\mu\mathrm{m}^{-2}$ on the lefthand side of the sample, compared to $92\,\mu\mathrm{m}^{-2}$ on the righthand side. The development throughout the annealing steps is shown in figure 4.22. The lowest temperature was already sufficient to start the melting process of the nanoparticles. Some nanoparticles displayed an adjacent monolayer, an indicator of unrolling carpet behavior. Some nanoparticles had a rectangular form. The orientation of these nanoparticles was rotated by approximately 45° with respect to $\mathrm{W}[001]$. An orientation along $\mathrm{W}\langle 110\rangle$ could also be possible but this seems less likely.

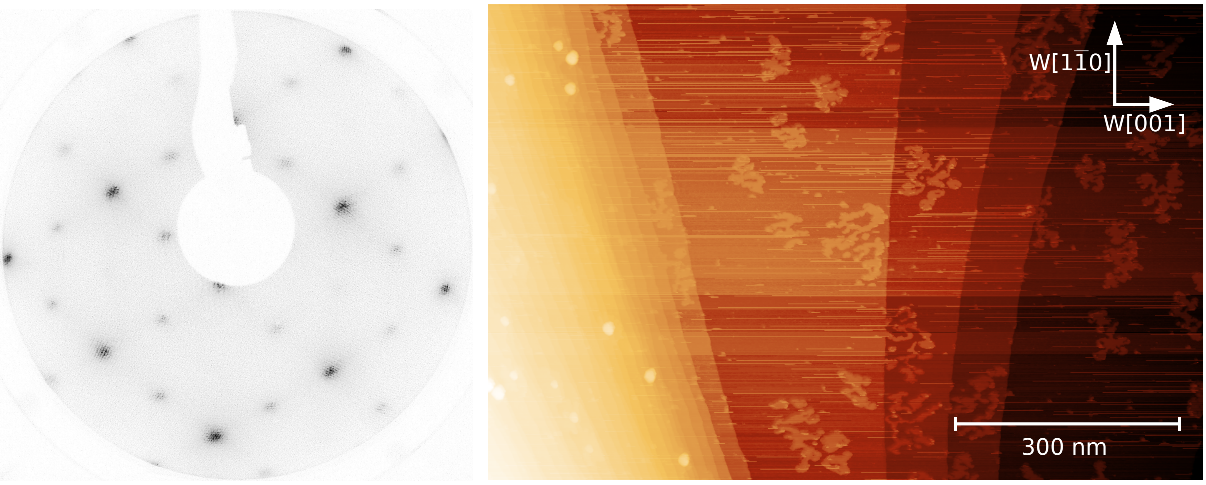

(a) LEED pattern at the end of the measurements. (112 eV)

(b) STM image of the righthand side. W-Tip; 1.0 V; 0.8 nA

Figure 4.21: Co nanoparticles, deposited on oxidized W(110), after the final annealing step.

The next annealing step (573 K) enhanced the previously observed effects: The unrolling carpet was spreading over tens of nanometers and monolayer islands formed. Areas with many islands had a reduced density of the nanoparticles and vice versa.

The distribution of heights (figure 4.22) gives some additional insight into the stability of different heights. The first few annealing steps caused a continuous height reduction on both sides of the sample. The nanoparticles reached an average height of roughly $h_{\mathrm{app.}} = (3.1 \pm 1.9)\,\mathrm{nm}$ after two annealing steps on the right side and after three steps on the left side. The additional annealing steps did not reduce the height but a steady drop of the area density occurred. The lefthand side required more annealing steps because the initial height was larger than on the righthand side.

Figure 4.21(b) shows the surface on the righthand side after the final annealing steps. The islands had a ramified shape. The islands' edges were predominantly oriented along $\mathrm{W}\langle 112\rangle$. The corners were more round and the shape was more compact in comparison to the melting on carbide (see section 4.2.2). Most of the remaining nanoparticles were located on small terraces. A likely explanation is that step edges had constituted a diffusion barrier (*Ehrlich-Schwoebel* barrier). Thus the cobalt concentration remained high because the diffusion was partly suppressed.

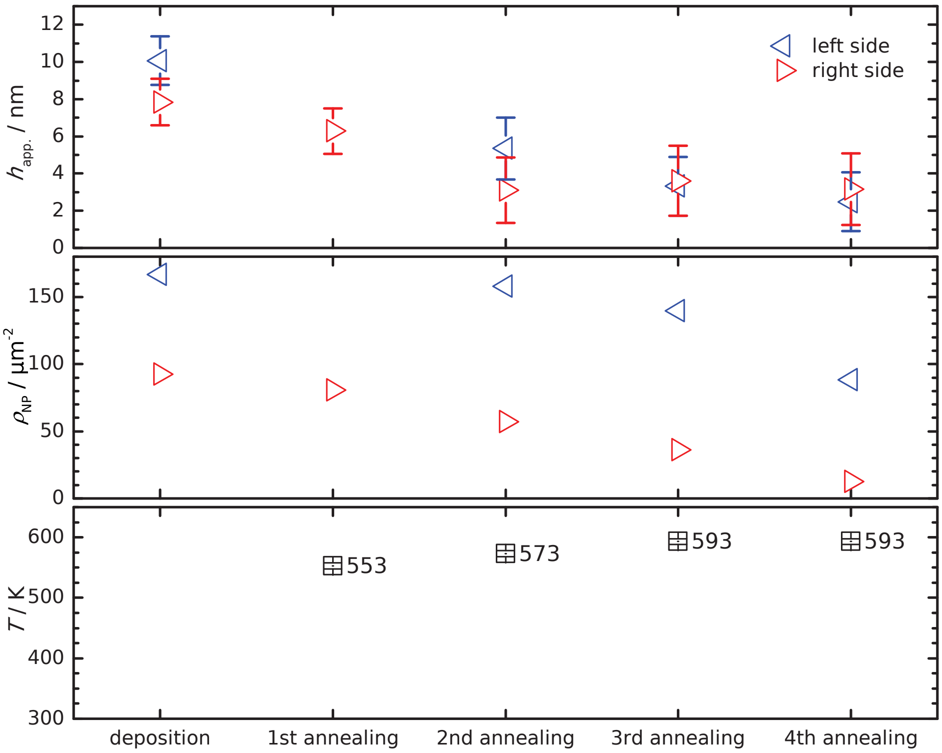

Figure 4.22: Co nanoparticles on oxidized W(110). Development of apparent height $h_{app.}$ and area density ρ_{NP} of the nanoparticles as a result of the annealing.

4.2.5 High coverage of cobalt nanoparticles on W(110)/O-p(2×1)

Composition of raw material The nanoparticles were produced in the magnetron sputtering source. The sputtering target from *MaTecK* was made of Co with a purity of $99.9\,\%$.

Sample preparation

The QMF was set to a particle diameter of $d_{QMF} = 7.7\,\mathrm{nm}$. Five minutes of deposition on the whole substrate were followed by 10 minutes of deposition on the righthand side only.

The W(110)/O-p$(2{\times}1)$ surface was prepared as outlined in section 4.1.2. Air was introduced during deposition at the connecting tube between the source chamber and preparation chamber. The p$(2{\times}1)$ structure was identified by LEED before the first annealing step. Two annealing steps were done, each lasting 45 minutes at a temperature of approximately $613\,\mathrm{K}$. The LEED pattern was continuously monitored during the second annealing which means that the sample was thus facing the LEED screen and that the temperature could not be measured pyrometrically. The sample was examined in STM for another day and a half. Another LEED measurement concluded the measurements.

Results

The deposition resulted in an already high particle density of $325\,\mu\mathrm{m}^{-2}$ on the lefthand side of the sample and $470\,\mu\mathrm{m}^{-2}$ on the righthand side. This gradient was expected because the deposition on the left side lasted only 5 minutes, compared to 15 minutes on the righthand side. The righthand side however did not have three times the density because the intensity of the nanoparticle beam had decreased over time. The average height was $h_{\mathrm{app.}} = (8.3\pm1.5)\,\mathrm{nm}$ and $h_{\mathrm{app.}} = (8.8\pm2.1)\,\mathrm{nm}$ respectively. The LEED image, that had been taken before annealing, revealed the p(2×1) pattern (compare figure 4.2(a)).

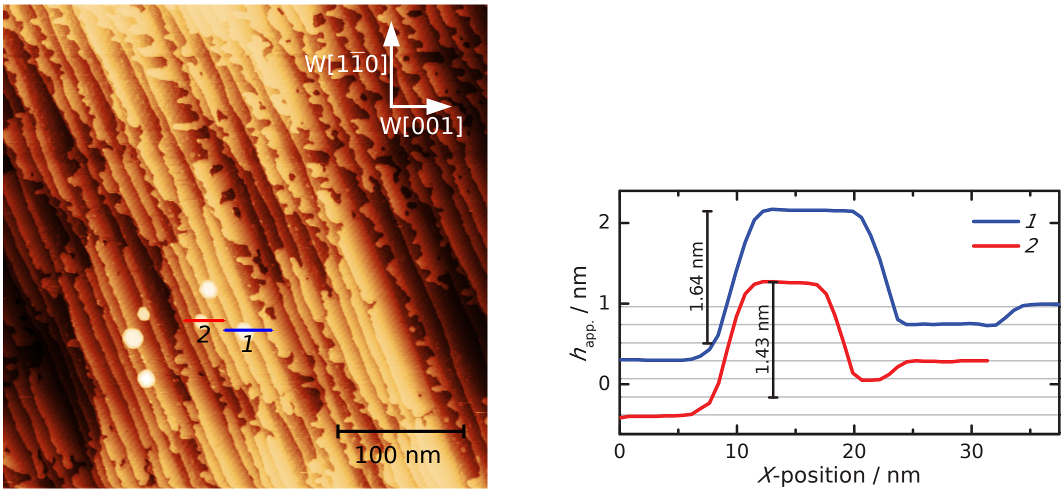

(a) STM image: The group of 6 remaining Co nanoparticles on oxidized W(110). The surrounding area was free of nanoparticles. W-Tip; 1.0 V; 0.8 nA

(b) Height profiles of hexagonal Co islands as designated in (a). Profile *1* has a height of 8 hcp Co layers, profile 2 of 7 hcp Co layers. Gray lines represent W terraces.

Figure 4.23: Left side of the sample after annealing for 45 minutes at up to 613 K.

The first annealing caused an almost complete melting on the lower-coverage, lefthand side and very few nanoparticles remained: The density dropped 70-fold to $\rho_{\mathrm{NP}} = 4.5\,\mu\mathrm{m}^{-2}$ and the height dropped below $h_{\mathrm{app.}} = 2.4\,\mathrm{nm}$. A careful analysis showed that the nanoparticles had a hexagonal form (figure 4.23(a)) and a flat top surface (figure 4.23(b)). Their heights h_i were integral multiples of $h_{\mathrm{Co}} = (203\pm6)\,\mathrm{pm}$:

$$h_i = n_i \cdot h_{\mathrm{Co}} \tag{4.2}$$

where n_i was between 5 and 12. h_{Co} is virtually identical to the distance between the hexagonal lattice planes of Co. The location of these nanoparticles was highly inhomogeneous. A total area of $1.5\,\mu\mathrm{m}^2$ was examined but 6 out of 7 nanoparticles where bunched together in an area of approximately $(90\cdot70)\,\mathrm{nm}^2 = 6.3\cdot10^{-3}\,\mu\mathrm{m}^2$ (figure 4.23(a)). That means that 85 % of the nanoparticles were in 0.4 % of the area. The available data cannot tell why this group of highly localized particles had not melted. One could speculate about inhomogeneities of the substrate. A more likely explanation is however, that these multilayer islands were the last remains of much larger concentration of nanoparticles. I.e. the overabundance of Co prevented the unrolling carpet and these islands were the result.

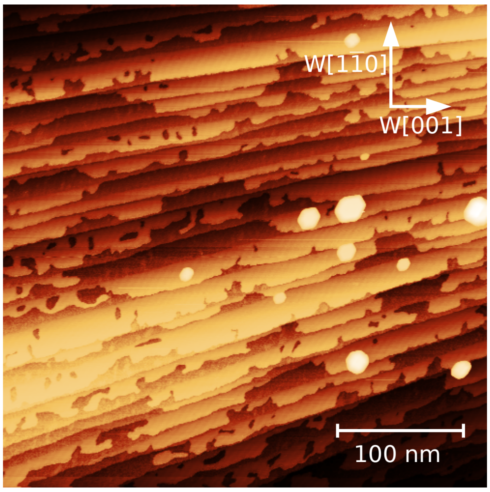

Figure 4.24: Right side of the sample: STM image of Co nanoparticles on oxidized W(110) after annealing for 45 minutes at up to 613 K. The surrounding area was similar. W-Tip; 1.0 V; 0.8 nA

The Co from the melting process was distributed in a monolayer across the substrate. Most of the material was attached to the lower edge of the terrace steps. Some vacancy islands existed while some parts of the monolayers were protruding in W[001] direction. These shapes resembled the results of Co on W(110) (see end of subsection 4.2.1). Two differences were revealed in STM: The corners were more round and the height difference between a tungsten terrace and the adjacent cobalt layer appeared slightly higher.

The density on the righthand side decreased to 32 % of the initial value. The majority of the nanoparticles melted to a monolayer. The apparent height of the remaining particles dropped to $(2.4 \pm 0.9)\,\mathrm{nm}$. Figure 4.24 shows a typical image of the surface: The remaining nanoparticles were relatively evenly distributed. Most featured a hexagonal form and a flat top facet. One side of the hexagonal islands was generally aligned in direction of W[001]. A few particles had an octagonal form with a round top (e.g. on right edge of figure 4.24). This form can be associated with a truncated octahedron with one square facet facing upwards. The square facet's edges are parallel/perpendicular to W[001].

Similar results were obtained at the second annealing. The nanoparticle density decreased to $2.7\,\mu\mathrm{m}^{-2}$, i.e. to 0.6 % of its initial value. The apparent height decreased to $h_{\mathrm{app.}} = (2.1 \pm 0.9)\,\mathrm{nm}$. The remaining nanoparticles were unevenly spread across the surface. The particles were further apart compared to the left side of the sample. The remaining particles were on terraces that had a width of less than 40 nm. These particular terraces were fully covered by a monolayer of Co (or an oxide thereof). Wider terraces (figure 4.25(a)) were free of nanoparticles and multilayer islands.

This kind of distribution supports the aforementioned theory that the multilayer islands were remainders of fluctuations in the initial concentration. Multilayer islands only occurred/remained after the substrate had been covered in one monolayer. The 2-dimensional diffusion on wide terraces was not hindered by step edges and the Co spread quickly. Small terraces limit the available area for diffusion and a high local concentration will take significantly longer to disperse.

The morphological anisotropy influences the islands' shape as well. The effectively higher concentration on small terraces lead to compact islands while the islands on the wide terraces showed a high degree of ramification.

The LEED pattern was also recorded during the second annealing. The initial pattern was the p(2×1) structure, which can be associated with oxygen and it was observed for 12 minutes during annealing. Additional satellite spots were observed after 15 minutes and they intensified for the rest of the annealing process and remained after cool-down

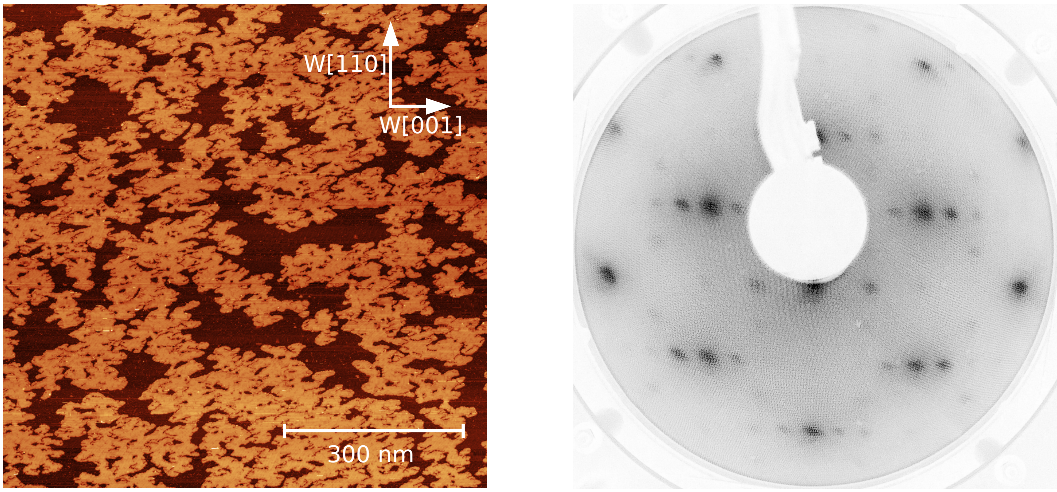

(a) STM image: Monolayer island of Co. W-Tip; 1.0 V; 0.8 nA

(b) LEED pattern: A superposition of O-p(2×1) and Co(0001) on W(110). (132 eV)

Figure 4.25: After two times annealing of Co nanoparticles on W(110)/O-p(2×1).

(figure 4.25(b)). This additional pattern is a result of a closed monolayer of Co(0001) on W(110). The satellite spots were observed by e.g. Fritzsche et al. for 1 to 4 ML Co(0001) on W(110) [60]. The orientation of this film is Co[$11\bar{2}0$] parallel to W[001] and it is called *Nishiyama-Wassermann* (see also section 2.4.1).

The difference between the two sample positions can be explained by two factors. (1) The righthand side featured a higher particle density, which puts certain constraints on the film growth. (2) The righthand side was closer to the fixture of the manipulator and the temperature might be slightly lower there.

4.3 Nickel-iron nanoparticles

Nickel-iron nanoparticles were successfully prepared with both nanoparticle sources. Particles from the ACIS were used for the annealing tests.

4.3.1 Nickel-iron nanoparticles on W(110), (0.50/0.50)-alloy

Previous publication: The measurements in this subsection were performed as part of the master's thesis of M. Werner [71]. My data analysis was done independently from his results. The results of this analysis have been published [54]. This paper was written by me. A round-up of this section is pending publication [120]. The main-body of that article was written by me.

Composition of raw material: The NiFe nanoparticles were produced in the ACIS. *Permenorm* made by *Vacuumschmelze GmbH*[6] was used as the cathode's raw material. Its

---

[6] The alloy was acquired from *Sekels GmbH*.

metallic composition was given as $47.50\,\%$ Ni, $0.48\,\%$ Mn, $0.19\,\%$ Si, and a remainder of Fe. No statement could be made concerning the amount of carbon or other impurities.

Sample preparation

The samples were prepared in accordance with section 3.7. The temperature of some annealing steps was lower than the lower temperature limit of the radiation thermometer. The respective temperatures were estimated based on the linear behavior of the heater and they were readjusted under consideration of the temperatures at higher heating power.

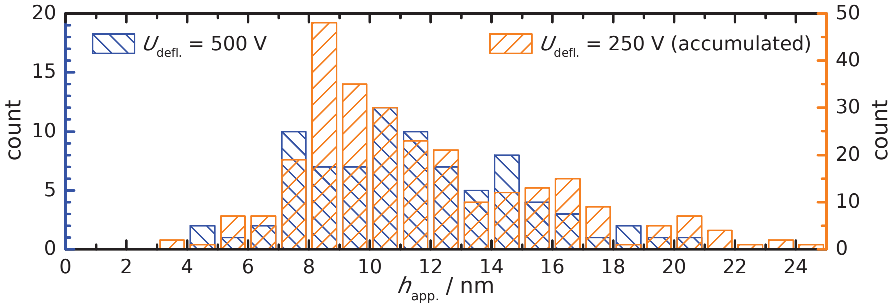

Figure 4.26: $Ni_{50}Fe$ nanoparticles: height distribution after deposition with different deflection voltages.

Figure 4.26 shows the height distributions of the nanoparticles' at deflection voltages of $U_{\text{defl.}} = -250\,\text{V}$ and $-500\,\text{V}$. The 250-V-distribution was accumulated over six consecutive measurements. The average height was $\overline{h}_{\text{app.}} = (11.9 \pm 4.5)\,\text{nm}$ and $(11.6 \pm 3.8)\,\text{nm}$ respectively. This is in agreement with other measurements from the ACIS [71, 90], which show that the voltage-to-volume ratio is increasing at $|U_{\text{defl.}}| \lessapprox 500\,\text{V}$.

Annealing

The lowest annealing temperature was estimated to be around $490\,\text{K}$. No change in height or form of the nanoparticles was observed after 30 minutes of annealing.

The next higher temperature step was at approximately $520\,\text{K}$. Two samples were prepared and annealed for 30 minutes and 120 minutes respectively. The results are shown in figure 4.27. Both samples showed islands of one monolayer in height. Some of these islands had a small remainder of its original nanoparticle on top. The islands had a ramified shape after 30 minutes and the area of the islands in figure 4.27(a) was examined: Islands *1* and *2* contained enough material for a sphere of $d_{\text{equiv.}} \approx 6.3\,\text{nm}$ and $d_{\text{equiv.}} \approx 6.9\,\text{nm}$ respectively. Islands *3* featured a small nanoparticle of $h_{\text{app.}} = 3.3\,\text{nm}$. It would yield a sphere of sphere of $d_{\text{equiv.}} \approx 8.2\,\text{nm}$. Some material had already accumulated at the terrace step close to this islands.

The number of atoms that diffused away from the islands increased during the longer annealing time. This reduced the diameter of the islands by a factor of two. Islands *4* and *5*, including the visible agglomerations at terrace step edges, would have yielded equivalent spheres of $d_{\text{equiv.}} \approx 7.5\,\text{nm}$ and $d_{\text{equiv.}} \approx 6.6\,\text{nm}$. The remaining islands were more compact and the diffusing atoms had agglomerated at the step edges of the tung-

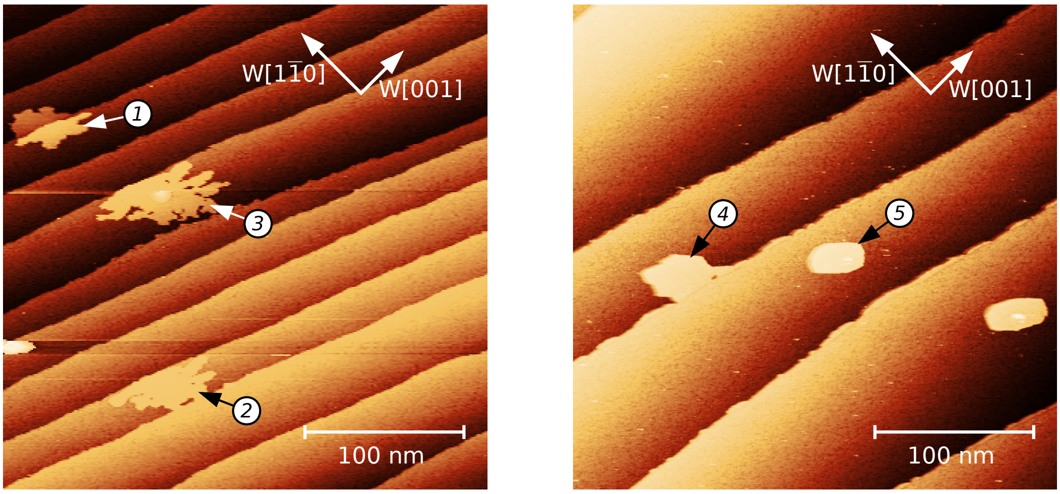

(a) 30 minutes of annealing: ramified islands as a result of unrolling carpet.

(b) 120 minutes of annealing: compact islands. Agglomeration at step edges.

Figure 4.27: STM images of $Ni_{0.50}Fe$ nanoparticles after annealing at $520\,\mathrm{K}$: PtIr-Tip; $1.0\,\mathrm{V}$; $0.8\,\mathrm{nA}$

sten substrate. Step edges without adjacent islands were covered, too. This indicates a high mobility of these atoms at $520\,\mathrm{K}$.

Figure 4.28(a) shows the result of annealing for 30 minutes at up to $553\,\mathrm{K}$. It can be considered to be a step between the two previous measurements because the temperature was higher but the duration was shorter. Some islands still exhibited ramification but compact shapes existed too. Ramified shapes were more common in areas of narrow terraces and in areas of higher nanoparticle density. This can be explained when considering the free area around a nanoparticle: The probability for an atom to return to its origin is significantly higher when its diffusion is constrained by step edges. The shrinking of the islands due to particle loss is an indicator for the *hit-and-stick* regime [1, sec. 14.2.2]. The diffusion along the islands' edges is not favorable when compared to free diffusion across the W-surface. This may be a direct result of the islands' pseudomorphic growth on W(110). The resulting strain is reducing the binding energy between the Ni/Fe atoms.

Seventeen islands from figure 4.28(a) were analyzed to estimate their average size and the corresponding spherical diameter. The average was $\overline{d}_{\text{equiv}} = (7.2 \pm 1.2)\,\mathrm{nm}$. The height distribution is shown in figure 4.28(b) in comparison with the cumulative height distribution. The equivalent diameters were smaller than the pristine heights. This height loss was most likely a result of the surface diffusion. Some atoms had already moved away from the islands. Inaccurate calculation of the equivalent spherical diameter $d_{\text{equiv.}}$ could have contributed, too.

All three measurements have in common that they showed a slight preference for diffusion along the W[001] axis. Diffusion across step edges did not occur. This is particularly obvious when considering the nanoparticles/islands on narrow terraces (see lower right half of figure 4.28(a)).

The result of annealing at $1029\,\mathrm{K}$ is shown in figure 4.29. The surface was covered with small islands with an average equivalent diameter of $\overline{d}_{\text{circle}} = (13.06 \pm 5.37)\,\mathrm{nm}$ and an average surface area of $\overline{A} \approx 156\,\mathrm{nm}^2$. That means that an average islands contained

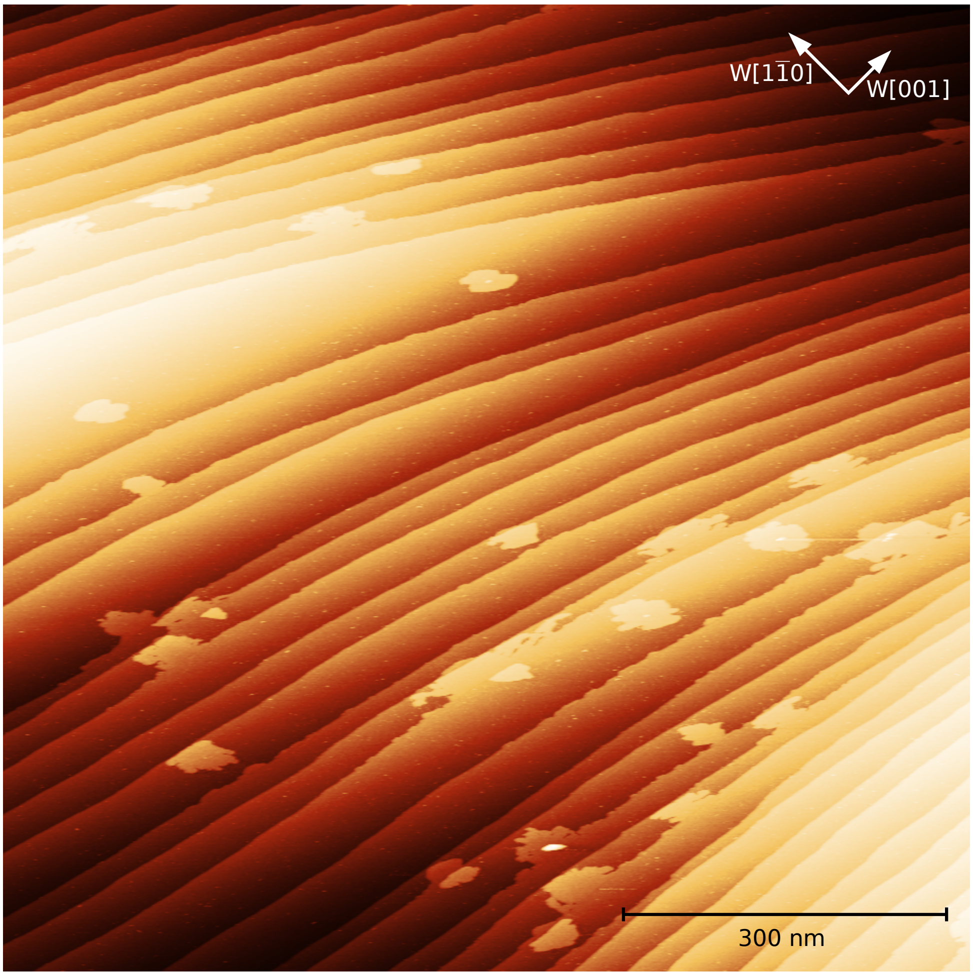

(a) STM image: Nanoparticles have melted. Islands have compact shapes on wider terraces (upper left half). Ramified islands are prevalent on narrow terraces (lower right half). PtIr-Tip; 1.0 V; 0.8 nA

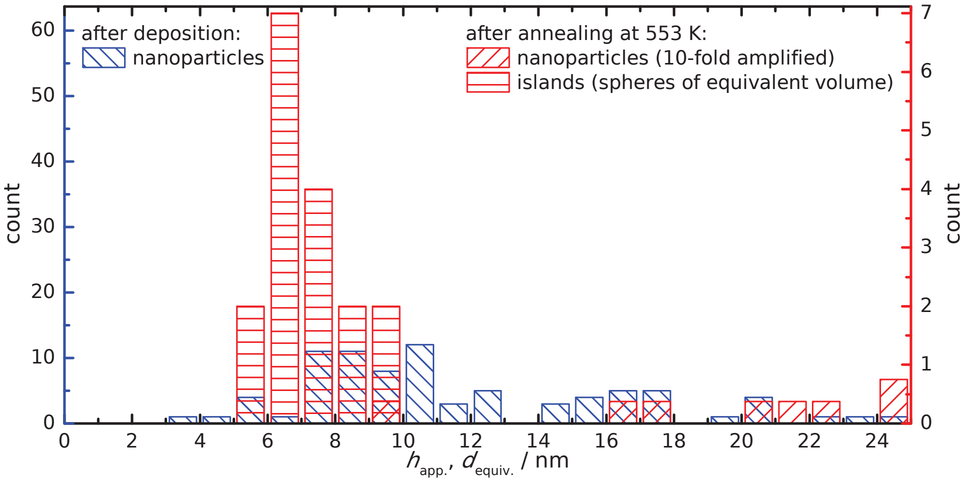

(b) Height distribution after deposition in comparison with height distribution after annealing. The number of remaining nanoparticles after annealing has been amplified 10-fold for better visibility. Monolayer islands are being represented by their equivalent spherical diameter.

Figure 4.28: $Ni_{0.50}Fe$ nanoparticles after 30 minutes of annealing at 553 K.

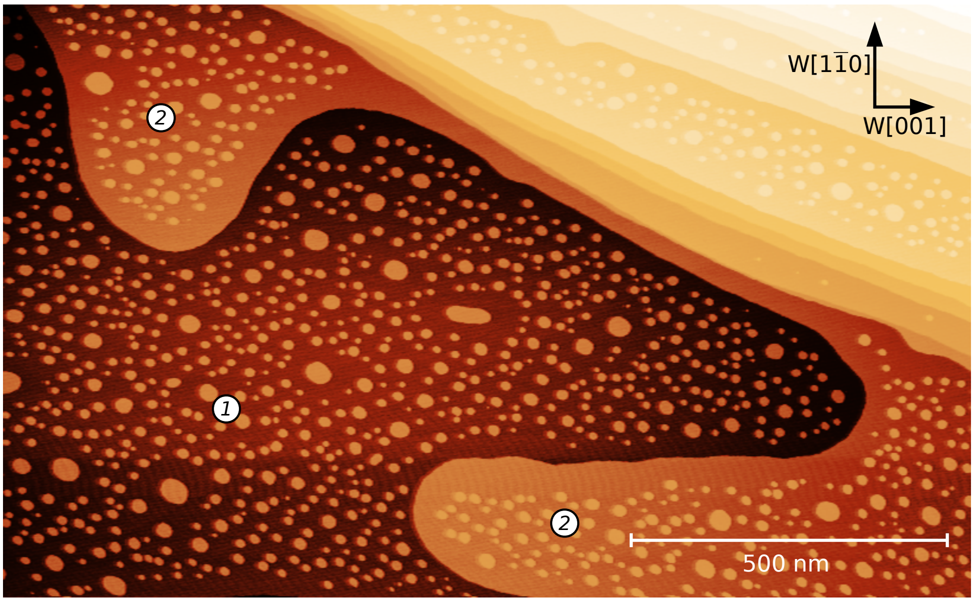

Figure 4.29: STM image after 30 minutes of annealing at 1029 K: $Ni_{0.50}Fe$ nanoparticles have melted completely and small islands are uniformly distributed. W-Tip; 1.0 V; 1.8 nA
1: This tungsten substrate is covered with small NiFe islands.
2: These agglomerated NiFe surfaces are covered with small NiFe islands.

about 2200 atoms or roughly 2 % of an average nanoparticle. The relative coverage on the low terrace *1* was $\theta = 17\,\%$. The total coverage θ_{total} can be calculated based on the particle distribution before annealing. The first step is to calculate the number of available Fe and Ni atoms N_{NiFe} per area, analog to equation 4.1:

$$\begin{aligned} N_{\text{NiFe}} &= \frac{1}{A} \cdot \frac{\sum_{i=1}^{n} m_i}{m_{\text{NiFe}}} \\ &= \frac{\rho_{\text{NiFe}}}{A \cdot m_{\text{NiFe}}} \cdot \sum_{i=1}^{n} V_i \\ &= \frac{\rho_{\text{NiFe}}}{A \cdot m_{\text{NiFe}}} \cdot \frac{\pi}{6 \cdot k^2} \cdot \sum_{i=1}^{n} h_i^3 \end{aligned} \tag{4.3}$$

with apparent height h, flattening factor $k = 0.85$ [119], bulk density $\rho_{\text{NiFe}} = 8240\,\text{kg}\cdot\text{m}^{-3}$, and an average atomic weight $m_{\text{NiFe}} = 9.509785\cdot10^{-26}\,\text{kg}$. The total coverage can be estimated to:

$$\theta_{\text{total}} = \frac{N_{\text{NiFe}}}{N_{\text{NiFe}}(\theta{=}1)} \approx 41\,\% \tag{4.4}$$

with surface density $N_{\text{NiFe}}(\theta{=}1) = 14.1\,\text{atoms}\cdot\text{nm}^{-2}$ under the assumption of pseudomorphic growth. The total coverage θ_{total} was below 1 ML, which means that the surface *1* below the islands was tungsten. The islands covered only $\theta = 17\,\%$ of the surface. The remaining material had formed wide terraces *2*. The terraces *1* and *2* exhibit a similar density of islands.

4.3.2 Nickel-iron nanoparticles on W(110), (0.25/0.75)-alloy

Previous publication: The measurements for this subsection were part of K. Scheiff's bachelor's thesis [90]. I have analyzed the resulting images independently and without his help. A round-up of this section is pending publication [120]. The main-body of that article was written by me.

Composition of raw material: The raw material from *MaTecK* had a nominal composition of $25\,\%_{\mathrm{at}}$ Ni and $75\,\%_{\mathrm{at}}$ Fe with a purity exceeding $99.9\,\%$. A cathode for the ACIS was lathed in-house.

Sample preparation

The W(110) surface was prepared in accordance with section 3.7. The nanoparticles were produced in the ACIS and the ACIS's quadrupole deflector was set to a deflection voltage of $U_{\mathrm{defl.}} = 750\,\mathrm{V}$. The nanoparticles were analyzed after deposition by STM. Each sample was annealed on the manipulator's integrated heater if the area density of nanoparticles had been deemed to be sufficiently high. The effects of these annealings were analyzed in STM after cool-down.

Each annealing lasted 15 minutes. The temperature was between 546 and $929\,\mathrm{K}$. The measurement at lower temperatures was repeated for two different sizes of nanoparticles by changing the voltage $U_{\mathrm{defl.}}$ of the mass selector to 700 and $850\,\mathrm{V}$.

Results

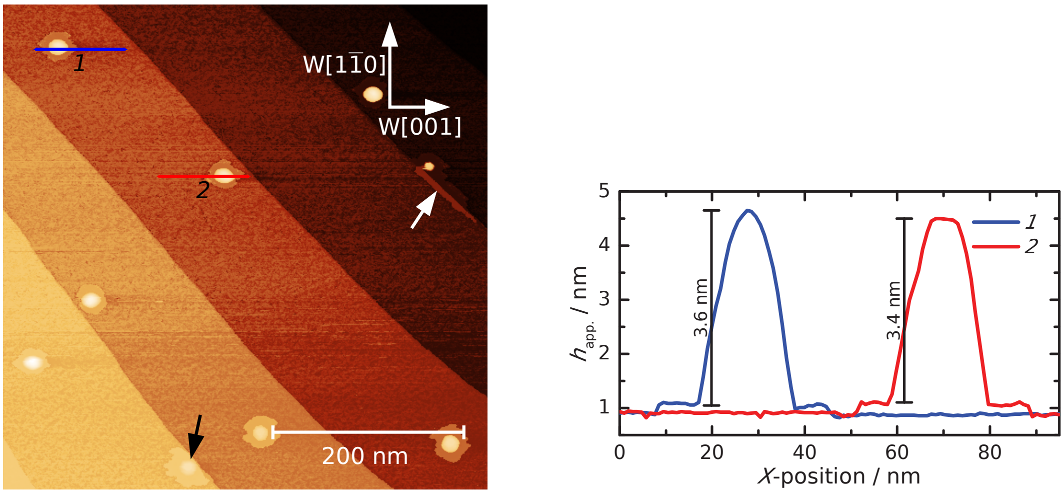

(a) STM image: Unrolling carpet behavior. The arrows indicate nanoparticles that were significantly affected by step edges. See figure 4.32(c) for height distribution. W-Tip; $1.0\,\mathrm{V}$; $0.8\,\mathrm{nA}$

(b) Height profiles of nanoparticles as designated in (a). Nanoparticle *1* has round form. Smaller nanoparticle *2* has a flat top.

Figure 4.30: $Ni_{0.25}Fe$ nanoparticles on W(110) after annealing for 15 minutes at up to $553\,\mathrm{K}$. Crystallographic and morphological anisotropy influence the diffusion depending on the nanoparticles' position.

Figure 4.30 shows an STM image of nanoparticles after annealing at $553\,\mathrm{K}$. A single-monolayer diffusion zone had formed around each nanoparticle. The zones had an average length of 40 to $50\,\mathrm{nm}$ along W$[001]$ and 30 to $40\,\mathrm{nm}$ along W$[1\bar{1}0]$. The general shape beared close resemblance to the $Ni_{0.5}Fe$-results (see figure 4.28). Pointed ends (one or more) appeared in the W$\langle 001 \rangle$ directions. Nanoparticles in the vicinity of step edges (indicated by arrows in figure 4.30(a)) experienced the influence of the morphological anisotropy and their form was affected. The *Ehrlich-Schwoebel* barrier prevented diffusion across step edges but diffusion along the step edge was significantly faster.

The diffusion zone of each nanoparticle in figure 4.30 was analyzed. An equivalent sphere would have had an average diameter $\overline{d}_{\mathrm{equiv.}} = (7.1\pm0.4)\,\mathrm{nm}$. This would put the size at the lower end of the height distribution before annealing (see figure 4.32(c), blue). The loss of material was mostly likely due to diffusion to adjacent step edges. A further analysis revealed some additional details: Nanoparticles of $h_{\mathrm{app.}} \gtrapprox 3.5\,\mathrm{nm}$ had a round top, similar to nanoparticles before annealing. Smaller nanoparticles of $h_{\mathrm{app.}} \lessapprox 3.5\,\mathrm{nm}$ had a flat top surface (figure 4.30(b)).

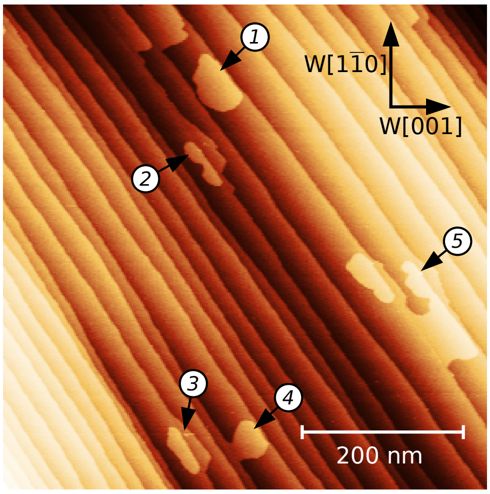

Figure 4.31: STM image of $Ni_{0.25}Fe$ nanoparticles on W(110) after annealing for 15 minutes at up to $580\,\mathrm{K}$: Molten nanoparticles have turned into compact islands. Crystallographic and morphological anisotropy influence the diffusion depending on the nanoparticles' position. Islands *2*, *3*, and *5* have each a remainder that is higher than one monolayer. W-Tip; $1.0\,\mathrm{V}$; $0.8\,\mathrm{nA}$

Annealing at $580\,\mathrm{K}$ resulted in the complete melting of all nanoparticles. Figure 4.31 shows the compact islands that were remaining. These islands were one monolayer high. Nanoparticles located close to terrace steps had spread on both terraces. Some islands, preferably those close to terrace steps (e.g. *2*, *3*, *5*), had a small peak in its center. This was a remainder of the original nanoparticles and it was not observed at $658\,\mathrm{K}$ or higher. The nanoparticles *1* to *4* were analyzed concerning their area. Their equivalent diameter was $\overline{d}_{\mathrm{equiv.}} = (8.9\pm0.7)\,\mathrm{nm}$, which is similar to the apparent height before annealing (figure 4.32(b)). The narrow terraces had been suppressing the diffusion and this had limited the loss of material.

The higher temperatures (not shown) always resulted in compact islands. Diffusion increased at rising temperatures.

Figure 4.32 shows the height distribution before and after deposition. Deflection voltages of 700, 750, and $850\,\mathrm{V}$ resulted in nanoparticles of approximately the same height of $9\,\mathrm{nm}$. A temperature of less than $550\,\mathrm{K}$ was sufficient to start the melting process. This caused the unrolling carpet effect and in turn a reduction in height. The

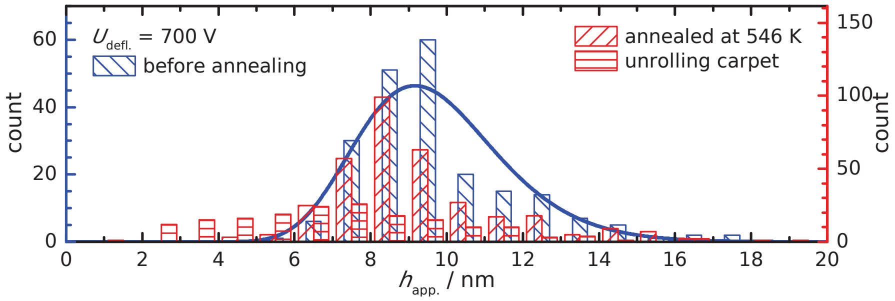

(a) Before annealing: $\overline{h}_{\text{app.}} = (9.5 \pm 1.2)$ nm. After annealing: Particle density remained constant. 34 % of the particles showed an unrolling carpet effect.

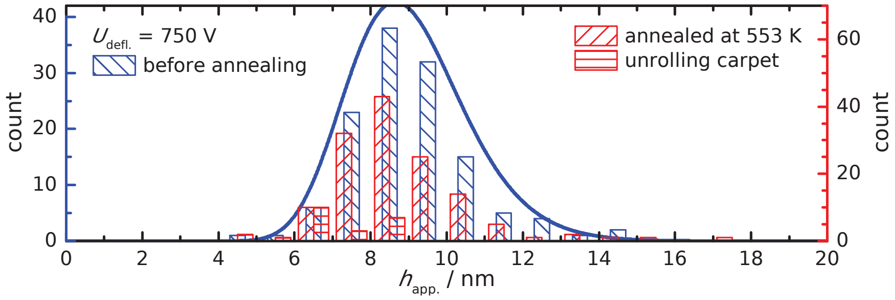

(b) Before annealing: $\overline{h}_{\text{app.}} = (8.9 \pm 1.2)$ nm. After annealing: Particle density reduced by 26 %. Slight height reduction. 15 % of the particles showed an unrolling carpet effect.

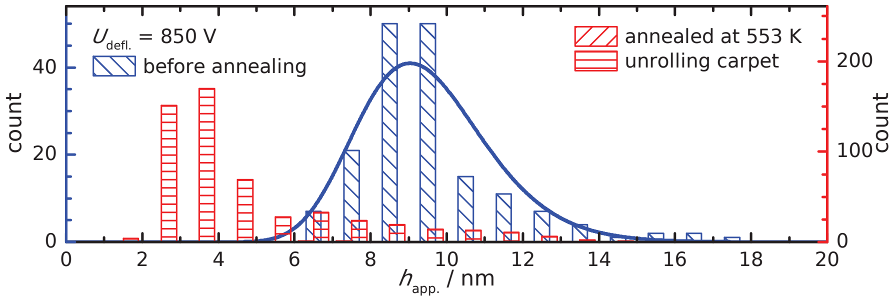

(c) Before annealing: $\overline{h}_{\text{app.}} = (9.3 \pm 1.2)$ nm. After annealing: Particle density reduced by 34 %. More than 99 % of the particles showed an unrolling carpet effect. (See figure 4.30)

Figure 4.32: Height distribution of $Ni_{0.25}Fe$ nanoparticles on W(110). Heights were log-normally distributed before annealing.

last sample (figure 4.32(c)) revealed a high amount of particles in the regime of 2 to $4\,\mathrm{nm}$. The area density after annealing had been reduced by one third. This strongly suggests, even though the STM did not reveal any monolayer islands, that the 2-to-4-nm-regime is not stable but simply an intermediary step before the complete meltdown.

It should be noted that the differentiation between particles with and without diffusion zone is difficult because the convolution of tip and sample is making it impossible to map the vicinity of a nanoparticle. For the purpose of this work, nanoparticles were classified as "unrolling carpet" when the diffusion zone was visible in STM, i.e. when it extended out of the area of uncertainty.

The particle size, i.e. the mass, before annealing did not dependent linearly on the deflection voltage. The wide distribution in figure 4.26 is a testimony to this. The effect was observed before [71, 90]. The linearity of mass versus deflection voltage holds true when exceeding a certain threshold. It is however interesting to see, that the larger nanoparticles were melting slightly earlier than the smaller ones.

4.4 Nickel-cobalt nanoparticles on W(110)/O-p(2×1)

Composition of raw material: The nanoparticles were produced in the magnetron sputtering source. The sputtering target from *MaTecK* had a composition of $50\,\%_{\mathrm{at}}$ Ni and $50\,\%_{\mathrm{at}}$ Co with an overall purity of $99.9\,\%$.

Sample preparation

The surface was prepared as outlined in section 4.2.4 by introducing air into the connecting tube between source and preparation chamber during deposition. The nanoparticles were deposited on a W(110) substrate. Three depositions with different settings of the quadrupole mass filter were done: A particle diameter $d_{\mathrm{QMF}} = 3.8\,\mathrm{nm}$ at a resolution of $\Delta m/m = 30\,\%$, $d_{\mathrm{QMF}} = 5.4\,\mathrm{nm}$ at $\Delta m/m = 10\,\%$, and $d_{\mathrm{QMF}} = 5.4\,\mathrm{nm}$ at $\Delta m/m = 100\,\%$. The two batches of $5.4\,\mathrm{nm}$ large nanoparticles were deposited on the same substrate: The nanoparticles with a resolution of $\Delta m/m = 10\,\%$ were deposited on the lefthand side and the wider resolution $\Delta m/m = 100\,\%$ was deposited on the righthand side.

4.4.1 Results for smaller nanoparticles

The surface structure was verified by LEED after deposition and after every annealing step. The structure was p$(2{\times}1)$ each time.

The height distribution resulting from the first deposition is shown in figure 4.33(a) and has a bimodal form with maxima at approximately $h_{\mathrm{app.}} = 3.4\,\mathrm{nm}$ and $h_{\mathrm{app.}} = 4.8\,\mathrm{nm}$. The peak at the smaller size can be attributed to the filtered particles. The larger sizes could be a result of non-perfect separation between neutral and charged particles but the well-defined peak suggests, that these nanoparticles were charged and that they were passing the quadrupole mass filter due to their higher mass (see also section 3.6).

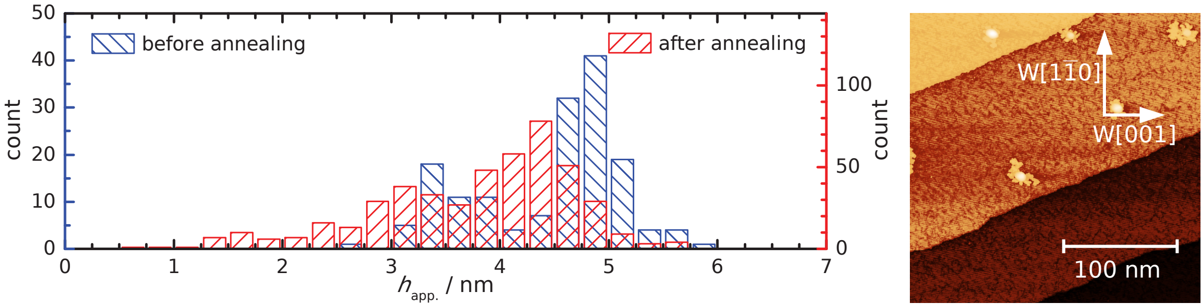

(a) ordinates are scaled in accordance with examined surface area

(b) W-Tip; 1.0 V; 0.8 nA

Figure 4.33: NiCo nanoparticles on tungsten oxide. Height distribution before and after annealing. STM image was taken after annealing and reveals ramified diffusion zones around nanoparticles as a result of unrolling carpet behavior.

Tempering

Figure 4.33(b) shows the surface after a short annealing for 15 minutes on the resistive heater (0.80 A / 3.12 W). The temperature was below 523 K for the entire time. A precise temperature cannot be given because the response of the thermocouples is too slow at this low power and the temperature is below the threshold of the pyrometer. The nanoparticles exhibited unrolling carpet behavior. The resulting diffusion zone had a ramified shape. This is similar to the results that were obtained from Co nanoparticles (see section 4.2.4)

The particle density was $58\,\mu\mathrm{m}^{-2}$ before annealing and $60\,\mu\mathrm{m}^{-2}$ after. This means, that a complete melting or complete evaporation of nanoparticles can be excluded. Both maxima of the distribution (see figure 4.33(a)) show a broadening shift towards smaller sizes. This suggests, that the temperature for surface melting (in this size regime) was independent of the size.

The coverage was far too low to determine possible growth-modes by LEED.

4.4.2 Results for larger nanoparticles

The nanoparticles of these two samples had a log-normal height distribution (see upper panel in figure 4.34(a)) with a mean of $h_{\mathrm{app.}} = (5.4\pm1.1)\,\mathrm{nm}$ and $h_{\mathrm{app.}} = (5.8\pm1.1)\,\mathrm{nm}$ respectively. I.e. the average height increased when the resolution widened. This is in agreement with the characteristics of quadrupole mass filters as outlined in section 3.6.4.

Tempering

The same heating power as for the smaller nanoparticles was used for the first tempering step. The temperature of the substrate was below the detection threshold of the pyrometer which means that a precise temperature reading is not available. The resulting height distributions are shown in the central panel of figure 4.34(a) and were similar to the previous distribution as far as the shifting towards smaller sizes was concerned. A segregation of smaller and larger nanoparticles had occurred, i.e. a bimodal distribution had formed. The area density of nanoparticles was the same before and after

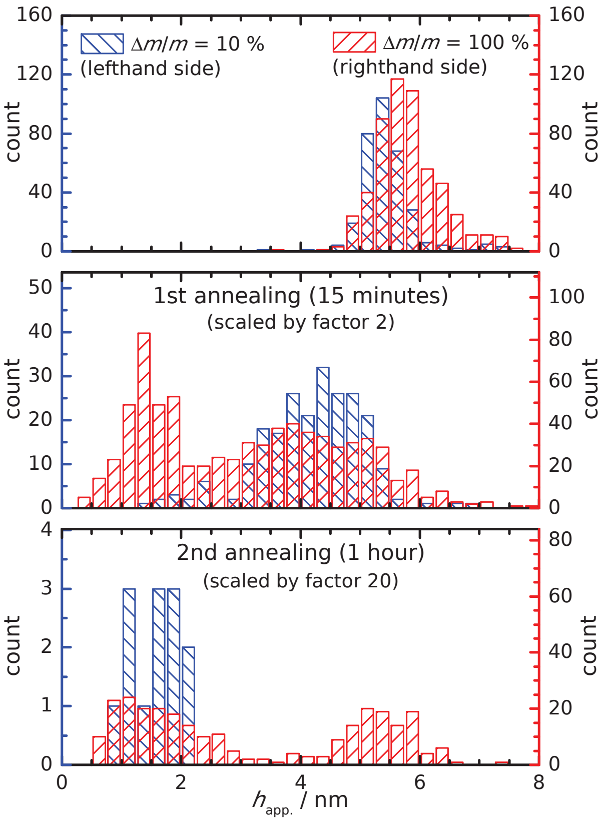

(a) Ordinates are scaled by the factor 2 (center) and 20 (bottom) with respect to the examined area.

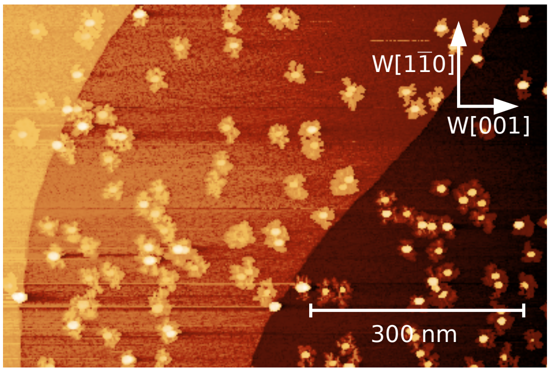

(b) Righthand side (filter at $100\,\%$) after 1$^{\text{st}}$ annealing step. W-Tip; $1.0\,\text{V}$; $0.8\,\text{nA}$

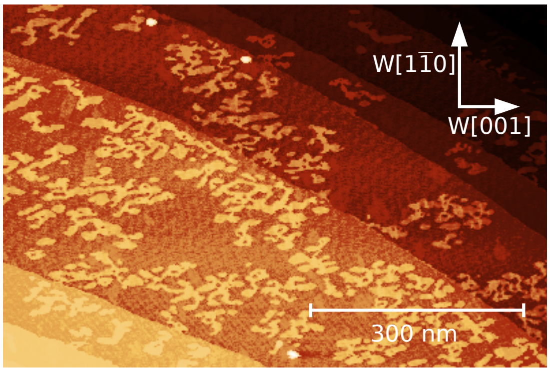

(c) Righthand side (filter at $100\,\%$) after 2$^{\text{nd}}$ annealing step. W-Tip; $1.0\,\text{V}$; $0.8\,\text{nA}$

Figure 4.34: Larger NiCo nanoparticles on tungsten oxide. The histogram shows a shift towards smaller sizes as a result of the annealing. Some large nanoparticles are remaining after annealing. The two annealing steps facilitate a transformation from individual nanoparticles over individual monolayer islands (b) to spread-out, meandering islands (c).

tempering. Most nanoparticles displayed a surrounding diffusion layer as a result of unrolling carpet behavior (figure 4.34(b)). This diffusion layer had a ramified shape.

The second tempering step was done with the same heating current but for one hour instead of 15 minutes. The pyrometer reported a maximum temperature of $543\,\text{K}$. LEED was used to monitor the sample surface throughout the heating process and no change in the diffraction pattern occurred.

The STM measurement after cool-down revealed a small number of remaining nanoparticles. The apparent height on the lefthand side (figure 4.34(a), lower panel) was between 0.8 and $2.0\,\text{nm}$ and the area density was reduced 13-fold. The area density was reduced 20-fold on the righthand side. The separation in a group of small nanoparticles ($h_{\text{app.}} < 3\,\text{nm}$) and a group of large nanoparticles ($h_{\text{app.}} > 5\,\text{nm}$) had increased. A closer look at the respective STM images revealed that the remaining large particles were not surrounded by a diffusion layer. This indicates that these particles had an increased melting point.

Islands with one monolayer height were spread over the surface. They featured rugged and highly irregular shapes (see figure 4.34(c)).

Particles smaller than $3\,\mathrm{nm}$ were probably not stable, but simple represented the last stage before the transition to a monolayer-only form.

4.5 Discussion

Table 4.2 gives an overview of the melting of the nanoparticles. The unrolling carpet effect was observed for all materials on all surfaces except on W(110)/O-((1×1)×12). Co exhibited a slightly lower melting temperature than the other materials but the overall differences were small.

<table>
<tr><th>material</th><th>substrate</th><th>temperature</th><th>form</th></tr>
<tr><td>Co, NiFe</td><td>W(110)</td><td>$T_{\mathrm{Ni}_{0.50}\mathrm{Fe}} < 520\,\mathrm{K}$
$T_{\mathrm{Co}} < 530\,\mathrm{K}$
$T_{\mathrm{Ni}_{0.25}\mathrm{Fe}} < 550\,\mathrm{K}$</td><td>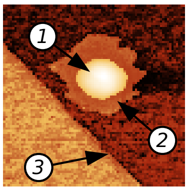 </td></tr>
<tr><td colspan="4"><i>1</i> nanoparticle with reduced height, <i>2</i> monolayer diffusion zone with one or more notches in W[001] direction, <i>3</i> agglomeration of material at nearby step edges.</td></tr>
<tr><td>Co</td><td>W(110)/C-R(15×3)</td><td>$T \approx 550\,\mathrm{K}$</td><td>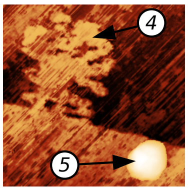 </td></tr>
<tr><td colspan="4"><i>4</i> monolayer diffusion zone with ramified shape, <i>5</i> remaining, intact nanoparticle. (Diagonal stripes are an artifact from scanning).</td></tr>
<tr><td>Co, NiCo</td><td>W(110)/O-p(2×1)</td><td>$T_{\mathrm{Ni}_{0.50}\mathrm{Co}} < 520\,\mathrm{K}$
$T_{\mathrm{Co}} < 550\,\mathrm{K}$</td><td>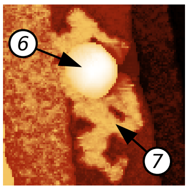 </td></tr>
<tr><td colspan="4"><i>6</i> nanoparticle with reduced height, <i>7</i> ramified monolayer diffusion zone, (Co forms hexagonal, multilayer-high islands in areas of high-concentration.)</td></tr>
<tr><td>Co</td><td>W(110)/O-((1×1)×12)</td><td>$T_{\text{height reduction}} \approx 570\,\mathrm{K}$
$T_{\text{reconstruction}} \approx 1060\,\mathrm{K}$</td><td>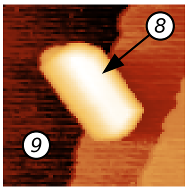 </td></tr>
<tr><td colspan="4"><i>8</i> nanoparticle with reduced height and elongated parallel to $\mathrm{W}\langle 1\bar{1}1\rangle$, <i>9</i> new surface reconstruction.</td></tr>
</table>

Table 4.2: Overview of the nanoparticles' melting behavior on different substrates. Direction of W[001]: →

4.5.1 Shape of the diffusion zone on W(110)

The influence of the substrate becomes obvious when comparing clean W(110) with W(110)/O-p(2×1). Unrolling carpet occurs in the same temperature range but the diffusion zone is different. It has a compact form on W(110), which indicates a high mobility of atoms on the surface and at the edges of the diffusion zones. Agglomeration of nanoparticle material at nearby tungsten step edges indicates a high surface mobility, too. Interlayer diffusion can be excluded. The diffusion zone's edges on W(110) are roughly parallel to W$\langle 1\bar{1}2\rangle$. The reason for this orientation is not immediately obvious because the most stable edges are expected to be along W$\langle 1\bar{1}1\rangle$ for pseudomorphic growth (see figure 4.35(a) and section 2.4.1 for details). The hexagonal shape is not in agreement with the measurements.

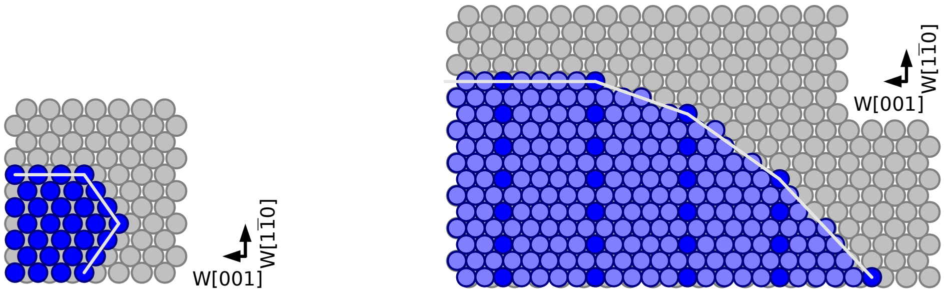

(a) Pseudomorphic growth: (Almost) hexagonal islands.

(b) Nishiyama-Wassermann reconstruction: Different, low-index island edges.

Figure 4.35: Orientation of edges: Hard sphere model of Co(0001) on W(110). ○ W atom, ● Co atom at a center position, ◉ Co atom at an incommensurable site.

An alternative explanation is based on the Nishiyama-Wassermann reconstruction which was observed for high-coverage Co on W(110) (e.g. Ociepa et al. [58]). Figure 4.35(b) shows this reconstruction and possible edges of an island. These edges have low-indices, i.e. the edges are formed from the connections of more stable, center-position atoms. In reality, one must assume that the atoms close to the edge are not positioned as highlighted but further relaxation is expected. Nevertheless, this is a good model to explain the edges' directions.

The termination in W[001]-direction requires a more complex explanation. Given the reconstruction in figure 4.35(b), one might expect that an edge in W[1$\bar{1}$0] direction would be particularly stable because it can be easily created by connecting center positions (figure 4.36(a)). To understand this discrepancy, one must understand that the mechanism of edge formation is based on a vastly simplified model. The Co top-layer is strained as a result of the lattice misfit. The strain is just 0.7 % parallel to W[001] but it is 2.7 % parallel to W[1$\bar{1}$0]. A reconstruction of the edge, as shown in figure 4.36(b), reduces the stress by introducing a ragged edge.

The general form is similar to the shape reported by Köhler et al. for Fe/W(110) [57] at similar temperatures. Elongation along the substrate's step edges at high temperatures is in perfect agreement with the results of Reuter et al. [62].

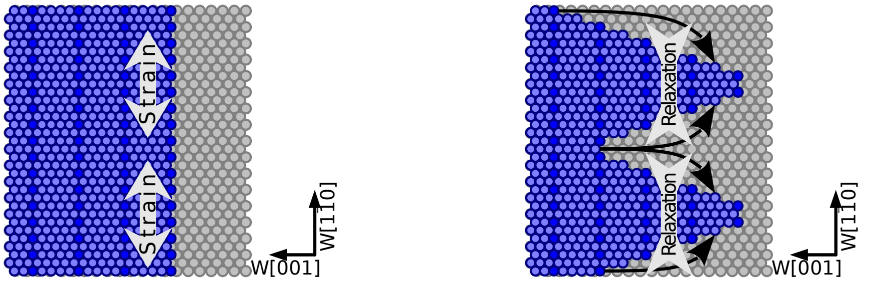

(a) Straight edges induce strain in the thin film.

(b) Reconstruction is leading to cogged edges with reduced strain.

Figure 4.36: Formation of cogged edges: Hard sphere model of the Nishiyama-Wassermann reconstruction of Co(0001) on W(110). ○ W atom, ● Co atom at a center position, ◉ Co atom at an incommensurable site.

4.5.2 The diffusion zone on other substrates

The diffusion zone on W(110)/O-p(2×1) has a ramified shape. This and a slightly higher melting temperature are both indicators of a reduced mobility on the substrate. A possible explanation is that the oxygen on the surface is chemically more active and thus forming bonds with the nanoparticles' atoms. This is similar to the *hit-and-stick* (see section 2.4.1) but with one difference: The atoms are moving on-top of the island/diffusion zone and they stick, when they reach the substrate after leaving the diffusion zone. That means, that the Ehrlich-Schwoebel barrier must be taken into account.

The effect on W(110)/C-R(15×3) is a continuation of this trend: A higher melting temperature is accompanied by an increased ramification. Measurements of Co films on this surface were done by Bettac et al. [121]. It was shown that Co film forms a rough fcc(001) layer as opposed to smooth hcp(0001) films on clean W(110).

The uneven melting is an additional effect: Some nanoparticles are melting while others remain unaffected from increasing temperatures. The difference between these two groups is not directly obvious but a number of typical differences between the nanoparticles could explain it. This includes differences in form/crystallization and differences in landing sites/substrate surface structure. Another, in my opinion more likely explanation, is a thermally induced phase transition. I.e. an initial energy is required to start the unrolling carpet.

On the one hand one could assume that the inhomogeneous distribution of these two groups may indicate a site dependence. But on the other hand, these areas of molten/unmolten nanoparticles are much wider than typical surface domains. Further investigations are necessary to solve this mystery.

Very high coverage (more than 1 ML after melting) results in the formation of yet another new surface. This was observed for Co nanoparticles which formed a closed Co(0001) surface after melting. The remaining Co nanoparticles took the form of hexagons.

A similar mechanism is present for Co nanoparticles on W(110)/O-((1×1)×12). An unrolling carpet does not occur but a new surface structure is forming at high temperatures. This is possibly a cobalt-oxide or Co-W-oxide compound. The remaining nanoparticles show a characteristically elongated form (see *8* in table 4.2) which indicates a strong influence of the surface.

4.5.3 Experimental differences between the nanoparticle sources

My results and those of my predecessors were obtained from two different nanoparticle sources. Our diverging results concerning the melting behavior could be resulting from these experimental differences.

Bulut used the ACIS but my cobalt measurements were done with the newly installed magnetron sputtering source. If this has an actual effect on the formation or contamination of the nanoparticles is still unclear. The operational pressure was an order of magnitude higher but it was, given the high purity of the inert gases, not sufficient to alter the substrate surface's composition. Extra-long depositions and deposition-like tests were conducted to rule out contamination from the deposition. A rather far-fetched theory may be that the inert gases were momentarily sticking to the substrate and thus softening the landing of the nanoparticles.

Influence of noble gas atoms on the nanoparticles

The bombardment of the nanoparticles with inert gas atoms was suggested as an explanation of the discrepancy between the results. The substrate at the magnetron sputtering source is exposed to a higher pressure compared to the substrate at the ACIS. The pressure is equivalent to an increased number of atoms hitting the substrate.

Ion bombardment (i.e. sputtering) has a significant influence on a surface (see section 3.6.1). However, sputtering works at high ion energies. To get an estimate of the kinetic energy in this situation, one can follow the path of an argon atom. The sputtering process will ionize and accelerate the atom. The impact at the sputtering target will certainly increase the temperature but the collisions in the subsequent aggregation process will cool the gas down to room temperature. The average velocity v_{rms} of an atom after thermalization can be calculated if one assumes a Maxwell-Boltzmann distribution:

$$\begin{aligned} v_{\text{rms}} &= \sqrt{\frac{3k_{\text{B}}T}{m}} \\ \Rightarrow v_{\text{rms}}(\text{He}) &= 1367\,\text{m}\cdot\text{s}^{-1} \\ \Rightarrow v_{\text{rms}}(\text{Ar}) &= 433\,\text{m}\cdot\text{s}^{-1} \end{aligned} \tag{4.5}$$

A similar (argon) velocity was reported by Kousal et al. [94], based on theoretical calculations and experimental measurements.

The kinetic energy E_{kin} can be calculated as well:

$$\begin{aligned} E_{\text{kin}} &= \frac{mv^2}{2} \\ \Rightarrow E_{\text{kin}} &= \frac{3k_{\text{B}}T}{2} = 38.8\,\text{meV} \end{aligned} \tag{4.6}$$

This energy can be checked against the bonding energy in a cobalt cluster. The cluster with the lowest energy is the Co_2 dimer with a bonding energy of $1.139\,\text{eV}$ [122]. Larger clusters (which includes the Co nanoparticles of this thesis) have higher bonding energies. This means, that the kinetic energy of an impinging atom is at least 30 times smaller than the lowest possible bonding energy. A gas atom may experience collisions before it reaches the substrate. These collisions will not increase the average kinetic energy because all beam-facing components are at room temperature. In fact, collisions are necessary because there is no clear line of sight between the aggregation region and the deposition substrate.

Influence of noble gas ions on the nanoparticles

It has been shown that the kinetic energy of noble gas ions is utterly insufficient to have any effect on the nanoparticles. However the calculation above does not include the ionization energy. The first ionization energies of helium and argon are $E_\text{I}(\text{He}^+) = 24.5874\,\text{eV}$ and $E_\text{I}(\text{Ar}^+) = 15.7596\,\text{eV}$. These values are significantly higher than the kinetic energy but still lower than the total kinetic energy of a nanoparticle $E_\text{kin}(\text{NP})$ at soft-landing conditions.

The Co nanoparticles in section 4.2.1 had a mass of approximately $10^6\,\text{amu}$:

$$\begin{aligned} E_\text{kin} &= \frac{mv^2}{2} = 635\,\text{eV} \\ &\mathrel{\hat{=}} 0.075\,\text{eV}{\cdot}\text{atom}^{-1} \end{aligned} \tag{4.7}$$

at an assumed velocity of $350\,\text{m}{\cdot}\text{s}^{-1}$ [94]. Therefore, the deposition of a nanoparticle is about 30 times more energetic than the energy of a noble gas ion.

However, this calculation is based on the idea that noble gas ions can reach the substrate at all. The magnetron sputtering source offers two possibilities two obtain ionized gases: On the one hand, collisions can occur between charged nanoparticles and neutral gas atoms but a charge transfer is very unlikely due to the higher ionization energy of the noble gases. On the other hand, an ion from the magnetron discharge could retain its charge and hit the substrate. However, this is similarly unlikely because that ion would be passing the quadrupole mass filter. The sole purpose of the QMF is the removal of ions of wrong masses. Therefore, most of the ions will loose their charge when they hit the quadrupole rods. The number of gas ions passing through the QMF can be estimated from the spectrum at the ion collector plate, too. A large, constant influx of positive ions would shift the spectra towards positive values. This is not reflected in the spectra that were obtained before the depositions (e.g. figure 3.15(a)).

One can assume from this that the current of ionized noble gas is below the detection limit of the ion collector but the current of nanoparticles is obviously well above the detection limit. Therefore, the number of argon/helium ions must be significantly lower than the number of charged nanoparticles. The chance that a nanoparticle on the substrate gets hit by one of these rare ions is completely negligible. Even if every single gas ion would find its way to a nanoparticle, the number of affected nanoparticles would still be small compared to the overall number of nanoparticles.

It should be mentioned that certain operational conditions lead to a constant, positive ion spectrum. I assume that these were situations of very high ionization in the magnetron. The quadrupole was either incapable of handling the current on the quadrupole rods or the space charge between the rods was reducing the filter's effectiveness. No successful deposition was achieved under these conditions.

5 Conclusion

An overview of the results was given in the final section of the previous chapter. This section is the conclusion to my thesis and some of the accomplishments will be emphasized. The focus is on the setup of the magnetron sputtering source and the continuation of the work concerning the anisotropic melting.

5.1 Magnetron sputtering source

The installation of the magnetron sputtering source was successful. A number of different setups were tested and I have shown that it is possible to produce nanoparticles in a range from $h_{\text{app.}} = 3.5\,\text{nm}$ upwards. The limiting factor for the upper size ($d \approx 10\,\text{nm}$) is not the source itself, but the quadrupole mass filter. Particles in the range of up to $h_{\text{app.}} \approx 15\,\text{nm}$ were produced but the lack of proper size-selection was a significant drawback.

Outlook

The magnetron sputtering source is currently fully operational and, given regular maintenance, will continue to be in the future. The upcoming addition of a five-axes-manipulator gives an additional degree of freedom for the deposition of nanoparticles. The independent setting of elevation angle and azimuth angle is going to allow the deposition of nanoparticles from every direction. A reduced elevation angle can open the field to a fine-grained control of the deposition energy. The reflection of nanoparticles on hard substrates is another experiment-to-be. The correct orientation of the manipulator may allow the specular reflection of size-selected nanoparticles towards a secondary substrate on the magnetic transporter.

It is possible to move the source into the other two UHV labs. Moving it to the *Hydrogen-Lab* would result in one STM per nanoparticle source. Moving the source to the *XPS/SPLEED-Lab* could give access to the eponymous spectral analysis tools.

Further improvements of the source are not necessary, although additional pumping stages are always helpful. The pumping stages should however be accompanied by ion-guides to reduce particle loss.

5.2 Anisotropic melting

The anisotropic melting (*15* in table 5.1 and section 2.5.2), as reported by Bulut [30] and Rosellen [67] for Co, could not be reproduced. A number of differences in experimental conditions may explain this.

<table>
<tr><th>material</th><th>substrate</th><th>temperature</th><th>form</th></tr>
<tr><td>Fe</td><td>W(110)</td><td>$T_{\text{height reduction}} = 600\,\text{K}$
$T_{\text{melting}} = 640\,\text{K}$</td><td>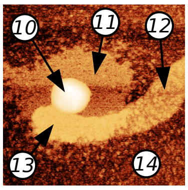
</td></tr>
<tr><td colspan="4">*10* nanoparticle with reduced height, *11* monolayer diffusion zone, slightly elongated in W[001] direction, *12* monolayer meandering diffusion zone, *13* double layer, *14* tiny islands / atoms around the diffusion zone. Published in [67], image from [123].</td></tr>
</table>

<table>
<tr><td>Fe, Co, FeCo</td><td>W(110)</td><td>$T_{\text{height reduction}} = 923\,\text{K}$
$T_{\text{melting}} = 1023\,\text{K}$</td><td>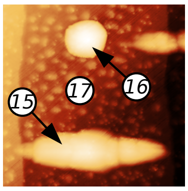
</td></tr>
<tr><td colspan="4">*15* elongated nanoparticle, *16* nanoparticle with reduced height, *17* tiny islands / atoms scattered across the surface. Published in [29, 30, 67], image from [124].</td></tr>
</table>

Table 5.1: Previous results of the nanoparticles' melting behavior on different substrates.

The W(110) crystal that was used in this thesis had been thoroughly cleaned and was virtually free of carbon contaminants. This is in strong contrast to the previously reported carbon contamination that occurred during the prolonged annealing [30, p. 76]. The influence of the carbon contamination on the melting of nanoparticles was discussed in section 4.2.2. I have shown that the W(110)/C-R(15×3) reconstruction was able to increase the melting point by several tens of Kelvins. This increase is still far away from the temperatures reported for anisotropic annealing.

Significant high-temperature stability was observed on W(110)/O-((1×1)×12) (see section 4.2.3). The Co nanoparticles exhibited a significant anisotropic spreading and a height of a few nanometers after annealing at 1000 K. The preferred orientation, parallel to $\mathrm{W}\langle 111\rangle$, is however at odds with the previously reported orientation and the completely new surface structure has not been reported yet.

The base pressure for deposition was not significantly different compared to Bulut's work [30, p. 80]. The possible influence of oxygen contamination has been thoroughly examined and yielded new, interesting results. Another sample was prepared and annealed immediately after deposition. This quick processing was intended to further reduce the contamination and it did not yield different results.

Outlook

A first step would be to reproduce the original measurements with the ACIS. The main obstacle at is the rather long manufacturing time for new cathodes which has recently increased from several month to more than a year. The old, existing Co cathodes are incompatible with the current setup.

The influence of the kinetic energy can be easily checked as soon as the new manipulator for the magnetron sputtering source is finished.

The very-soft landing of nanoparticles on inert gas layers is a well-known practice at low temperatures for a layer of frozen argon (e.g. [125]) but is unknown for a single monolayer adsorbate. This might be, if deemed useful, examined by inducing inert gas directly into the deposition chamber.

A Appendix

A.1 List of abbreviations

ACIS	Arc cluster ion source
AES	Auger electron spectroscopy
bcc	body-centered cubic
CNT	carbon nanotube
DFT	density functional theory
EDX	energy dispersive X-ray spectroscopy
fcc	face-centered cubic
hcp	hexagonal closed-packed
HOPG	highly-oriented pyrolytic graphite
HR-TEM	high-resolution TEM
IGP	ion getter pump
L	Langmuir (unit of exposure): $1\,\mathrm{L} = 1\,\mu\mathrm{Torr} \cdot 1\,\mathrm{s}$
LEED	ctron diffraction
MD	molecular dynamics
ML	monolayer
MOKE	magneto-optical Kerr effect
QMF	quadrupole mass filter
RHEED	reflection high-energy electron diffraction
SAM	scanning Auger microscopy
sccm	standard cubic centimeters per minute (unit of flow): $1\,\mathrm{sccm} = 1\,\mathrm{cm}^3 \cdot \mathrm{min}^{-1}$ at standard conditions ($T = 273\,\mathrm{K}$, $p = 1.01 \cdot 10^5\,\mathrm{Pa}$)
SEM	scanning electron microscope / scanning electron microscopy
SP-STM	spin-polarized STM
STM	scanning tunneling microscope / scanning tunneling microscopy
SW-CNT	single-wall carbon nanotube
TEM	transmission electron microscope / transmission electron microscopy
TSP	titanium sublimation pump
UHV	ultra-high vacuum
XAS	X-ray absorption spectroscopy
XMCD	X-ray magnetic circular dichroism
μ_B	Bohr magneton: $\mu_\mathrm{B} = \frac{e\hbar}{2m_\mathrm{e}}$

Table A.1: List of abbreviations

A.2 Nomenclature of alloy composition

The composition of alloys and alloy nanoparticles is not always clear. A value like $Ni_{25}Fe_{75}$ may designate an alloy of $25\,\%$ Ni and $75\,\%$ Fe but it may also designate a cluster of 25 Ni atoms and 75 Fe atoms. Additional ambiguity is created as percentage may be given with respect to the total mass ($\%_{\mathrm{weight}}$) or with respect to the number of atoms ($\%_{\mathrm{at.}}$).

The following nomenclature was used in this work:

- Integer values represent the total number of atoms. e.g. $Ni_{25}Fe_{75}$ designates a particle of 25 Ni atoms and 75 Fe atoms.
- The atom count is not given, if it is equal to one. e.g. $Ni_{25}Fe$ designates a particle of 25 Ni atoms and 1 Fe atom.
- Fractional values below one represent fractional concentrations. e.g. $Ni_{0.25}Fe_{0.75}$ designates an alloy with a nickel concentration of $25\,\%_{\mathrm{at.}}$ and an iron concentration of $75\,\%_{\mathrm{at.}}$.
- If the concentration of a compound is not given, then its concentration accounts for the remaining amount. e.g. $Ni_{0.25}Fe$ designates an alloy of $25\,\%_{\mathrm{at.}}$ nickel. The remainder, i.e. $100\,\% - 25\,\% = 75\,\%$, is iron.

A.3 Scaling of ordinates in histograms

The number of nanoparticles n_{NP} that can be examined by STM depends on two factors: The number of scanned images and the number of particles per image.

From this follows:

$$n_{\mathrm{NP}} = A_{\mathrm{STM}} \cdot \rho_{\mathrm{NP}} \tag{A.1}$$

where ρ_{NP} is the average area density of nanoparticles and A_{STM} is the total area of the scanning. The former is an intrinsic property of the sample while the latter is independent of the sample.

A histogram of the height distribution is therefore a result of both factors, but A_{STM} carries no information about the sample. This complicated the comparison of histograms which are based on n_{NP}. One option is to use the normalized particle count $\frac{n_{\mathrm{NP}}}{A_{\mathrm{STM}}}$. This has the advantage that two histograms (e.g. taken before and after annealing) will reveal a shift in height and a change of the total number of the particles. The disadvantages are that the total number of particles is lost – a number that carries statistical significance – and that the data-evaluation is greatly complicated.

My approach is using each histogram its own ordinate (y-axis). This is accomplished by by either having one ordinate on the left and one on the right side of the diagram or by stacking diagrams vertically. This method reveals the changes in particle height and total count.

A.4 Temperature reference sheet

I/A	T/°C	T/K
0.1	86.717	359.717
0.2	114.746	387.746
0.3	142.775	415.775
0.4	170.804	443.804
0.5	198.833	471.833
0.6	226.862	499.862
0.7	254.891	527.891
0.8	282.92	555.92
0.9	310.949	583.949
1.0	338.978	611.978
1.1	367.007	640.007
1.2	395.036	668.036
1.3	423.065	696.065
1.4	451.094	724.094
1.5	479.123	752.123
1.6	507.152	780.152
1.7	535.181	808.181
1.8	563.21	836.21
1.9	591.239	864.239
2.0	619.268	892.268
2.1	647.297	920.297
2.2	675.326	948.326
2.3	703.355	976.355
2.4	731.384	1004.384
2.5	759.413	1032.413
2.6	787.442	1060.442
2.7	815.471	1088.471
2.8	843.5	1116.5
2.9	871.529	1144.529
3.0	899.558	1172.558
3.1	927.587	1200.587
3.2	955.616	1228.616
3.3	983.645	1256.645
3.4	1011.674	1284.674
3.5	1039.703	1312.703
3.6	1067.732	1340.732
3.7	1095.761	1368.761
3.8	1123.79	1396.79
3.9	1151.819	1424.819
4.0	1179.848	1452.848
4.1	1207.877	1480.877
4.2	1235.906	1508.906
4.3	1263.935	1536.935
4.4	1291.964	1564.964

Table A.2: Reference table for manipulator temperature and required heating current.

Bibliography

[1] K. Oura, V.G. Lifshits, A.A. Saranin, A.V. Zotov, and M. Katayama. *Surface Science - An Introduction*. Springer, 2003.

[2] K.L. Kelly, E. Coronado, L.L. Zhao, and G.C. Schatz. The optical properties of metal nanoparticles: The influence of size, shape, and dielectric environment. *The Journal of Physical Chemistry B*, 107(3):668–677, 2003.

[3] P.O. Anikeeva, J.E. Halpert, M.G. Bawendi, and V. Bulović. Quantum Dot Light-Emitting Devices with Electroluminescence Tunable over the Entire Visible Spectrum. *Nano Letters*, 9(7):2532–2536, June 2009.

[4] M. Getzlaff. *Fundamentals of Magnetism*. Springer, 2008.

[5] M. Bode, O. Pietzsch, A. Kubetzka, and R. Wiesendanger. Shape-dependent thermal switching behavior of superparamagnetic nanoislands. *Physical Review Letters*, 92:067201, February 2004.

[6] P. Gambardella, S. Rusponi, M. Veronese, S.S. Dhesi, C. Grazioli, A. Dallmeyer, I. Cabria, R. Zeller, P.H. Dederichs, K. Kern, C. Carbone, and H. Brune. Giant magnetic anisotropy of single cobalt atoms and nanoparticles. *Science*, 300(5622):1130–1133, 2003.

[7] I.M.L. Billas, J.A. Becker, A. Châtelain, and W.A. de Heer. Magnetic moments of iron clusters with 25 to 700 atoms and their dependence on temperature. *Physical Review Letters*, 71:4067–4070, December 1993.

[8] I.M.L. Billas, A. Châtelain, and W.A. de Heer. Magnetism from the atom to the bulk in iron, cobalt, and nickel clusters. *Science*, 265(5179):1682–1684, 1994.

[9] J. Bansmann, S.H. Baker, C. Binns, J.A. Blackman, J.-P. Bucher, J. Dorantes-Dávila, V. Dupuis, L. Favre, D. Kechrakos, A. Kleibert, K.-H. Meiwes-Broer, G.M. Pastor, A. Perez, O. Toulemonde, K.N. Trohidou, J. Tuaillon, and Y. Xie. Magnetic and structural properties of isolated and assembled clusters. *Surface Science Reports*, 56(6):189–275, 2005.

[10] K.W. Edmonds, C. Binns, S.H. Baker, M.J. Maher, S.C. Thornton, O. Tjernberg, and N.B. Brookes. Size dependence of the magnetic moments of exposed nanoscale iron particles. *Journal of Magnetism and Magnetic Materials*, 231(1):113–119, 2001.

[11] J. Bansmann and A. Kleibert. Magnetism of mass-filtered nanoparticles on ferromagnetic supports. *Applied Physics A*, 80(5):957–964, February 2005.

[12] G. Wulff. Zur Frage der Geschwindigkeit des Wachsthums der Auflösung der Krystallflächen. *Zeitschrift für Krystallographie und Mineralogie*, 34:449–530, March 1901.

[13] C.R. Henry. Morphology of supported nanoparticles. *Progress in Surface Science*, 80(3):92–116, 2005.

[14] F. Baletto, R. Ferrando, A. Fortunelli, F. Montalenti, and C. Mottet. Crossover among structural motifs in transition and noble-metal clusters. *The Journal of Chemical Physics*, 116(9):3856–3863, 2002.

[15] I. Barke, H. Hartmann, D. Rupp, L. Flückiger, M. Sauppe, M. Adolph, S. Schorb, Ch. Bostedt, R. Treusch, Ch. Peltz, S. Bartling, T. Fennel, K.-H. Meiwes-Broer, and T. Möller. The 3d-architecture of individual free silver nanoparticles captured by x-ray scattering. *Nature Communications*, 6, February 2015.

[16] E.K. Parks, K.P. Kerns, and S.J. Riley. The structure of nickel–iron clusters probed by adsorption of molecular nitrogen. *Chemical Physics*, 262(1):151–167, December 2000.

[17] O. Margeat, D. Ciuculescu, P. Lecante, M. Respaud, C. Amiens, and B. Chaudret. NiFe Nanoparticles: A Soft Magnetic Material? *Small*, 3(3):451–458, February 2007.

[18] J. Teeriniemi, M. Melander, S. Lipasti, R. Hatz, and K. Laasonen. Fe–Ni Nanoparticles: A Multiscale First-Principles Study to Predict Geometry, Structure, and Catalytic Activity. *The Journal of Physical Chemistry C*, 121(3):1667–1674, December 2017.

[19] W.-H. Chiang and R.M. Sankaran. Linking catalyst composition to chirality distributions of as-grown single-walled carbon nanotubes by tuning $\mathrm{Ni}_x\mathrm{Fe}_{1-x}$ nanoparticles. *Nature materials*, 8(11):882–886, November 2009.

[20] S.K. Singh, A.K. Singh, K. Aranishi, and Q. Xu. Noble-Metal-Free Bimetallic Nanoparticle-Catalyzed Selective Hydrogen Generation from Hydrous Hydrazine for Chemical Hydrogen Storage. *Journal of the American Chemical Society*, 133(49):19638–19641, November 2011. PMID: 22070579.

[21] M.P. Andersson, F. Abild-Pedersen, I.N. Remediakis, T. Bligaard, G. Jones, J. Engbæk, O. Lytken, S. Horch, J.H. Nielsen, J. Sehested, J.R. Rostrup-Nielsen, J.K. Nørskov, and I. Chorkendorff. Structure sensitivity of the methanation reaction: H2-induced CO dissociation on nickel surfaces. *Journal of Catalysis*, 255(1):6–19, April 2008.

[22] D. Upper. The unsuccessful self-treatment of a case of "writer's block". *Journal of Applied Behavior Analysis*, 7(3):497–497, 1974.

[23] R. Pöttgen and D. Johrendt. *Intermetallics*. de Gruyter, 2014.

[24] F.M. Takrori and A. Ayyad. Surface energy of metal alloy nanoparticles. *Applied Surface Science*, 401:65–68, 2017.

[25] M. Masoumi, L.P.M. Santos, I.N. Bastos, S.S.M. Tavares, M.J.G. da Silva, and H.F.G. de Abreu. Texture and grain boundary study in high strength Fe–18Ni–Co steel related to hydrogen embrittlement. *Materials & Design*, 91:90–97, 2016.

[26] W. Pepperhoff and M. Acet. *Constitution and Magnetism of Iron and its Alloys*. Springer Science & Business Media, 2001.

[27] Y.-Y. Chuang, K.-Ch. Hsieh, and Y.A. Chang. A thermodynamic analysis of the phase equilibria of the Fe-Ni system above 1200 K. *Metallurgical Transactions A*, 17(8):1373–1380, August 1986.

[28] W.B. Pearson. *A handbook of lattice spacings and structures of metals and alloys*. Pergamon Pr., New York, 1958.

[29] F. Bulut, W. Rosellen, and M. Getzlaff. Structural properties of size-selected FeCo nanoparticles deposited on W(110). *Applied Physics A*, 97(1):185–189, April 2009.

[30] F. Bulut. *Massenselektierte Eisen-Kobalt-Legierungscluster - Korrelation magnetischer und struktureller Eigenschaften*. Inauguraldissertation, Heinrich-Heine-Universität Düsseldorf, Institut für Angewandte Physik, 2008.

[31] M.F. Collins and D.A. Wheeler. Magnetic moments and the degree of order in cobalt-nickel alloys. *Proceedings of the Physical Society*, 82(4):633, 1963.

[32] P.S.P. Wei. Low-energy electron diffraction study of tungsten (100) surface. *The Journal of Chemical Physics*, 53(7):2939–2945, October 1970.

[33] J. Kołaczkiewicz and E. Bauer. Growth and thermal stability of Fe, Ni, Rh and Pd layers on the (111)W crystal face. *Surface Science*, 420(2-3):157–173, January 1999.

[34] A. Winkelmann, D. Hartung, H. Engelhard, C.-T. Chiang, and J. Kirschner. High efficiency electron spin polarization analyzer based on exchange scattering at Fe/W(001). *Review of Scientific Instruments*, 79(8):083303, August 2008.

[35] L. Vitos, A.V. Ruban, H.L. Skriver, and J. Kollár. The surface energy of metals. *Surface Science*, 411(1-2):186–202, August 1998.

[36] R. M. Stern. Tungsten (110) surface characteristics in Low-Energy Electron diffraction. *Applied Physics Letters*, 5(11):218, 1964.

[37] R. Baudoing and R.M. Stern. Metastable surface structure of the W(110) face. *Surface Science*, 10(3):392–398, June 1968.

[38] E. Bauer. Multiple scattering versus superstructures in low energy electron diffraction. *Surface Science*, 7(3):351–364, July 1967.

[39] D.F. Ollis and M. Boudart. Surface and bulk carburization of tungsten single crystals. *Surface Science*, 23(2):320–346, November–December 1970.

[40] K.J. Rawlings, S.D. Foulias, and B.J. Hopkins. A model for carburised W(100) and W(110). *Journal of Physics C: Solid State Physics*, 14(34):5411–5415, 1981.

[41] J.G. Macmillan, A.J. Slavin, and K.J. Sunderland. The adsorption kinetics of C2H2, and C2H4 on W(110) at 1100 K. *Surface Science*, 173(1):138–147, August 1986.

[42] M. Bode, R. Pascal, and R. Wiesendanger. STM study of carbon-induced reconstructions on W(110): strong evidence for a surface lattice deformation. *Surface Science*, 344(3):185–191, December 1995.

[43] L.H. Germer and J.W. May. Diffraction study of oxygen adsorption on a (110) tungsten face. *Surface Science*, 4(4):452–470, July 1966.

[44] J.W. May. Coadsorption of oxygen and carbon monoxide upon a (110) tungsten surface. *The Journal of Chemical Physics*, 45(7):2383, October 1966.

[45] T. Engel, H. Niehus, and E. Bauer. Adsorption of oxygen on W(110). *Surface Science*, 52(2):237–262, October 1975.

[46] P.K. Wu, M.C. Tringides, and M.G. Lagally. Ordering kinetics of a chemisorbed overlayer: O/W(110). *Physical Review B*, 39(11):7595–7610, April 1989.

[47] K.E. Johnson, R.J. Wilson, and S. Chiang. Effects of adsorption site and surface stress on ordered structures of oxygen adsorbed on W(110). *Physical Review Letters*, 71(7):1055–1058, August 1993.

[48] K. Radican, S.I. Bozhko, Sundar-Raja Vadapoo, S. Ulucan, Han-Chun Wu, A. McCoy, and I.V. Shvets. Oxidation of W(110) studied by LEED and STM. *Surface Science*, 604(19-20):1548–1551, September 2010.

[49] E. Bauer and T. Engel. Adsorption of oxygen on W(110). *Surface Science*, 71(3):695–718, February 1978.

[50] H. Daimon, R. Ynzunza, J. Palomares, H. Takabi, and Ch.S. Fadley. Direct structure analysis of W(110)-(1×1)-O by full solid-angle x-ray photoelectron diffraction with chemical-state resolution. *Surface Science*, 408(1-3):260–267, June 1998.

[51] R.X. Ynzunza, F.J. Palomares, E.D. Tober, Z. Wang, J. Morais, R. Denecke, H. Daimon, Y. Chen, Z. Hussain, M.A. Van Hove, and C.S. Fadley. Structure determination for saturated (1×1) oxygen on W(110) from full solid angle photoelectron diffraction with chemical-state resolution. *Surface Science*, 442(1):27–35, November 1999.

[52] W. Rosellen, Ch. Kleinhans, V. Hückelkamp, F. Bulut, A. Kleibert, J. Bansmann, and M. Getzlaff. Influence of substrate and temperature on the shape of deposited Fe, Co, and FeCo nanoparticles. *physica status solidi (b)*, 247(5):1032–1038, May 2010.

[53] W. Rosellen, H. Bettermann, T. Veltum, and M. Getzlaff. Low energy impact of size selected FeCo nanoparticles with a W(110) surface. *Physica E*, 44(7-8):1683–1686, April 2012.

[54] H. Bettermann, M. Werner, and M. Getzlaff. Temperature-induced processes for size-selected metallic nanoparticles on surfaces. *Applied Surface Science*, 391:49–52, January 2017.

[55] J. Bansmann, A. Kleibert, H. Bettermann, and M. Getzlaff. In-flight and postdeposition manipulation of mass-filtered nanoparticles under soft-landing conditions. In *Gas-Phase Synthesis of Nanoparticles*, pages 323–338. Wiley-VCH Verlag GmbH & Co. KGaA, March 2017.

[56] H.N. Pham. Größenabhängige Mobilität metallischer Nanopartikel auf Graphen. Bachelorarbeit, Heinrich-Heine-Universität Düsseldorf, Institut für Angewandte Physik, March 2016.

[57] U. Köhler, C. Jensen, C. Wolf, A.C. Schindler, L. Brendel, and D.E. Wolf. Investigation of homoepitaxial growth on bcc surfaces with STM and kinetic Monte Carlo simulation. *Surface Science*, 454-456:676–680, May 2000.

[58] J.G. Ociepa, P.J. Schultz, K. Griffiths, and P.R. Norton. Re-emitted positron energy spectroscopy from thin Co films on W(110). *Surface Science*, 225(3):281–291, January 1990.

[59] B.G. Johnson, P.J. Berlowitz, D.W. Goodman, and C.H. Bartholomew. The structural and chemisorptive properties of ultrathin cobalt overlayers on W(110) and W(100). *Surface Science*, 217(1):13–37, July 1989.

[60] H. Fritzsche, J. Kohlhepp, and U. Gradmann. Epitaxial strain and magnetic anisotropy in ultrathin Co films on W(110). *Physical Review B*, 51:15933–15941, June 1995.

[61] Ya.E. Geguzin, Yu.S. Kaganovskii, and E.G. Mikhailov. On the structural anisotropy of ^{63}Ni diffusion spread on the W surface. *Ukrainskii Fizicheskii Zhurnal*, 27:1865–1867, 1982.

[62] D. Reuter, G. Gerth, and J. Kirschner. Anisotropic diffusion of 3 d metals on W(110): Competition between crystalline structure and surface steps. *Physical Review B*, 57(4):2520–2529, January 1998.

[63] R. Butz and H. Wagner. Surface diffusion of Pd and Au on W single crystal planes. *Surface Science*, 87(1):69–84, August 1979.

[64] E. Bauer, H. Poppa, G. Todd, and F. Bonczek. Adsorption and condensation of Cu on W single-crystal surfaces. *Journal of Applied Physics*, 45(12):5164–5175, December 1974.

[65] A. Kleibert, A. Voitkans, and K.-H. Meiwes-Broer. Size-dependent alignment of Fe nanoparticles upon deposition onto W(110). *Physical Review B*, 81:073412, February 2010.

[66] H. Haberland, Z. Insepov, and M. Moseler. Molecular-dynamics simulation of thin-film growth by energetic cluster impact. *Physical Review B*, 51(16):11061–11067, April 1995.

[67] W. Rosellen. *Strukturelle Eigenschaften massenselektierter 3d-Metall-Partikel*. Inauguraldissertation, Heinrich-Heine-Universität Düsseldorf, Institut für Angewandte Physik, November 2013.

[68] F. Ding, K. Bolton, and A. Rosén. Molecular dynamics study of the surface melting of iron clusters. *The European Physical Journal D*, 34(1-3):275–277, July 2005.

[69] F. Bulut. Messdaten CD 1, sample, 31.1.2008.

[70] S. Helveg, C. López-Cartes, J. Sehested, P.L. Hansen, B.S. Clausen, J.R. Rostrup-Nielsen, F. Abild-Pedersen, and J.K. Nørskov. Atomic-scale imaging of carbon nanofibre growth. *Nature*, 427(6973):426–429, January 2004.

[71] M. Werner. NiFe - Nanopartikel auf Oberflächen. Masterarbeit, Heinrich-Heine-Universität Düsseldorf, Institut für Angewandte Physik, June 2015.

[72] K. Jousten, editor. *Wutz Handbuch Vakuumtechnik*. Springer, 11 edition, 2012.

[73] Omicron Nanotechnology. *SPECTALEED Optics and Electron Source*, 4.3 edition, October 2003.

[74] Omicron Nanotechnology. *Instruction Manual - UHV Evaporator EFM 3/4, Triple Evaporator EFM 3T, IBAD Evaporator EFM 3i*, 3.1 edition, February 2004.

[75] Omicron Vakuumphysik. *ISE 5 Sputter Ion Source User's Guide*, 1.1 edition, May 1999.

[76] VAT Vakuumventile. *Mini UHV Gate Valve - 2D dimension drawing*, 315370 edition, July 2014. 01032-CE01.

[77] *The Vacuum Technology Book - Volume II*, volume 2. Pfeiffer Vacuum GmbH, 2013.

[78] Arun Microelectronics Ltd. *Titanium sublimation pump controller model TSP2, user manual issue 3.2*, 2010.

[79] Vacuum Generators. *Operating and Maintenance Handbook, Resistive Heater Accessory, HST Series*, ecn2802 edition, 2002.

[80] C. Kleinhans. Magnetooptischer Kerr-Effekt - Charakterisierung größenselektierter Nanopartikel. Diplomarbeit, Heinrich-Heine-Universität Düsseldorf, Institut für Angewandte Physik, April 2010.

[81] M.P. Seah and W.A. Dench. Quantitative electron spectroscopy of surfaces: A standard data base for electron inelastic mean free paths in solids. *Surface and Interface Analysis*, 1(1):2–11, February 1979.

[82] Michel A. Van Hove, William H. Weinberg, and Chi-Ming Chan. *Low-Energy Electron Diffraction*. Springer Berlin Heidelberg, 1986.

[83] M. Bode, S. Krause, L. Berbil-Bautista, S. Heinze, and R. Wiesendanger. On the preparation and electronic properties of clean W(110) surfaces. *Surface Science*, 601(16):3308–3314, August 2007.

[84] G. Ganteför, H.R. Siekmann, H.O. Lutz, and K.-H. Meiwes-Broer. Pure metal and metal-doped rare-gas clusters grown in a pulsed arc cluster ion source. *Chemical Physics Letters*, 165(4):293–296, January 1990.

[85] R.-P. Methling, V. Senz, E.-D. Klinkenberg, Th. Diederich, J. Tiggesbäumker, G. Holzhüter, J. Bansmann, and K.-H. Meiwes-Broer. Magnetic studies on mass-selected iron particles. *The European Physical Journal D*, 16(1):173–176, October 2001.

[86] E.-D. Klinkenberg, K.-H. Meiwes-Broer, R.-P. Methling, and J. Tiggesbäumker. Verfahren und Vorrichtung zur kontinuierlichen Clusterproduktion mit Massenselektion. *Deutsches Patent- und Markenamt*, Patent-Nr. DE 101 35 434 A 1, February 2003.

[87] J. Passig. Charakterisierung und Optimierung der Nanoteilchenemission aus der Clusterquelle ACIS. Diplomarbeit, Universität Rostock, March 2005.

[88] VAT Vakuumventile. *UHV Gate Valve - 2D dimension drawing*, 212276 edition, May 2016. 10840-CE44.

[89] A Kleibert. *Massengefilterte Eisennanopartikel auf ultradünnen Kobaltfilmen - eine in situ Studie mit weicher Röntgenstrahlung*. Inauguraldissertation, Universität Rostock, December 2005.

[90] K. Scheiff. Heizen von Fe75Ni25-Nanopartikeln auf Wolframoberflächen. Bachelorarbeit, Heinrich-Heine-Universität Düsseldorf, Institut für Angewandte Physik, May 2017.

[91] H. Haberland, M. Karrais, M. Mall, and Y. Thurner. Thin films from energetic cluster impact: A feasibility study. *Journal of Vacuum Science & Technology A: Vacuum, Surfaces, and Films*, 10(5):3266, September 1992.

[92] B.M. Smirnov, I. Shyjumon, and R. Hippler. Flow of nanosize cluster-containing plasma in a magnetron discharge. *Physical Review E*, 75(6), June 2007.

[93] J. Kousal, O. Polonskyi, J. Blazek, O. Kylian, J. Pesicka, and H. Biederman. Velocity and charge of the nanoparticles produced by a gas aggregation cluster source. In *International Plasma Chemistry Society 20*, July 2011.

[94] J. Kousal, O. Polonskyi, O. Kylián, A. Choukourov, A. Artemenko, J. Pešička, D. Slavínská, and H. Biederman. Characterization of nanoparticle flow produced by gas aggregation source. *Vacuum*, 96:32–38, October 2013.

[95] M. Köhler. *Nanotechnologie – Eine Einführung in die Nanostrukturtechnik*. Wiley-VCH, 2001.

[96] H.E. Farnsworth, R.E. Schlier, T.H. George, and R.M. Burger. Ion bombardment-cleaning of germanium and titanium as determined by low-energy electron diffraction. *Journal of Applied Physics*, 26(2):252–253, February 1955.

[97] V.N. Popok, I. Barke, E.E.B. Campbell, and K.-H. Meiwes-Broer. Cluster–surface interaction: From soft landing to implantation. *Surface Science Reports*, 66(10):347–377, October 2011.

[98] M. Ganeva. *Formation of metal nano-size clusters with a DC magnetron-based gas aggregation source*. Inauguraldissertation, Ernst-Moritz-Arndt-Universität Greifswald, June 2013.

[99] M. Ganeva, T. Peter, S. Bornholdt, H. Kersten, T. Strunskus, V. Zaporojtchenko, F. Faupel, and R. Hippler. Mass Spectrometric Investigations of Nano-Size Cluster Ions Produced by High Pressure Magnetron Sputtering. *Contributions to Plasma Physics*, 52(10):881–889, November 2012.

[100] H. Hartmann, V. N. Popok, I. Barke, V. von Oeynhausen, and K.-H. Meiwes-Broer. Design and capabilities of an experimental setup based on magnetron sputtering for formation and deposition of size-selected metal clusters on ultra-clean surfaces. *Review of Scientific Instruments*, 83(7):073304, July 2012.

[101] C.G. Granqvist and R.A. Buhrman. Ultrafine metal particles. *Journal of Applied Physics*, 47(5):2200–2219, May 1976.

[102] L.B. Kiss, J. Söderlund, G.A. Niklasson, and C.G. Granqvist. New approach to the origin of lognormal size distributions of nanoparticles. *Nanotechnology*, 10(1):25–28, January 1999.

[103] P.H. Dawson, editor. *Quadrupole mass spectrometry and its applications*. Elsevier Scientific Publishing co., 1976.

[104] J.H. Gross. *Mass Spectroscopy - A textbook*. Springer-Verlag GmbH, 2nd edition, 2011.

[105] W. Paul. Electromagnetic traps for charged and neutral particles. In *Nobel Prize Lectures in Physics 1981–1990*, pages 601–622. World Scientific Publishing: Singapore, 1993.

[106] Oxford Applied Research. *Gas Condensation RF/DC Nanocluster Source NC200U*, 4.00 edition.

[107] Oxford Applied Research. *Quadrupole Mass Filter - QMF200*, 2.0 edition.

[108] VAT Vakuumventile. *UHV Gate Valve - 2D dimension drawing*, 206557 edition, June 1999. 10844-CE44.

[109] I.M. Goldby, B. von Issendorff, L. Kuipers, and R. E. Palmer. Gas condensation source for production and deposition of size-selected metal clusters. *Review of Scientific Instruments*, 68(9):3327–3334, September 1997.

[110] D. Nečas and P. Klapetek. Study of user influence in routine spm data processing. *Measurement Science and Technology*, 28(3):034014, January 2017.

[111] Omicron Vakuumphysik. *Micro SPM User's Guide*, 1.0 edition, June 1999.

[112] P. Klapetek, D. Nečas, and Ch. Anderson. Gwyddion user guide. `http://gwyddion.net/documentation/user-guide-en/index.html`.

[113] W. Demtröder. *Experimentalphysik 3 - Atome, Moleküle, Festkörper*. Springer, 3 edition, 2005.

[114] D. Meschede, editor. *Gerthsen Physik*. Springer, 23 edition, 2006.

[115] M. Puljiz, S. Wanjelik, and M. Getzlaff. Emissivity of polished tungsten surfaces as a function of temperature, detection angle and wavelength. In *DPG-Frühjahrstagung der Sektion Kondensierte Materie*, March 2015.

[116] J. Schubert. Deposition und temperaturabhängige Wechselwirkung von Co Nanopartikeln auf W(1 1 0). Bachelorarbeit, Heinrich-Heine-Universität Düsseldorf, Institut für Angewandte Physik, July 2017.

[117] Th. Michely and J. Krug. *Islands, mounds and atoms: patterns and processes in crystal growth far from equilibrium*. Springer series in surface sciences. Springer, 2004.

[118] National Institute of Standards and Technology; Physical Meas. Laboratory. Atomic weights and isotopic compositions. `http://physics.nist.gov/comp`.

[119] A. Kleibert, F. Bulut, W. Rosellen, K.-.H Meiwes-Broer, J. Bansmann, and M. Getzlaff. Supported and embedded Fe nanoparticles: Influence of the environment on shape and interface contributions to the magnetic anisotropy. *Journal of Physics: Conference Series*, 211:012017, February 2010.

[120] H. Bettermann and M. Getzlaff. Melting processes of 3d-metal nanoparticles on surfaces. In K. Wandelt, editor, *Encyclopedia of Interfacial Chemistry: Surface Science and Electrochemistry*. Elsevier Ltd, 1st edition, April 2018.

[121] A. Bettac, J. Bansmann, V. Senz, and K.-H. Meiwes-Broer. Structure and magnetism of hcp(0001) and fcc(001) thin cobalt films on a clean and carbon-reconstructed W(110) surface. *Surface Science*, 454–456(Supplement C):936–941, May 2000.

[122] T. Alonso-Lanza, Á. Mañanes, and A. Ayuela. Bonding of Cobalt Atoms, Dimers and Co_4 Clusters to Circumcoronene. *arXiv.org > Condensed Matter > Materials Science*, arXiv:1704.07718, April 2017.

[123] W. Rosellen. Messdaten Promotion, Fe_500V_Abdampfen, 03/04.02.2010.

[124] F. Bulut. Messdaten CD 1, sample, 19.12.2007.

[125] T. Irawan, D. Boecker, F. Ghaleh, C. Yin, B. von Issendorff, and H. Hövel. Metal clusters on rare gas layers – growth and spectroscopy. *Applied Physics A*, 82(1):81–86, January 2006.

Publications

T. Chirila, B. Schüler, H. Bettermann, M. Cerchez, and T. Heinzel. Collimation effects in electron transport through magnetic barriers in series. In preparation.

H. Bettermann and M. Getzlaff. Melting processes of 3d-metal nanoparticles on surfaces. In K. Wandelt, editor, *Encyclopedia of Interfacial Chemistry: Surface Science and Electrochemistry*. Elsevier Ltd, 1st edition, April 2018.

J. Bansmann, A. Kleibert, H. Bettermann, and M. Getzlaff. In-flight and postdeposition manipulation of mass-filtered nanoparticles under soft-landing conditions. In *Gas-Phase Synthesis of Nanoparticles*, pages 323–338. Wiley-VCH Verlag GmbH & Co. KGaA, March 2017.

H. Bettermann, M. Werner, and M. Getzlaff. Temperature-induced processes for size-selected metallic nanoparticles on surfaces. *Applied Surface Science*, 391:49–52, January 2017.

W. Rosellen, H. Bettermann, T. Veltum, and M. Getzlaff. Low energy impact of size selected FeCo nanoparticles with a W(110) surface. *Physica E*, 44(7-8):1683–1686, April 2012.

Conference contributions

•T.-F. Pabst, H. Bettermann, and M. Getzlaff. Thermally induced sharpening of tungsten STM-tips. Poster, *DPG-Frühjahrstagung*, Berlin, March 2018.

•M. Getzlaff and H. Bettermann. Melting processes of deposited 3d metal alloy nanoparticles. Talk, *Clustertreffen 2017*, Bacharach, September 2017.

•M. Getzlaff and H. Bettermann. Melting processes of 3d metal alloy nanoparticles deposited on surfaces. Talk, *33rd European Conference On Surface Science*, Szeged, August 2017.

•H. Bettermann, K. Scheiff, J. Schubert, and M. Getzlaff. 3d-metal nanoparticles on tungsten, tungsten-oxide and tungsten-carbide. Talk, *DPG-Frühjahrstagung*, Dresden, March 2017.

•J. Schubert, H. Bettermann, and M. Getzlaff. Deposition and temperature dependent surface interaction of Co nanoparticles on W(1 1 0). Poster, *DPG-Frühjahrstagung*, Dresden, March 2017.

T. Veltum, K. Elshimi, J. Andrews, H. Bettermann, and •M. Getzlaff. Size-selected cobalt nanoparticles deposited on the Cu(001)-C(2x2)N grid pattern. Poster, *18th International Symposium on Small Particles and Inorganic Clusters*, Jyväskylä, August 2016.

•H. Bettermann and M. Getzlaff. Deposition and surface interaction of 3d-metal nanoparticles on W(1 1 0). Poster, *DPG-Frühjahrstagung*, Regensburg, March 2016.

•K. Besocke, H. Bettermann, and M. Getzlaff. Characterization of a UHV evaporator for the coating of W-tips for room-temperature SP-STM. Poster, *DPG-Frühjahrstagung*, Regensburg, March 2016.

•K. Elshimi, J. Andrews, T. Veltum, H. Bettermann, and M. Getzlaff. Reconstructed Cu(100)-c(2x2)N surface for self-organized nanoparticle deposition. Poster, *DPG-Frühjahrstagung*, Regensburg, March 2016.

•T. Veltum, W. Gilbert, H. Bettermann, and M. Getzlaff. 3d metal nanoparticles deposited on graphene. Poster, *DPG-Frühjahrstagung*, Regensburg, March 2016.

•H. Bettermann, K. Elshimi, J. Andrews, H.N. Pham, T. Veltum, and M. Getzlaff. Surface interaction of deposited 3d metal nanoparticles on graphene and nanostructured Cu_xN. Poster, *Symposium on Size Selected Clusters*, Davos, February 2016.

•H. Bettermann, W. Gilbert, T. Veltum, and M. Getzlaff. Magnetic Nanoparticles from a Gas Aggregation Source. Talk, *Clustertreffen 2015*, Lindow, September 2015.

H. Bettermann, T. Veltum, M. Werner, W. Rosellen, and •M. Getzlaff. Temperature-induced processes for size-selected metallic nanoparticles on surfaces. Poster, *31st European Conference On Surface Science*, Barcelona, August 2014.

•H. Bettermann, M. Werner, and M. Getzlaff. FeNi nanoparticle preparation and deposition on W(110). Poster, *DPG-Frühjahrstagung*, Berlin, March 2015.

•W. Gilbert, T. Veltum, H. Bettermann, and M. Getzlaff. 3d metal nanoparticles deposited on graphene. Poster, *DPG-Frühjahrstagung*, Berlin, March 2015.

•M. Werner, H. Bettermann, and M. Getzlaff. Temperature dependent shape of deposited FeNi nanoparticles. Poster, *DPG-Frühjahrstagung*, Berlin, March 2015.

H. Bettermann, T. Veltum, W. Rosellen, and •M. Getzlaff. Energy dependent deposition and annealing of 3d nanoparticles on W(110) substrates. Poster, *Cluster Surface Interaction Workshop*, Varese, June 2014.

•H. Bettermann, M. Werner, and M. Getzlaff. 3d nanoparticle deposition on a W(110) surface. Talk, *DPG-Frühjahrstagung*, Dresden, March 2014.

•C. Häusler, H. Bettermann, and M. Getzlaff. Optical activity of chiral molecules and its analog on a macroscopic scale. Poster, *DPG-Frühjahrstagung*, Dresden, March 2014.

•M. Werner, H. Bettermann, and M. Getzlaff. FeNi nanoparticle deposition on a W(110) surface (poster). *DPG-Frühjahrstagung*, Dresden, March 2014.

•M. Wilhelm, H. Bettermann, and M. Getzlaff. Preparation of 3d nanoparticles by magnetron sputtering and deposition on a W(110) surface. Poster, *DPG-Frühjahrstagung*, Dresden, March 2014.

W. Rosellen, •H. Bettermann, and M. Getzlaff. Energy dependent nanoparticle deposition on a W(110) surface. Talk, *DPG-Frühjahrstagung*, Regensburg, March 2013.

•T. Veltum, H. Bettermann, and M. Getzlaff. Characterization of graphene on ferromagnetic materials. Poster, *DPG-Frühjahrstagung*, Regensburg, March 2013.

W. Rosellen, H. Bettermann, T. Veltum, A. Kleibert, and •M. Getzlaff. Nanoparticles on metal surfaces: low-energy impact. Talk, *29th European Conference On Surface Science*, Edinburgh, September 2012.

W. Rosellen, H. Bettermann, T. Veltum, and •M.Getzlaff. Low-energy nanoparticle impact. Talk, *International Conference on Nanoscience + Technology*, Paris, July 2012.

•H. Bettermann, W. Rosellen, and M. Getzlaff. Growth and characterisation of Fe thin films on MgO(100). Poster, *DPG-Frühjahrstagung*, Berlin, March 2012.

•W. Rosellen, H. Bettermann, and M. Getzlaff. Behavior of Co, Fe and FeCo alloy nanoparticles deposited on W(110). Talk, *DPG-Frühjahrstagung*, Berlin, March 2012.

•T. Veltum, H. Bettermann, and M. Getzlaff. Graphene as a supporting layer for nanoparticles. Poster, *DPG-Frühjahrstagung*, Berlin, March 2012.

•H. Bettermann, W. Rosellen, and M. Getzlaff. Characterisation of magnetic thin films on MgO(100). Poster, *DPG-Frühjahrstagung*, Dresden, March 2011.

•W. Rosellen, H. Bettermann, and M. Getzlaff. Nanoparticle impact on a W(110) surface. Talk, *DPG-Frühjahrstagung*, Dresden, March 2011.

Danksagung

Zuvorderst möchte ich mich bei meinem Betreuer Prof. Dr. Mathias Getzlaff bedanken, der mir die Möglichkeit zur Promotion in seiner Arbeitsgruppe gegeben hat und mich dabei fortlaufend unterstützt.

Weiterhin gilt mein Dank Prof. Dr. Klaus Schierbaum, dem Korreferenten dieser Arbeit, und mein Dank geht auch an meinem Promotionsmentor Prof. Dr. Dieter Schumacher.

Mein besonderer Dank gilt natürlich auch all denen, die mit Rat und Tat zum Gelingen dieser Promotion beigetragen haben:

Torsten Veltum hat diese Arbeit netterweise Korrektur gelesen und wir haben uns lange das Labor geteilt. Dies hat mir viel Arbeit erspart und ich hoffe ich habe ihn nicht zu oft mit neuen Vorschlägen für sein eigenes Labor genervt.

Maja Strugačevac sorgt seit jetzt fast zwei Jahre für eine superpositive Arbeitsatmosphäre und hat beim vielfachen Korrektur lesen viele Fehler beseitigt. Ich könnte mir keine liebere Büronachbarin wünschen.

Wolfgang Rosellen half als Betreuer während meiner Masterarbeit und während der Einarbeitung zu Beginn meiner Promotion.

Sara Wanjelik konnte mir, parallel zu ihrer eigenen Arbeit, im Labor helfen und konnte auch mit Tipps aushelfen. Ich habe mir gerne mit ihr ein Büro geteilt.

Stefan Manderla darf keinesfalls unerwähnt bleiben, denn er half immer aus, wenn ich ihn mit technischen Fragen zu den Turbopumpen gefunden haben und auch die Herstellung des Positionsspiegels für die Magnetronquelle war eine unbezahlbare Hilfe. Bei Fragen zu elektronischen Problemen hat mir Ulrich Rosowski weitergeholfen, als Beispiel sei hier die Plattenventilsteuerung erwähnt.

Viele Aufbauten wären ohne die Hilfe der Zentralwerkstatt der Physik nicht möglich gewesen. Mein Dank gilt dem Werkstattleiter Oliver Wyczisk und allen Mitarbeitern. Ohne die Zentralwerkstatt hätte es wahrscheinlich auch kein Vakuum gegeben!

Außerdem möchte ich mich bei unseren Bachelor- und Masterstudenten Kai Besocke, Kariman Elshimi, Wolfram Gilbert, Tobias Löffler, Timm Pabst, Hoai Nam Pham und Matthias Werner bedanken. Ihr habt das Institut zu dem gemacht, was es ist! Besonderen Dank verdient Benedikt Schlosza, der die Magnetronquelle umgebaut hat, während ich schon zusammengeschrieben habe, und der bei der Herstellung der Heizbox viel Geduld und Ausdauer bewiesen hat.

Diese Arbeit wurde (fast ausschließlich) mit freier Software erstellt. Vielen Dank an alle, die zur verwendeten Software beigetragen haben. Insbesondere natürlich an das pdfLaTeX- und XeLaTeX-Projekt und die Setzungsprogramme *TeXworks* und *TeXShop*. Die Auswertung und Präsentation der STM-Bilder wurde dank *Gwyddion* viel einfacher. Die 2D-Darstellungen wurden mit *LibreOffice*-Draw und die 3D-Darstellungen mit *OpenSCAD* erstellt.

Der Raspberry Pi im Labor hält mich seit mehr als ein Jahr über den Status „meines” Vakuums auf dem Laufenden. Unzählige wochenendliche Kontrollgänge konnten vermieden werden. Die Vielzahl der Projekte, auf die ich zurückgegriffen habe, würde jeden Rahmen sprengen und deshalb möchte ich mich hier (exemplarisch) beim *GPIO zero*-Projekt bedanken. Die Ansteuerung eines A / D-Wandlers mit nur zwei Zeilen Code hätte ich vorher nicht für möglich gehalten.

Eidesstattliche Versicherung

Ich versichere an Eides Statt, dass die Dissertation von mir selbstständig und ohne unzulässige fremde Hilfe unter Beachtung der „Grundsätze zur Sicherung guter wissenschaftlicher Praxis an der Heinrich-Heine-Universität Düsseldorf" erstellt worden ist.

Ferner erkläre ich, dass ich nicht anderweitig mit oder ohne Erfolg versucht habe, eine Dissertation einzureichen oder mich der Doktorprüfung zu unterziehen.

Düsseldorf, den 16. Januar 2018

Hendrik Bettermann